creative commons Attribution

Geopolimer-EPS kompozit szigetelő anyagok eredő hővezetési tényezőjének elméleti és kísérleti vizsgálata

MAGYAR Tamás ▪ Miskolci Egyetem, Nyersanyagelőkészítési és Környezeti Eljárástechnikai Intézet ▪ magyar.tamas@uni-miskolc.hu

FAITLI József ▪ Miskolci Egyetem, Nyersanyagelőkészítési és Környezeti Eljárástechnikai Intézet ▪ jozsef.faitli@uni-miskolc.hu

SZABÓ Roland ▪ Miskolci Egyetem, Nyersanyagelőkészítési és Környezeti Eljárástechnikai Intézet ▪ roland.szabo@uni-miskolc.hu

Érkezett: 2017. 08. 05. ▪ Received: 05. 08. 2017. ▪ https://doi.org/10.14382/epitoanyag-jsbcm.2017.13

Experimental- and theoretical investigation of the resultant thermal conductivity of geopolimer-EPS composite insulating materials

Today it is very important to minimize the use of energy, which is especially true for the thermal insulation of buildings. If heat-insulating materials for the construction industry can be produced from wastes or industrial byproducts (plastics, ashes), this innovative technology also contributes to the sustainability of modern living. Therefore, the main objective of the present paper is the theoretical and experimental investigation of the resultant thermal conductivity of lab scale and pilot scale geopolymer-polystyrene (EPS) composite insulating materials. The thermal conductivity measurements have been carried out by a new self-developed apparatus. The theories of the so-called serial and the parallel heat flow cases in two phase disperse systems are well known in the literature. The parallel and the serial heat flow models have been linked together in a theoretical universal equation. The dispersion constant (D) parameter has been introduced for the universal equation. The dispersion constant parameter is suitable for the characterization of the dispersion state of two phase disperse systems. Comparing the results of the experimental and theoretical resultant thermal conductivities it was concluded that the dispersion state of the measured geopolimer-EPS composite insulating materials is approximately 0.8. It was also observed that as the quantity of the ground fly ash increases the resultant thermal conductivity increases as well.

Keywords: geopolimer, EPS, thermal insulating material, thermal conductivity, serial and parallel heat flow model.

Kulcsszavak: geopolimer, EPS, hőszigetelő anyag, hővezetési tényező, soros és párhuzamos hővezetési modell.

MAGYAR Tamás

A Miskolci Egyetem Mikoviny Sámuel Földtudományi Doktori Iskolájában 2016. márciusában szerzett abszolutóriumot, jelenleg doktorjelölt. Környezetmérnöki MSc diplomáját 2011-ben szerezte a Miskolci Egyetemen. Fő kutatási témája: A települési szilárd hulladéklerakókban keletkező bomlási hő kinyerésének- és hasznosításának vizsgálata, illetve a diszperz anyagok hőtani paramétereinek vizsgálata.

FAITLI József

Okleveles bányagépészeti- és villamossági mérnök (1989), habilitált doktor, egyetemi docens, intézeti tanszékvezető a Miskolci Egyetem, Nyersanyagelőkészítési és Környezeti Eljárástechnikai Intézetének, Mechanikai Eljárástechnikai Intézeti Tanszékén. Fő kutatási témája a mechanikai eljárástechnika és a hulladékelőkészítés.

SZABÓ Roland

A Miskolci Egyetem Mikoviny Sámuel Földtudományi Doktori Iskolájának PhD hallgatója 2014. szeptemberétől. Előkészítéstechnikai mérnöki MSc diplomáját 2013-ban szerezte a Miskolci Egyetemen. 2013. júliusa és 2014. szeptembere között tanszéki mérnök a Miskolci Egyetem Nyersanyagelőkészítési és Környezeti Eljárástechnikai Intézetében. Jelenlegi kutatási témája a speciális tulajdonságú geopolimerek fejlesztése, különös tekintettel a habszerkezetű geopolimer termékre.

1. Bevezetés

Az épületek gazdaságos üzemeltetésének egyik általánosan alkalmazott módszere a külső falazatokra felvitt hőszigetelő anyagok alkalmazása. Ennek ellenére az épületek fűtésére és hűtésére felhasznált energia igen jelentős, ezért a hőszigetelés megfelelő kialakítása, illetve működtetése jelentős energiamegtakarítást eredményezhet. Az USA Energiaügyi Minisztériumának jelentése [1] szerint a fűtési-, illetve hűtési költségek a teljes épület energetikai költségeit tekintve 50-70%-ot is jelenthetnek egy átlagos otthon esetében. Az említett arány magasabb is lehet kedvezőtlen éghajlati viszonyok mellett, illetve alacsonyabb energiahatékonysággal rendelkező épületeknél. Az épületek megfelelően megválasztott, illetve kivitelezett hőszigetelése nagymértékben hozzájárul az energiahatékonyság növeléséhez, amely a költségeket is jelentősen csökkentheti. A fűtésre és hűtésre felhasznált energia mennyisége attól függ, hogy az épület mennyire „jól" hőszigetelt. A hőszigetelést tekintve megkülönböztethetünk külső, illetve belső hőszigeteléseket. A külső hőszigetelés mellett a belső hőszigetelés is jelentős hatással van az energiafogyasztásra, különösen a több hőmérsékleti zónával rendelkező épületek esetében, melynek tipikus példái a többemeletes lakótömbök (panelépületek) [2]. Az épületek esetében alkalmazott hőszigetelő anyagok egyik legfontosabb műszaki paramétere a hővezetési tényező (jele: λ, mértékegysége: W/mK), amely értéke minél kisebb, annál jobban ellenáll az anyag, a két ellentétes oldalán kialakuló hőmérsékletkülönbség következtében létrejövő és rajta áthaladó hőárammal szemben, tehát annál jobb hőszigetelő anyagról beszélhetünk.

Másrészt, a modern életvitel jelentős környezetterheléssel jár, ezért a magas életszínvonal fenntarthatósága érdekében alapvető cél, hogy a hulladékká vált anyagokat vagy melléktermékeket vissza tudjuk forgatni a gazdaságba (EU körkörös gazdaság elve). Igen nagy tömegben keletkeznek salak és pernye anyagok a szén és lignittüzelésű erőművekben, amely anyagok már deponált mennyisége is jelentős. Világméretű probléma a hulladékká váló műanyagok óriási mennyisége is, amelynek egy kis szelete a polisztirol. Amennyiben pernye és polisztirol melléktermék és hulladék anyagokból jó minőségű épületi szigetelő anyagokat tudnánk gyártani, az mind az energiahatékonyság, mind a körkörös gazdaság szempontjából előnyös lenne.

2. Hővezetés többfázisú diszperz rendszerekben

A többfázisú diszperz rendszerekben a hő vezetésének jelensége igen összetett folyamat. A termodinamika alapjait figyelembe véve egy adott rendszer (anyaghalmaz) belső energiájának a megváltozása a következő négy típusú energiacsere következményeként jöhet létre:

- hőátadás, amelyet a hőmérséklet és az entrópia;
- mechanikai energia, vagy más néven a térfogatváltozási munka, amelyet a nyomás és a térfogat;
- kémiai energia, amelyet a vegyérték és a reakcióba lépő anyagok moláris mennyisége; illetve,
- a felületi energia, amelyet a felületi feszültség és a fázisok közötti felület jellemeznek.

Egyensúlyi állapotban a különféle energiatípusokat jellemző paraméter párok egyike alapvetően meghatározza az egyensúlyi állapotot. Roth szerint [3], létezik egy olyan termodinamikai potenciál, amelynek a jellemzői a rendszer méretével egyenesen arányosak, illetve amelynek szélső értéke (minimuma) van egyensúlyi állapotban. Egy többfázisú diszperz rendszer eredő hővezetési tényezőjének vizsgálata során az uralkodó energiacsere típusokat kell figyelembe venni. Egy folytonos egyfázisú anyag belső energiája megfelel az anyag mikroszkopikus építő elemeinek molekuláris szintű kinetikus energiáinak összegével. A magasabb hőmérséklettel rendelkező atomok, molekulák nagyobb kinetikus energiával rendelkeznek – tehát gyorsabban és nagyobb amplitúdóval rezegnek –, amelyet a szomszédos molekulák felé képesek átadni. Gyakorlatilag ez az a mechanizmus, amelynek segítségével terjed a hő az anyagban a magasabb hőmérsékletű részek felől az alacsonyabb hőmérsékletű részek felé. Többfázisú rendszer esetén a hőterjedés a fázishatárokon lévő molekulák között hasonlóan – oszcilláló energiacsere segítségével – megy végbe, mint az előzőleg említett esetben. A különböző anyagok hőtani viselkedése nagyban függ a fázisváltástól, azaz a halmazállapot megváltozásától. Az eredő hőtani paraméterek a diszperz anyagban lejátszódó mikro folyamatokat – így a fázisváltást, a rejtett hőt a gőz fázisban és az érzékelhető hőt a folyadék fázisban – is magukban foglalják.

A kapcsolódó szakirodalmat áttekintve megállapítható, hogy Maxwell [4] volt az első, aki nagyon kis koncentrációban jelen lévő monodiszperz szemcséket tartalmazó kétfázisú keverékek eredő hővezetési tényezőjét vizsgálta. A vizsgálatai során feltételezte, hogy a szemcsék között nincs érintkezés, így azok között nem jönnek létre hőhidak. Később Rayleigh [5], illetve Zehner és Schundler [6] fejlesztették tovább a Maxwell [4] által megalkotott modellt. Zehner és Schundler [6] az egyszerűsített modell alapján feltételezte, hogy a diszperz rész azonos méretű gömb alakú szemcsékből áll. Az említett modellek alapján a kétfázisú durva diszperz rendszer eredő hővezetési tényezője a koncentráció függvényében az *1. ábrán* látható, amikor is a szilárd diszperz rész hővezetési tényezője százszorosa (λ_2/λ_1=100) a diszperziós közeg hővezetési tényezőjének.

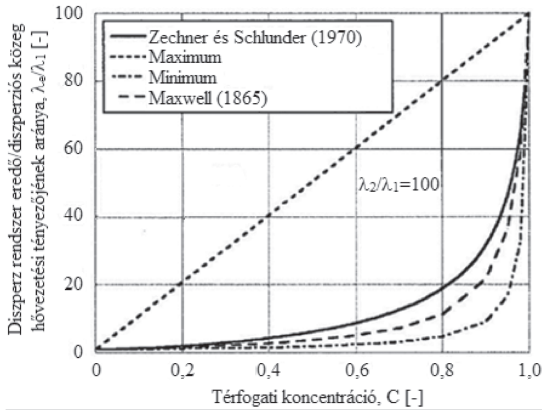

1. ábra Monodiszperz gömb alakú szemcséket tartalmazó durva diszperz rendszerek eredő hővezetési tényezője a koncentráció függvényében [7]
Fig. 1. The resultant thermal conductivities of two-phase disperse systems containing only spherical monodisperse particles as funtion of the concentration [7]

A soros és párhuzamos hővezetési modellek ismertetéséhez vizsgáljunk meg egy kétfázisú szilárd-gáz diszperz rendszert. A szilárd fázis legyen a diszpergált fázis, a gáz fázis pedig a diszperziós közeg. A térfogathányadok (koncentrációk) összege legyen egységnyi (1), azaz:

$$\varepsilon_s + \varepsilon_g = 1 \tag{1}$$

A bemutatott rendszer leegyszerűsítve modellezhető olyan módon, hogy az összes szemcsét egy összefüggő szilárd testnek képzeljük el, amely mellett a gáz fázis összefüggően kitölti a fennmaradó térrészt. A valódi diszperz rendszerhez képest ez a modell nagymértékű egyszerűsítést jelent, azonban a gyakorlatban találkozhatunk ilyen, nem diszperz anyagokkal. Amennyiben a valós diszperz állapotot ilyen módon leegyszerűsítettük, illetve modelleztük, a hőáramlás irányát és a fázisok elhelyezkedését tekintve kétféle szélsőséges elrendezésről (állapotról) beszélhetünk. Amennyiben a hő áramlása sorosan megy végbe a diszperz rendszert alkotó fázisokon keresztül (*2. ábra*), abban az esetben az eredő hővezetés értéke alacsony lesz, ugyanis a gáz fázis hővezetési tényezője nagyságrendekkel alacsonyabb – ez jelenti tehát az alsó korlátot (*1. ábra*) –, mint a szilárd fázis esetében.

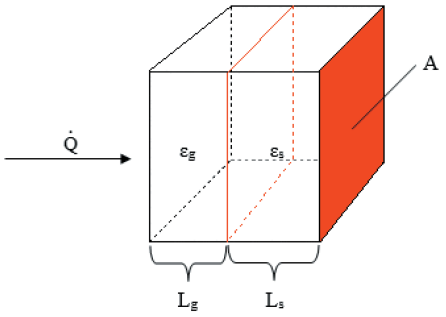

2. ábra Soros hővezetési modell kétfázisú diszperz rendszerekre (elméleti minimum)
Fig. 2. Serial heat flow model for two-phase disperse systems (theoretical minimum)

Az egységnyi felületen áthaladó hőáram kétfázisú soros elrendezés esetén a (2) képlettel számítható:

$$\dot{Q} = \frac{1}{\frac{L_s}{\lambda_s} + \frac{L_g}{\lambda_g}} \cdot A \cdot \Delta T \tag{2}$$

A soros elrendezéshez tartozó eredő hővezetési tényezőt a (3) képlet segítségével kaphatjuk meg:

$$\lambda = \frac{\lambda_s \cdot \lambda_g}{\varepsilon_s \cdot \lambda_g + \varepsilon_g \cdot \lambda_s} \quad (3)$$

Az egységnyi felületen áthaladó hőáram kétfázisú párhuzamos elrendezés esetén (*3. ábra)* megegyezik a két párhuzamosan elhelyezkedő fázison áthaladó rész hőáramok összegével (4), amely gyakorlatilag az elméleti maximum értéket jelenti (*1. ábra*).

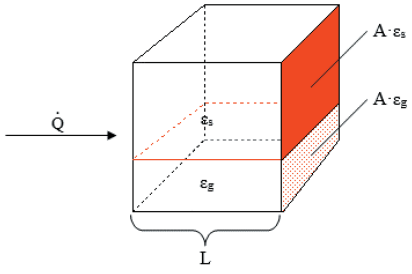

3. ábra Párhuzamos hővezetési modell kétfázisú diszperz rendszerekre (elméleti maximum)
Fig. 3. Parallel heat flow model for two-phase disperse systems (theoretical maximum)

$$\dot{Q} = \dot{Q}_s + \dot{Q}_g = \frac{\lambda_s}{L} \cdot A \cdot \varepsilon_s \cdot \Delta T + \frac{\lambda_g}{L} \cdot A \cdot \varepsilon_g \cdot \Delta T \quad (4)$$

A hőáramlás irányát tekintve az alkotó fázisok párhuzamos elrendezése esetében az eredő hővezetési tényező az (5) egyenlet segítségével adható meg:

$$\lambda = \lambda_s \cdot \varepsilon_s + \lambda_g \cdot \varepsilon_g \quad (5)$$

Egy valós kétfázisú (szilárd-gáz) diszperz rendszerben az eredő hővezetési tényező az alsó (soros hővezetési modell) és felső (párhuzamos hővezetési modell) korlát közé kell, hogy essen, amelyre számos paraméter hatással van. Ezek a paraméterek főként a szemcseméret-, a szemcsealak-, és a szemcsesűrűség-eloszlás, illetve alapvetően a koncentráció.

3. Anyagok és módszerek

A hőtani vizsgálataink középpontjában olyan pernye alapú geopolimer kompozit anyagok állnak, amelyek különböző térfogatszázalékban tartalmaznak hozzáadott expandált polisztirolt. Az egyébként is jó hőszigetelő képességgel rendelkező geopolimerek hővezetési tényezője, illetve testsűrűsége jelentősen csökkenthető expandált polisztirol gyöngyök (EPS) hozzáadásával. A másodnyersanyagokból létrehozott kompozit anyag alkalmas lehet az építőipari szigetelő anyagok jövőbeni kiváltására. Alkalmazásának másik fontos előnye, hogy a deponálandó hulladék mennyisége is csökken.

3.1. Felhasznált anyagok

3.1.1. Geopolimer

A geopolimerek amorf alumino-szilikátok, melyek lúgos közegben (KOH, NaOH) szilícium-dioxid és alumino-szilikát-oxidok között lejátszódó reakció során állíthatók elő szobahőmérsékleten vagy magasabb hőmérsékleten (30-100 °C) egyaránt. Ez a reakció egy amorf félig-kristályos háromdimenziós polimer struktúrát eredményez, mely Si-O-Al kötésekből áll [8, 9]. Minden olyan elsődleges vagy másodlagos nyersanyag alkalmas geopolimer gyártására, amely reaktív szilícium-dioxid és alumínium-oxid fázisokat tartalmaz, mint például a természetes kőzetek vagy ipari melléktermékek (pl. erőműi pernye, salak és vörösiszap) [8, 9, 10, 11]. A geopolimerek jó fizikai-kémiai és mechanikai tulajdonságokkal rendelkeznek, többek között alacsony sűrűség, mikro- vagy nanoporozitás, csekély zsugorodás, magas szilárdság, hőstabilitás, nagy felületi keménység, tűz- és kémiai ellenállóság jellemzi azokat [12, 13, 14]. A geopolimer szilárdsága a pernye őrlésével szabályozható [15, 16].

3.1.2. Expandált polisztirol (EPS)

Az expandált polisztirolhab (EPS) alapanyaga hőre lágyuló polimerizált sztirol, ami habosító anyagot és égéskésleltető adalékot tartalmaz. A túlnyomórészt levegőből álló anyag kiváló hőszigetelő képességgel rendelkezik, jól alakítható, egészségre, illetve környezetre nem veszélyes. Az expandált polisztirolhab legfontosabb jellemzője az igen alacsony hővezetési tényező, amely a zárt cellákban nyugvó levegőnek köszönhető [17]. Kiváló hőszigetelő képessége mellett, alkalmazásának széleskörű elterjedésében fontos szerep jutott az igen kis testsűrűségnek (30 kg/m³), valamint annak, hogy jelenleg az egyik legolcsóbb homlokzati hőszigetelő anyag [18].

3.2. Geopolimer-EPS kompozit próbatestek gyártása

A próbatestek gyártása, illetve vizsgálata laboratóriumi- és félüzemi (I. és II. széria) méretben történt. A laboratóriumi szériás minták előállítása során őrölt deponált tiszaújvárosi pernyét használtunk, mint geopolimer szilárd fázis, amelyhez NaOH és nátrium-szilikát lúgos aktiválószert kevertünk 45 m/m% arányban egy függőleges habarcskeverőben. Ezután a geopolimer pasztához adagoltuk az előaprított polisztirol szemcséket (0,5-10 mm), amely keveréket a homogenizálást követően 400×400 mm-es alapterületű sablonokba öntöttük, majd vibrációsan tömörítettük. Az elkészített próbatestek magassága változó volt, amelyeket a hővezetési tényező mérése során figyelembe vettünk.

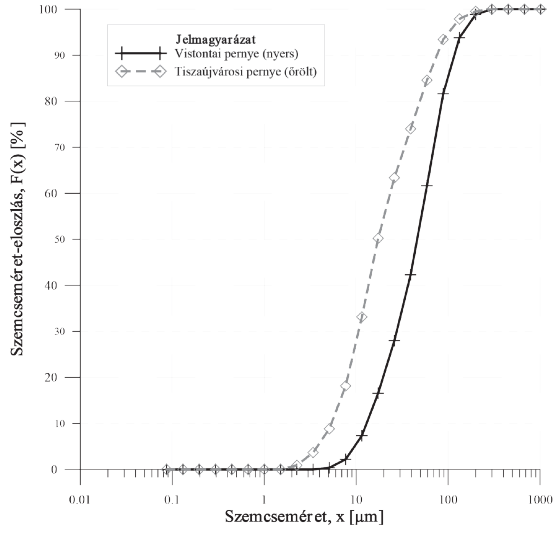

4. ábra A próbatestek elkészítésénél alkalmazott tiszaújvárosi (őrölt) és a visontai (nyers) pernye szemcseméret-eloszlása
Fig. 4. Particle size distributions of the applied fly ashes from Tiszaújváros (ground) and Visonta (raw)

A félüzemi mérések két szériája ehhez képest annyival tért el, hogy a geopolimer komponens pernye összetételét a kötésidő szabályozása érdekében megváltoztattuk: az I. szériában 90 m/m% nyers visontai pernye és 10 m/m% őrölt tiszaújvárosi pernye, a II. szériában pedig 80 m/m% nyers visontai pernye és 20 m/m% őrölt tiszaújvárosi pernye volt az összetétel. A próbetestek előállításához alkalmazott pernyék szemcseméret-eloszlásait a *4. ábra*, a nevezetes szemcseméreteket, illetve a fajlagos felület nagyságát a *1. táblázat* szemlélteti.

Pernye megnevezése	x_{10} (μm)	x_{50} (μm)	x_{80} (μm)	Fajlagos felület (cm^2/cm^3)
Visontai pernye (nyers)	13,2	46,7	85,4	2018,0
Tiszaújvárosi pernye (őrölt)	5,5	17,3	49,4	4977,4

1. táblázat A próbatestek elkészítésénél alkalmazott tiszaújvárosi (őrölt)- és a visontai (nyers) pernye nevezetes szemcseméretei, illetve a fajlagos felület nagysága
Table 1. The characteristic particle sizes and the specific surface areas of the applied fly ashes from Tiszaújváros (ground) and Visonta (raw)

További eltérés a laboratóriumi kísérletekhez képest, hogy a félüzemi szériák esetében a 10 V/V% geopolimer-tartalmú mintáknál a pernyéhez 47 m/m%-ban adagoltuk az aktiváló oldatot, annak érdekében, hogy a polisztirolt egyenletesebben vonja be a geopolimer paszta. A többi esetben 45 m/m%-ban tartalmazott lúgos aktiválószert a geopolimer paszta. A félüzemi kísérletek során a keverést egy 150 l térfogatú kényszerkeverővel valósítottuk meg, a sablonok mérete pedig 500×1000×100 mm, illetve 100×500×200 mm volt, amelyekből a hővezetési tényező meghatározásához, a mérőberendezésbe illeszkedő 400×400 mm-es alapterületű mintákat vágtunk ki. Az elkészült próbatestek (*5. ábra*) összetevőinek arányait a *2. táblázat*ban adjuk meg.

5. ábra Az elkészült geopolimer-EPS kompozit próbatest [18]
Fig. 5. A geopolimer-EPS composite specimen

Összetevők, [V/V %]	Próbatestek típusa												
	Laboratóriumi					Félüzemi (I. széria)				Félüzemi (II. széria)			
EPS	100	98	97	90	60	100	98	97	60	100	98	97	60
Geopolimer	0	2	3	10	40	0	2	3	40	0	2	3	40

2. táblázat Az elkészült geopolimer-EPS kompozit próbatestek összetételi arányai
Table 2. Composition ratios of the geopolimer-EPS specimens

3.3. A diszperz anyagok hőtani tulajdonságainak mérésére kifejlesztett berendezés és a kiértékelési módszer

A berendezés megtervezésekor elsősorban a hővezetési tényező mérése volt a cél, a többi paraméter mérése párhuzamosan, vagy kiegészítő méréssel valósítható meg. A hővezetési tényező mérésére alapvetően három különféle alapelv szerint van lehetőség. Az első a tökéletest megközelítő teljes hőszigetelés, amikor hőszigetelés útján tudjuk a hőárammérő szenzoron keresztül haladó hőfluxust behatárolni, úgy hogy a hőáram fluxus vektorok egymással párhuzamosak, a szenzorra pedig merőlegesek legyenek. A második alapelv szerint az oldalirányú hőveszteséget kell pótolni egy szabályozott segéd fűtőrendszer által. A harmadik módszer szerint olyan geometriájú mérőberendezést kell építeni, amiben a teljes hőáramnak csak egy belső, jól meghatározott keresztmetszetét mérjük. A belső mért keresztmetszet lényegesen kisebb, mint a teljes keresztmetszet, így a mért keresztmetszetben a hőáram vonalak párhuzamosak, az oldalirányú veszteségek pedig nem befolyásolják a mérést. A Miskolci Egyetem, Nyersanyagelőkészítési és Környezeti Eljárástechnikai Intézetében megépített mérőberendezés a harmadik elven alapul, az így kialakított konstrukció pedig alkalmas építőipari hőszigetelő anyagok hőtani jellemzőinek, illetve a többfázisú diszperz rendszerek eredő hőtani paramétereinek a mérésére is.

A kifejlesztett berendezés két fontos része a fűtéssel ellátott fedél és az alsó nyitott doboz (*6. ábra*), amelyeket vörösrézből alakítottunk ki, a jobb hővezetés biztosítása érdekében. A fedélbe khantál ellenálláshuzalból és kerámia szigetelőgyűrűkből kialakított fűtőegység került beépítésre. A beépített fűtőszálak egyenletesen lefedik a fedél teljes 400×400 mm-es felületét, a berendezéssel vizsgálható minta maximális magassága 60 mm.

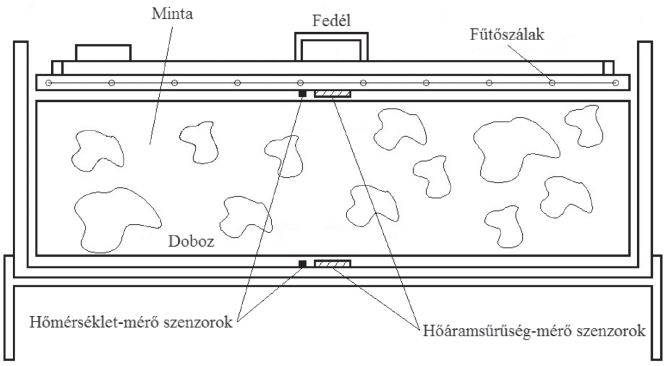

6. ábra A diszperz anyagok hőtani tulajdonságainak mérésére kifejlesztett berendezés sematikus rajza
Fig. 6. Schematic of the developed thermal properties measuring device for disperse systems

A fűtőszálak elektromos táplálását nem közvetlenül a 230 V effektív feszültségű hálózatból, hanem 0...80 V közötti változtatható feszültségű laboratóriumi tápegységből nyerjük, így a berendezés rugalmasan igazítható az eltérő tulajdonságú vizsgálati anyagokhoz. Mivel a fűtőszálak árama és feszültsége a stabil táp következtében állandó, így a fűtőteljesítmény (P) is közel állandónak tekinthető egy-egy mérés során. A hőáram mérésére 2 db AHLBORN FQA018C, 100×100 mm felületű, 2 mm vastag hőárammérő lap került alkalmazásra. A hőárammérő

lap nagyszámú sorba kapcsolt hőelemet tartalmaz, a kimenő mV nagyságrendű feszültség jel közvetlenül a felületegységen áthaladó hőmennyiséggel arányos. A hőárammérő lapok gyárilag kalibráltak (9,4 W/m² / 1 mV). Egy hőárammérő lap a fedél közepére ($Q_{felső}$) és egy másik lap a doboz aljának a közepére ($Q_{alsó}$) került beépítésre. A hőmérséklet mérésére 2 db National Semiconductor gyártmányú LM35CN típusú integrált hőmérsékletérzékelő került beépítésre a fedélbe ($T_{felső}$) és a doboz aljába ($T_{alsó}$), közvetlenül a hőárammérő lapok mellé. Az 5-30 V táp tartományban működőképes TO92 (plastic) tokozású szenzor 10 mV/°C kimenő jelet ad 0,1 ohm kimenő impedancia mellett (I_{ki} < 1 mA), ezért a kapcsolódó jelvezeték ellenállása nem befolyásolja a mérést. A szenzor -55 °C és +150 °C tartomány átfogására alkalmas. Kimenete lineáris, a mérési hiba kisebb, mint 0,5 °C.

Mivel a megépített berendezés egy teljesen új konstrukció, ezért kiértékelési módszert is kellett hozzá fejleszteni. A kísérleti berendezéssel 2015 januárjában – többek közt – elvégeztünk egy kalibrációs mérést a tiszta EPS-re vonatkozóan (*7. ábra*). A vizsgált EPS lemez hővezetési tényezője 0,039 W/mK, amely a gyártó által biztosított érték. Méréseink alapján ez az érték 0,036 W/mK-re adódott, amely kevesebb, mint 8 %-os eltérést jelent a gyári értékhez viszonyítva.

Egy mérés jellemzően három napig tartott, mivel a hőtani paraméterek meghatározásához közel egyensúlyi állapot elérése szükséges. A tanulmányban elvégzett mérések laboratóriumi körülmények között történtek, éppen ezért a külső, környezeti hőmérséklet közel állandónak tekinthető. Természetesen a berendezés környezeti hőmérséklete is rögzítésre került. A berendezéssel a szabadban is lehet méréseket végezni, amikor néhány nap alatt kvázi stacionér állapot alakul ki, azaz a paraméterek követik a napi hőingadozást. A *7. ábrán* láthatóak a mért hőmérsékletek és hőáramsűrűségek az idő függvényében. A fedélben lévő hőáramsűrűség mérő szenzor mért eredményei pozitív előjellel rendelkeznek, amelyet úgy kell értelmezni, hogy a hő a fűtés hatására a berendezésben lévő minta felé áramlik. A mérő berendezés alsó, doboz részében található hőáramsűrűség mérő szenzor mért értékei negatív előjelűek, amely azt jelenti, hogy a hő a mintából a berendezés alján keresztül a környezet felé távozik. Az alkalmazott hőáramsűrűség mérő szenzorok számos – sorba kapcsolt – hőelemből állnak, amelyek kimenő feszültségének a polaritása jelzi a hőáramlás irányát. A fedélben lévő hőáramsűrűség mérő szenzor által mért értékek csak a fűtő rendszer bekapcsolása után kezdtek el növekedni. Amint a hő a fedélben lévő hőáramsűrűség mérő szenzoron keresztül megérkezik a mérő berendezés aljában lévő hőáramsűrűség mérő szenzorhoz, a mért alsó hőáramsűrűség értékek elkezdenek csökkenni. Ahogyan már korábban említettük a teljes egyensúlyi állapot elérése nem történt meg, de egy kvázi egyensúlyi állapotban a hőáramsűrűségek (Q) és a hőmérséklet-különbség (ΔT) – amikor a bemenő- és a kimenő hőáramsűrűség megegyezik a 100×100 mm-es felületen mért virtuális „csatornán" keresztül – meghatározható (*7. ábra*). A hő által megtett út (L) ismert, mivel az a hőáramsűrűség mérő szenzorok közötti mért távolság, amely gyakorlatilag megegyezik a próbatest

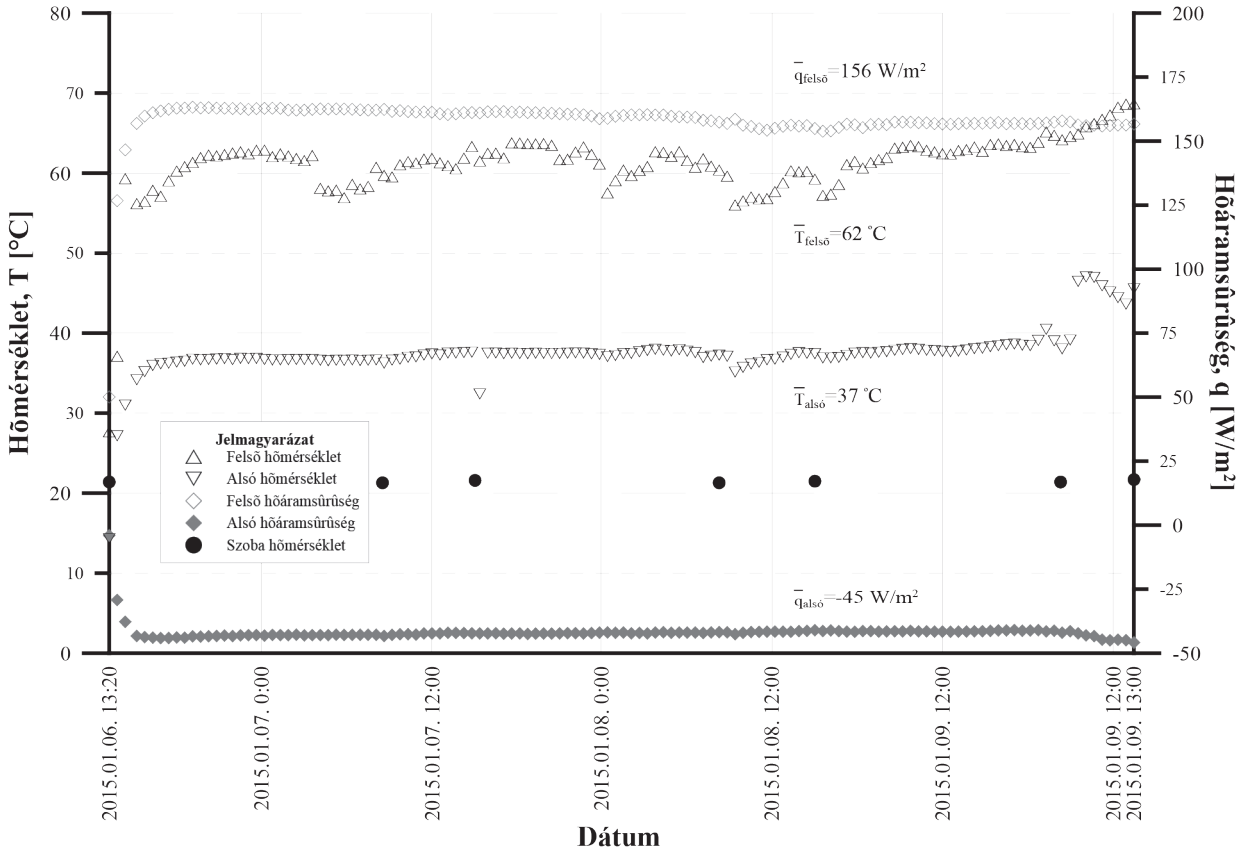

7. ábra A tiszta EPS-re vonatkozó kalibrációs mérés eredménye
Fig. 7. Results of the calibration measurement with pure EPS

magasságával. A fent leírtak alapján a hővezetési tényező a (6) egyenlet segítségével a mért adatokból egyszerűen számítható:

$$\lambda = \frac{Q \cdot L}{\Delta T} \qquad (6)$$

A fűtés bekapcsolása után a fedélben elhelyezett hőmérő szenzor mért értékei is emelkedni kezdenek. 40 V-os konstans tápfeszültség esetében a felső hőmérő szenzor által mért értékek a 40-50 °C-os mérési tartományban álltak be, míg 60 V-os tápfeszültségnél ugyanez a tartomány már 70-80 °C közé esett. A kísérleti berendezés alsó részében elhelyezett hőmérő szenzor mért értékei természetesen alacsonyabbak, mint a felső szenzor által mért értékek, amelynek oka, hogy a berendezés 100 mm-es lábakon áll, tehát az alja vissza tud hűlni a környezethez relatíve közeli hőmérsékleti értékre. A fedélben lévő hőmérő szenzor által mért értékekre illesztett görbének a meredeksége a felfűtési szakaszra vonatkozóan ($\Delta T/\Delta t$) arányos a mért minta fajhőjével. A kifejlesztett kísérleti berendezés nem alkalmazható közvetlenül a fajlagos hőkapacitás (C_m) mérésére, mert a betáplált hőnek csak egy része áramlik a mintába és melegíti fel azt, a hő többi része gyakorlatilag magát a berendezést, illetve a környezetet fűti. A mérések alapján azonban meghatározható volt, hogy a rendszerbe betáplált hőnek csak a kb. 1/3,75-öd része fordítódik a betöltött minta felmelegítésére, amely érték a berendezésre jellemző együttható (I). A berendezésre vonatkozó együttható-, a minta tömegének (m_m)-, illetve halmazsűrűségének (ρ_B) ismeretében a fajhő és a hődiffuzivitás (κ) a következőképpen írható fel (7):

$$C_m = \frac{P \cdot I}{m_m \cdot \frac{\Delta T}{\Delta t}} \quad \text{és} \quad \kappa = \frac{\lambda}{\rho_B \cdot C_m} \qquad (7)$$

4. Eredmények

4.1. A hővezetés univerzális egyenlete kátfázisú diszperz rendszerekre

A korábbiakban beláttuk, hogy a diszperz állapotú anyagokban vezetéssel megvalósuló eredő hőátadás, röviden a hővezetés, azért nagyon bonyolult jelenség mert ez számtalan belső hővezetési és a diszperz rész és diszpergáló közeg közötti határfelületeken hőátadási részjelenségekre bontható. Valódi diszperz anyagokban a szemcsék, cseppek és buborékok száma igen nagy, a jellemzőik pedig igen változatosak lehetnek, ezért nem az volt a célunk, hogy a komponensek fizikai jellemzői alapján adjunk becslést az eredő hővezetésre. Ezzel szemben egy konkrét mérhető anyag, azaz adott eredő diszpergáltsági állapotban szeretnénk az állapotot egy mérőszámmal jellemezni és az eredő hővezetési tényezőt méréssel és számítással meghatározni. A *3. táblázat*ban összefoglaltuk azt a gondolatmenetet, amellyel a kétfázisú esetre vonatkozó univerzális eredő hővezetési tényező egyenletet (8) vezettünk le.

A 2. fejezetben már összefoglaltuk – példaként szilárd–gáz diszperz rendszerre – a kétfázisú hővezetés lehetséges két szélső esetét, a soros- és párhuzamos elrendezésű hővezetési eseteket. A levezetés érdekében jelöljük K-val a két fázis hővezetési tényező értékeinek a hányadosát. A cél az, hogy a soros- és párhuzamos hővezetési egyenleteket egy olyan kombinált egyenletbe foglaljuk össze, amely tartalmazza, az un. D-diszperzitásállandót és D=1 esetén a soros, míg D=0 esetén a párhuzamos egyenletre egyszerűsödik vissza. Ennek érdekében mindkét esetre λ/λ_s un. célfüggvény határozható meg, amely segítségével a (8) egyenlet felírható.

Kétfázisú rendszer (szilárd-gáz) eredő hővezetési tényezője soros elrendezés esetén	Kétfázisú rendszer (szilárd-gáz) eredő hővezetési tényezője párhuzamos elrendezés esetén
$\frac{1}{\lambda} = \frac{\varepsilon_s}{\lambda_s} + \frac{\varepsilon_g}{\lambda_g}$	$\lambda = \lambda_s \cdot \varepsilon_s + \lambda_g \cdot \varepsilon_g$
$\varepsilon_g = 1 - \varepsilon_s$ és $\lambda_g = K \cdot \lambda_s$ (ahol K az arányossági tényező, amely megmutatja, hogy λ_s értéke hány szorosa, illetve hányad része λ_g értékének)	
$\frac{1}{\lambda} = \frac{\varepsilon_s}{\lambda_s} + \frac{1-\varepsilon_s}{K \cdot \lambda_s}$	$\lambda = \lambda_s \cdot \varepsilon_s + (1-\varepsilon_s) \cdot K \cdot \lambda_s$
$\frac{1}{\lambda} = \frac{1}{\lambda_s} \cdot \left(\varepsilon_s + \frac{1-\varepsilon_s}{K} \right)$	$\lambda = \lambda_s \cdot [\varepsilon_s + (1-\varepsilon_s) \cdot K]$
$\frac{1}{\lambda} = \frac{1}{\lambda_s} \cdot \frac{K \cdot \varepsilon_s + (1-\varepsilon_s)}{K}$	
$\lambda = \lambda_s \cdot \frac{K}{K \cdot \varepsilon_s + (1-\varepsilon_s)}$	
Célfüggvény: $\frac{K}{K \cdot \varepsilon_s + (1-\varepsilon_s)}$	Célfüggvény: $\varepsilon_s + (1-\varepsilon_s) \cdot K$

Kétfázisú rendszer (szilárd-gáz) eredő hővezetési tényezőjének univerzális egyenlete (soros- és párhuzamos hővezetési modell összekapcsolása):

$$\lambda = \lambda_s \cdot \left\{ \frac{K}{[K \cdot \varepsilon_s + (1-\varepsilon_s)] \cdot [\varepsilon_s + (1-\varepsilon_s) \cdot K]} \right\}^D \cdot [\varepsilon_s + (1-\varepsilon_s) \cdot K] \qquad (8)$$

ahol D a diszperzitás állapot, D=1 esetén a soros-, D=0 esetén a párhuzamos elrendezéshez tartozó eredő hővezetési tényező képletét kapjuk vissza.

3. táblázat A hővezetés univerzális egyenlete kétfázisú diszperz rendszerekre
Table 3. Theoretical universal equation of heat flow in two-phase disperse systems

4.2. A mérési eredmények és az új modell összevetése

A hővezetési tényező méréseket kéfázisú geopolimer-EPS rendszerekben végeztük el, ami szilárd-szilárd durva diszperz rendszer. A geopolimer a diszperziós közeg, amiben az EPS szemcsék diszpergálva vannak. Annak ellenére, hogy a geopolimer komponenst többféle pernye is alkotja, a geopolimer komponenst tekintsük az egyik folytonos és homogén szilárd fázisnak. A másik szilárd komponens ebben az esetben az EPS. A laboratóriumi-, illetve a félüzemi I. és II. szériás mintákon elvégzett hővezetési tényező meghatározásának mérési eredményeit a *4. táblázat*ban foglaltuk össze.

A *8. ábra* szemlélteti a kifejlesztett mérőberendezéssel meghatározott hővezetési tényező értékeit (fekete háromszög) a geoplimer- és az EPS komponens térfogatarányainak függvényében a laboratóriumi szériás minták esetében. A mért hővezetés tényezők mellett feltüntettük az egyes diszperzitás

Összetevők, [V/V %]	Próbatestek típusa												
	Laboratóriumi					Félüzemi (I. széria)				Félüzemi (II. széria)			
EPS	100	98	97	90	60	100	98	97	60	100	98	97	60
Geopolimer	0	2	3	10	40	0	2	3	40	0	2	3	40
Mért hővezetési tényező, λ [W/mK]	0,036	0,043	0,045	0,055	0,078	0,036	0,043	0,045	0,100	0,036	0,043	0,045	0,086

4. táblázat A laboratóriumi, a félüzemi I. és II. szériás geopolimer-EPS kompozit minták mért hővezetési tényezői a próbatestek összetételi arányainak feltüntetésével
Table 4. Results of the thermal conductivity measurements on lab and pilot scale geopolimer-EPS specimens

állapotokhoz tartozóan az elméleti, eredő hővezetési tényezők görbéit is (piros: D=0-0,4, szürke: D=0,5, illetve kék: D=0,6-1 színekkel jelölve), amelyeket a kétfázisú diszperz rendszerekre felírt univerzális hővezetés egyenletének (8) segítségével számítottunk ki. Ahogyan a 2. és 4.1. fejezetekben részleteztük, a 8. ábrán piros folytonos vonallal jelölt párhuzamos modell adja meg az eredő hővezetési tényező elméleti maximum értékeit, amely esetben az univerzális egyenletben bevezetett D-diszperzitás állapot értéke 0. Az elméleti minimum értékét a soros modell jelenti (kék folytonos vonal), a modellhez tartozó D-diszperzitás állapot értéke ebben az esetben pedig 1. Az elméleti minimum és maximum értékek között a vizsgált kétfázisú diszperz rendszerre vonatkozóan az egyes diszperzitás állapotoknak (D=0,1...0,9) megfelelően meghatározott eredő hővezetési tényezők görbéit láthatjuk szaggatott vonalakkal jelölve. A *8. ábra* tehát a mért és az új egyenlet (8) szerinti elméleti úton meghatározott eredő hővezetési tényezők összehasonlítására alkalmas. Az elméleti számítások esetében fontos megjegyeznünk, hogy az adott kompozitra jellemző diszperzitás állapot (D) értéke és a tiszta, geopolimer komponens hővezetési tényezője numerikus iterálással került meghatározásra. A tiszta EPS hővezetési tényezője a mérések alapján már ismert volt, azonban a geopolimer komponens hővezetési tényezőjének meghatározása sokkal nehezebb feladatot jelentett, ugyanis a tiszta geopolimer hővezetési tényezője leginkább az alkalmazott pernye szemcseméret-eloszlásától – részletesen a 2. fejezetben felsorolt egyéb paraméterektől –, ezáltal a tiszta, geopolimer komponens testsűrűségétől függ. Annak érdekében, hogy a laboratóriumi-, a félüzemi I. és II. szériás kompozit mintákhoz tartozó tényleges diszperzitás állapotot meg tudjuk állapítani, a mért és az egyes diszperzitás állapotokra vonatkozóan elméleti úton meghatározott eredő hővezetési tényezők értékei alapján kiszámítottuk a korrigált empirikus szórás értékeit is (szürke oszlopokkal szemléltetve). A kompozitra vonatkozó tényleges diszperzitás állapotot az a jellemző D érték fogja jellemezni, amely esetében a korrigált empirikus szórás értéke minimális.

A *8. ábra* bal oldalát tekintve az iterálással meghatározott tiszta geopolimer komponens hővezetési tényezőjét olvashatjuk le, amely a laboratóriumi szériás minták esetében 0,7 W/mK, ebben az esetben az EPS térfogataránya természetesen 0 %. Ugyanezen ábra jobb oldalán a tiszta EPS komponens hővezetési tényezőjét láthatjuk, amely a mérések alapján 0,036 W/mK értékre adódott. Egy köztes koncentrációjú keverék esetén az eredő hővezetési tényező értéke elsősorban attól függ, hogy milyen az EPS szemcsék diszpergáltsági állapota, mennyisége, illetve elhelyezkedése a geopolimer komponensben. A 8. ábrán az is jól látható, hogy a korrigált empirikus szórás értéke a D=0,8 esetében minimális, tehát a kompozit anyag diszpergáltsági állapota a soros hővezetési modellhez, azaz a kék folytonos vonallal jelölt elméleti minimum értékéhez esik közelebb.

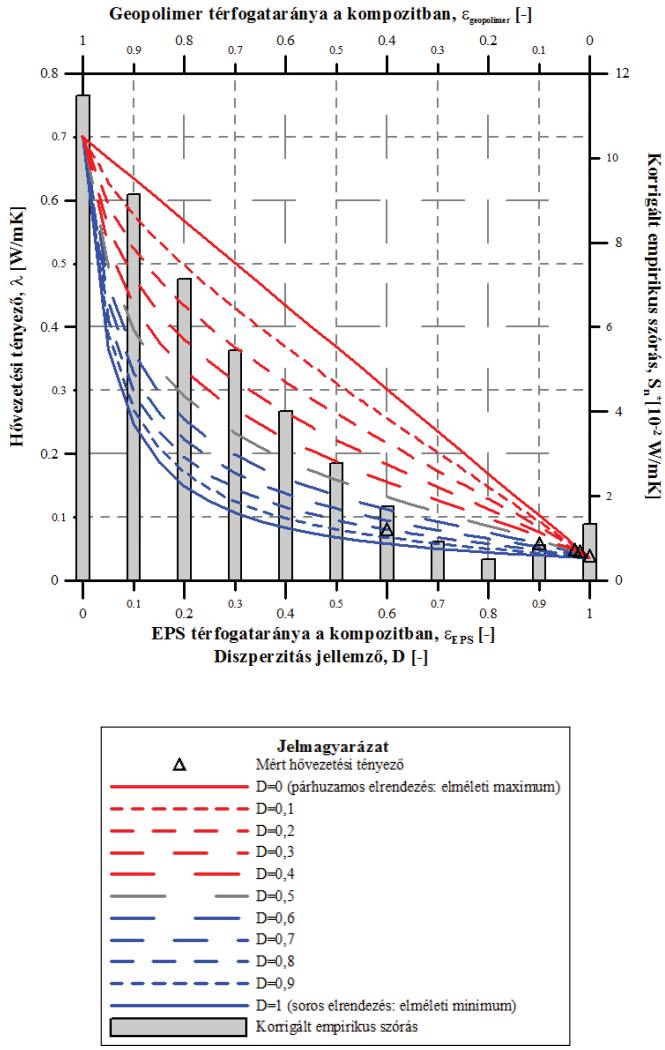

8. ábra A mért és az elméleti úton számított eredő hővezetési tényezők összehasonlítása a kompozitot alkotó komponensek térfogatarányának függvényében a laboratóriumi minták esetében
Fig. 8. Comparison of experimental- and theoretical resultant thermal conductivities of lab scale geopolimer-EPS composite materials as function of a component volumetric ratio

A laboratóriumi szériás minták esetében a 8. ábrához hasonlóan, elkészítettük a félüzemi I. és II. szériás mintákhoz tartozó ábrákat is (*9. és 10. ábra*).

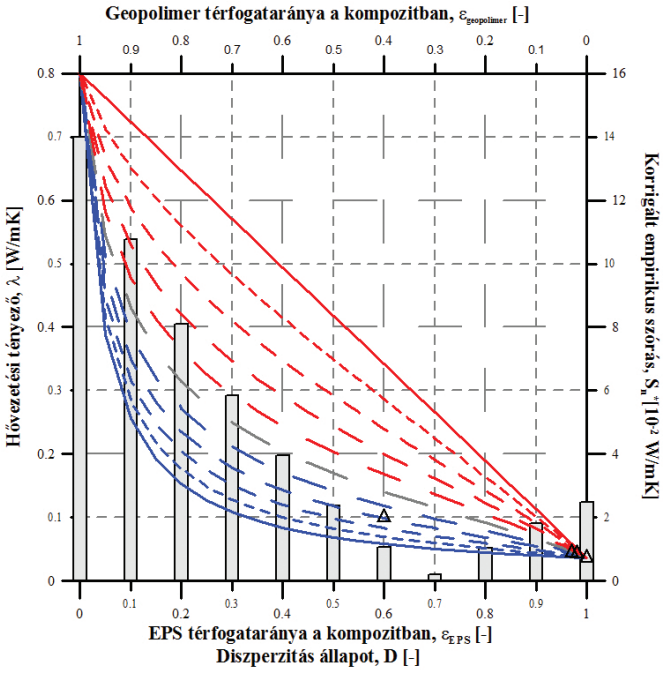

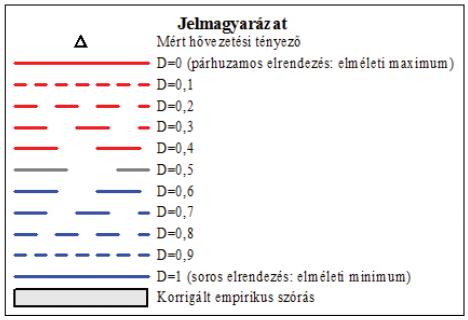

9. ábra A mért- és az elméleti úton számított eredő hővezetési tényezők összehasonlítása a kompozitot alkotó komponensek térfogatarányának függvényében a félüzemi I. szériás minták esetében

Fig. 9. Comparison of experimental- and theoretical resultent thermal conductivities of pilot scale geopolimer-EPS composite materials (I.) as function of a component volumetric ratio

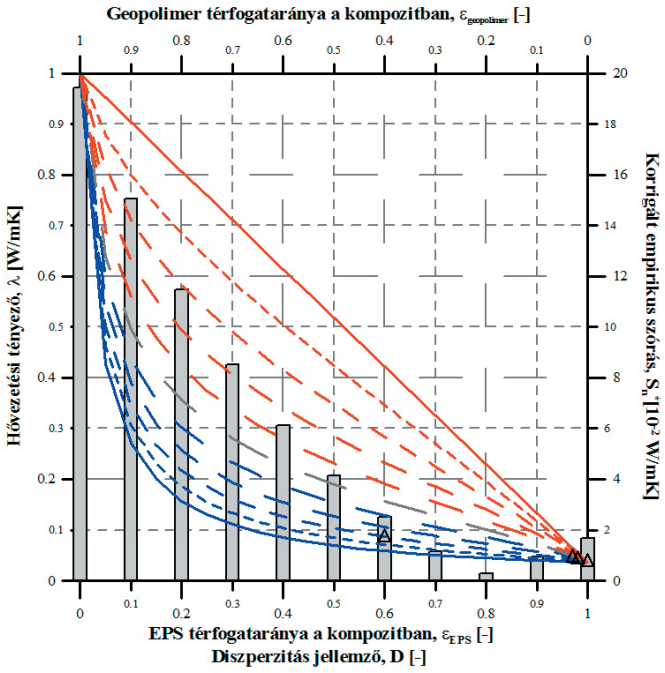

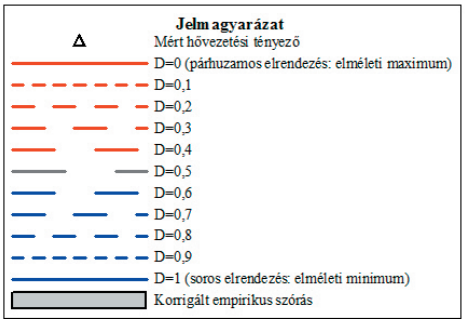

10. ábra A mért- és az elméleti úton számított eredő hővezetési tényezők összehasonlítása a kompozitot alkotó komponensek térfogatarányának függvényében a félüzemi II. szériás minták esetében

Fig. 10. Comparison of experimental- and theoretical resultant thermal conductivities of pilot scale geopolimer-EPS composite materials (II.) as function of a component volumetric ratio

A félüzemi I. szériás mintákra vonatkozóan az iterálással meghatározott geopolimer komponens hővezetési tényezője 0,8 W/mK-re adódott (*9. ábra*), amely magasabb, mint a laboratóriumi szériás minták esetében. Ennél a szériánál a geopolimer komponenst alkotó pernye már 10 m/m%-ban őrölt pernyét is tartalmazott, amely a testsűrűség növekedését eredményezte. A *9. ábra* alapján a félüzemi I. szériás kompozit mintákra jellemző diszperzitás állapot értéke 0,7-re adódott.

A félüzemi II. szériás minták eredményeit tekintve az iterálással meghatározott tiszta, geopolimer fázis hővezetési tényezője tovább nőtt, értéke 1 W/mK (*10. ábra*). A geopolimer komponensre vonatkozó, tovább növekvő hővezetési tényező magyarázata, hogy az ebben a szériában készült próbatestek esetében az alkalmazott pernye már 20 m/m%-ban tartalmazott őrölt pernyét. A diszperzitás állapot értéke a félüzemi II. szériás minták esetében a labaoratóriumi szériás mintákhoz hasonlóan 0,8.

5. Megállapítások

Összegzésképpen megállapítható, hogy az elkészült próbatesteken a mért- és az elméleti, eredő hővezetési tényező meghatározására felírt univerzális egyenlet (soros- és párhuzamos hővezetési modell összekapcsolása kétfázisú diszperz rendszerekre) által kapott értékek jól korrelálnak egymással. A kidolgozott módszer és a bevezetett új egyenlet alapján a geopolimer komponens ismeretlen hővezetési tényező értéke is kiszámítható volt, mert a mérésekre legjobban illeszkedő görbe (meghatározott D-diszperzitásállandó esetén), – amelyet a legkisebb korrigált empirikus szórás jellemez – kimetszi ezt az értéket a 0 % EPS tartalomhoz tartozóan. A várakozásoknak megfelelően, az őrölt pernye arányának növekedésével az iterálással meghatározott, tiszta geopolimer komponens hővezetési tényezőjének értéke is nő. A diszperzitás állapot tekintetében megállapítható, hogy mindhárom széria esetében az értéke 0,8 körüli volt, tehát nagyjából azonos

kevertségi állapotot sikerült elérni a próbatestek előállítása során. A kétfázisú rendszerre felírt eredő hővezetési tényező univerzális egyenletének segítségével – amennyiben ismert a két alkotó fázis hővezetési tényezője, illetve a komponensek aránya a kompozitban –, meghatározható a keverékre vonatkozó diszperzitás állapot értéke is, amellyel jellemezhető az egyik fázis másik fázisban való diszpergáltsági állapota.

Köszönetnyilvánítás

A tanulmány részben az „Innovatív, környezetbarát szigetelőanyag piacorientált kutatás-fejlesztése polisztirol másodnyersanyag hasznosításával - PIAC_13-1-2013-0124” megnevezésű projekt keretében a Magyar Kormány támogatásával, a Nemzeti Fejlesztési Ügynökség kezelésében, a Kutatási és Technológiai Innovációs Alap finanszírozásával valósult meg.

A tanulmány részben a „Fenntartható Nyersanyag-gazdálkodási Tematikus Hálózat – RING 2017” című, EFOP-3.6.2-16-2017-00010 jelű projekt részeként a Szechenyi2020 program keretében az Európai Unió támogatásával, az Európai Szociális Alap társfinanszírozásával valósult meg.

Felhasznált irodalom

[1] The US Department of Energy (2002). Insulation fact sheet with addendum on moisture control. DOE/CE-0180, USA.

[2] Caoa, X. – Liua, J. – Caoa, X. – Lia, Q. – Huc, E. – Fana, F. (2015): Study of the thermal insulation properties of the glass fiber boardused for interior building envelope. *Energy and Buildings 107*, pp. 49-58., https://doi.org/10.1016/j.enbuild.2015.08.007

[3] Roth, K. (2012): Soil Physics. Lecture Notes (v2.2). *Institute of Environmental Physics*, Heidelberg University, p. 391.

[4] Maxwell, J. C. (1865): A Dynamical Theory of the Electromagnetic Field. *Philosophical Transactions of the Royal Society of London*, Vol. 155.

[5] Rayleigh, L. (1892): On the influence of obstacles in rectangular order upon the properties of a medium. *Philosophical magazine*, Vol. 56, pp. 481-502.

[6] Zehner, P. – Schlunder, E. U. (1970): Thermal conductivity of granular materials at moderate temperatures (in German). *Chemie Ingr. Tech. 42*, pp. 933-941.

[7] Kandula, M. (2011): On the Effective Thermal Conductivity of Porous Packed Beds with Uniform Spherical Particles, *Journal of Porous Media*, Volume 14., pp. 919-926., https://doi.org/10.1615/JPorMedia.v14.i10.70

[8] Davidovits, J. (1994): Geopolymers: Inorganic polymeric new materials. *J. Mater. Educ.* 16, pp. 91-139.

[9] Davidovits, J. (2011): Geopolymer chemistry and application. *Institut Geopolimére 16 rue Galilée F-02100 Saint-Quentin France*, ISBN: 9782951482050, pp. 283-286.

[10] Komintsas, K. – Zaharaki, D. (2007): Geopolymerisation: A review and prospects for the mineral industry. *Mineral Engineering 20*, pp. 1261-1277., https://doi.org/10.1016/j.mineng.2007.07.011

[11] Mucsi G. – Csőke B. – Molnár Z. (2012): Alkáli aktivált pernyealapú kötőanyag vizsgálata. *HulladékOlnline* elektronikus folyóirat 3/1.

[12] Barbosa, V. F. F. – MacKenzie, K. J. D. (2003): Thermal behaviour of inorganic geopolymers and composites derived from sodium polysialate. *Mater. Res. Bull. 38*, pp. 319-331., https://doi.org/10.1016/S0025-5408(02)01022-X

[13] Barbosa, V. F. F. – MacKenzie, K. J. D. (1999): Synthesis and characterization of sodium polysialate inorganic polymer based on alumina and silica. In: *Geopolymer '99 Second International Conference*, Saint-Quentin, France, Thaumaturgo, C. (eds.), pp. 65-78.

[14] Panias, D. – Giannopoulou, I. P. – Perraki, T. (2007): Effect of synthesis parameters on the mechanical properties of fly ash-based geopolymers. *Colloids and Surfaces A: Physicochem. Eng. Aspects 301*, pp. 246-254.

[15] Mucsi G. – Kumar S. – Csőke B. – Kumar R. – Molnár Z. – Rácz Á. – Mádai F. – Debreczeni Á. (2015): Control of geopolymer properties by grinding of land filled fly ash. *International Journal of Mineral Processing 143*: pp. 50-58., https://doi.org/10.1016/j.minpro.2015.08.010

[16] Mádai F. – Kristály F. – Mucsi G. (2015): Microstructure, Mineralogy and Physical Properties of Ground Fly Ash Based Geopolymers. *Ceramics-Silikaty 59*:(1), pp. 70-79.

[17] Jelle, B. P. (2011): Traditional, state-of-the-art and future thermal building insulation materials and solutions – Properties, requirements and possibilities. *Energy and Buildings 43*, pp. 2549–2563., https://doi.org/10.1016/j.enbuild.2011.05.015

[18] Makai A. – Kiss J. – Mucsi G. (2016): The Possibilities of Polystyrene Waste Recycling. *XXX. microCAD International Multidisciplinary Scientific Conference*. Konferencia helye, ideje: Miskolc, Magyarország, 2016.04.21-2016.04.22. Miskolc: University of Miskolc, 2016. Paper A_9.

Ref.:
Magyar Tamás – **Faitli** József – **Szabó** Roland: *CGeopolimer-EPS kompozit szigetelő anyagok eredő hővezetési tényezőjének elméleti és kísérleti vizsgálata*
Építőanyag – Journal of Silicate Based and Composite Materials, Vol. 69, No. 3 (2017), 74–82. p.
https://doi.org/10.14382/epitoanyag-jsbcm.2017.13

Assessment of the fresh self-compacting concrete properties utilizing different types of additives

Abdulkader EL MIR ▪ BME Department of Construction Materials and Technologies ▪ abdelkader.elmir@hotmail.com
Salem Georges NEHME ▪ BME Department of Construction Materials and Technologies ▪ sgnehme@yahoo.com
Érkezett: 2017. 08. 18. ▪ Received: 18. 08. 2017. ▪ https://doi.org/10.14382/epitoanyag-jsbcm.2017.14

Abstract
Self-compacting concrete (SCC) is characterized by unique workability properties. Stagnation or segregation of SCC must be avoided to obtain a homogenous and stable mixture. When SCC is produced, it is essential that the concrete has all the adequate fresh properties at the time of placement. For a successful and reliable application of SCC, the predication of SCC fresh state properties is of crucial importance. This predictability is determined by the sensitivity of the rheological properties towards the affecting parameters in the mixture composition. Experimental work was conducted to clarify the effects of the volumetric water to powder ratio and additives on the behavior of SCC from the rheological point of view. Therefore, the aim of this paper is to analyze the effect of different types of additives and paste contents on the fresh state response of SCC; powder type. It was found that the additives can greatly influence the concrete workability. Along that, an extension of the workability window of SCC is updated according to the acceptance criterion for.
Keywords: Self-compacting concrete; Fresh properties; Sustainability; Additives
Kulcsszavak: Öntömörödő beton; Frissbeton jellemzők; Fenntarthatóság; Kiegészítő anyagok

Abdulkader EL MIR
MSc Civil Engineer, PhD student at BME, Department of Construction Materials and Technologies. Fields of interest: porosity of concrete, self compacting concretes, high performance concretes.

Salem Georges NEHME
MSc Civil Engineer, PhD, Associate Professor at BME, Department of Construction Materials and Technologies. Fields of interest: concrete technology, mass concrete, self-compacting concrete, fibre reinforced concrete, quality control of building materials, non-destructive testing, reinforced concrete structures, recycling of building materials.

1. Introduction

Self-compacting concrete (SCC) was developed to meet the durability requirements of concrete structures and tackle the casting difficulties in challenging geometries [1].

The primary fresh properties of SCC have been the filling ability, passing ability and segregation resistance. These properties must be taken into consideration in the design phase of SCC. The essential rheological properties of SCC have been based on low yield stress, moderate viscosity and retention of the kinetic energy of the flowable mixture by reducing the content of coarse aggregates. These measures have been required to reach the targeted filling ability, viscosity and segregation resistance. A low yield stress is achieved by the use of adequate dosages of superplasticizer. The flow characteristics are further modified by changing the aggregate volume fraction, coarse-to-fine aggregate volume, and the composition of the other ingredients. The viscosity has been controlled by the contents of the free water, superplasticizer, and the volume fraction of the solids in the mixture. The basic strategies for ensuring a moderate viscosity are based on either inclusion of high amounts of powder materials; i.e. total content of cementitious materials (referred to as powder type SCC) or addition of viscosity modifier agents (referred to as VMA type SCC) [2-5].

The filling ability is a fresh property of SCC that permits it to flow into the formwork under self-weight, and without vibration or any other means of consolidation. SCC filling ability is controlled through its rheological parameters such as the yield stress and the plastic viscosity. In general, high range water reducing admixture (HRWRA) improves the filling ability of SCC by reducing the yield stress and plastic viscosity. On the other hand, extreme dosages of HRWRA could result in very high fluidity that may cause concrete segregation. The use of additives is a great alternative to improve the segregation resistance. Therefore, the stability of the mixture could be maintained along with a good filling ability. Additives such as ground granulated blast-furnace slag, metakaolin (MK), silica fume (SF), fly ash and others have been used to produce SCC with a good filling ability [4-7].

Passing ability has been defined as the ability of fresh SCC to flow through small openings and fill the spaces within the reinforcements. In case of heavily reinforced structures, an adequate passing ability of SCC enables it to be placed and consolidated through dense reinforcing bars without any aggregate blockage [4]. The filling and passing ability have been directly connected. Also, the passing ability is affected by the number and spacing of the reinforcing bars. A good passing ability can be achieved by increasing the filling ability of fresh concrete and by limiting the segregation of coarse aggregates. *Table 1* summarizes the slump flow classes according to EFNARC recommendations and European standards [4, 7].

Slump flow classes	Mean slump flow diameter (mm)
SF1	550 – 650
SF2	660 – 750
SF3	760 – 850

Table 1. Slump flow classes [4, 7]
1. táblázat Roskadási terülési osztályok [4, 7]

The segregation resistance of SCC has been defined as its ability to remain uniform during and after placement without any loss of stability due to bleeding, mortar separation and coarse aggregate settlement [2, 4]. In particular, the distortion of aggregates becomes non-uniform if SCC did not have the necessary segregation resistance. A good segregation resistance of SCC could be obtained by the proper selection of material constituents and fractions. SCC with good segregation resistance quality is characterized by a high amount of powder material, a limited content of well-graded coarse aggregates, a small nominal maximum size of aggregate, and a low water to binder ratio [2,3]. Also, a viscosity modifying agent could assist in the segregation resistance of SCC. The characterization of the viscosity of SCC could be determined using the V-funnel time test. The test procedure has been clearly described in EFNARC guidelines [4].

Since there has been a large amount of recommendations and guidelines in the literature. *Table 2* and *3* help to summarize the viscosity classes (VF).

Viscosity class	V-funnel time (s)
VF1	≤ 8
VF2	9 – 25

Table 2. Viscosity classification for V-funnel time test [4, 7]
2. táblázat Viszkozitási osztályok tölcséres kifolyási vizsgálat alapján [4, 7]

References	Recommended V-funnel time (s)
BRL 1801 recommendations [8]	9-25
EFNARC guidelines [5]	6-12
Domone [9]	3-15

Table 3. Recommendation for V-funnel time by several authors
3. táblázat Tölcséres kifolyási idő javaslatok különböző szakirodalmi forrásokban

During the development of the mixture composition of SCC, the optimum workability ranges were established for the fresh state. *Fig. 1* illustrates the workability ranges as suggested by DAfStb [10]. This could help to limit the targeted values based on the upper and lower limits of the slump flow and for the V-funnel flow time.

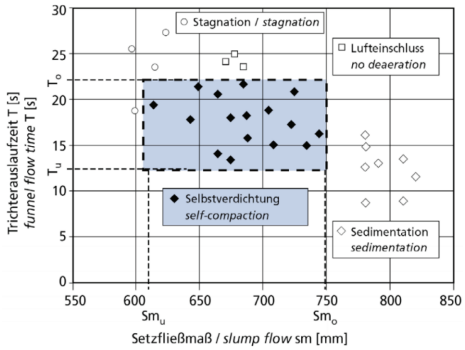

Fig. 1. Processing window for SCC as suggested by DAfStb [10]
1. ábra DAfStb [10] javaslat öntömörödő beton optimális reológiai jellemzőire

2. Experimental work

2.1 Materials, mix design and testing methods

A total of seventy-two SCC mixtures were designed and placed with common constant and variable parameters to obtain an objective evaluation between the fresh properties. Local natural quartz river sand and gravel with a maximum nominal size of 16 mm were used in the mixtures. Blast furnace slag cement CEM III/A 32.5 R (C) with a compressive strength grade of 32.5 MPa and a clinker content in the range of 41–58 wt% was applied for the present study. MK and SF were the supplementary cementitious materials (SCMs) implemented separately to enrich the mechanical properties. Waste perlite powder (WPP) originating from raw perlite rock was used as a filler material for SCC. Two types of WPP, which mainly differed in terms of their specific surface areas (WPP-C and WPP-SZ), were generated from cutting the raw perlite rock and applied with the following content (75% WPP-C and 25% WPP-SZ). Limestone powder (LP) was the non-pozzolanic filler applied in this study. The physical and chemical compositions of the mentioned fine materials are shown in *Table 4*, and grading fractions are provided in *Fig. 2*. A HRWRA, Sika Viscocrete 5, was used and adjusted to keep an SF3 slump flow class in a range of 740-850 mm [7].

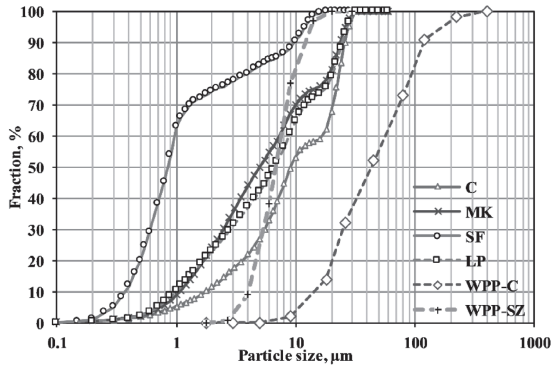

Fig. 2. Particle size distribution of the cement (C), metakaolin (MK), silica fume (SF), limestone powder (LP), waste perlite powder (WPP-C) and waste perlite powder (WPP-SZ)
2. ábra Szemeloszlási görbék; cement (C), metakaolin (MK), szilikapor (SF), mészkőpor (LP), hulladék perlit C (WPP-C), hulladék perlit SZ (WPP-SZ)

Chemical composition	C	MK	SF	LP	WPP-C	WPP-SZ
SiO_2	25.53	52.79	95.09	5.63	73.80	73.2
Al_2O_3	6.3	42.07	0.24	1.4	13.80	16.6
Fe_2O_3	2.29	1.25	0.06	0.9	1.57	2.6
CaO	55.59	0.37	0.91	50.32	1.17	1.06
MgO	4.05	0.38	0.32	0.65	0.11	0.2
SO_3	2.34	< 0.01	0.07	0.08	-	-
K_2O	0.78	1.22	0.51	0.29	4.01	3.5
Na_2O	0.33	0.02	0.2	0.07	2.66	1.5
TiO_2	0.28	0.2	< 0.01	0.08	0.083	0.09
P_2O_5	0.03	0.06	0.07	0.02	-	-
Physical properties						
Specific gravity	3.1	2.6	2.35	2.69	2.33	2.33
Specific surface area (cm^2/g)	3450	15244	20450	3470	843.3	4159
Loss on ignition (%)	2.15	1.59	2.49	40.55	2.8	1.21

Table 4. Chemical and physical characteristics of binders and filler materials
4. táblázat Alkalmazott anyagok kémiai és fizikai jellemzői

Mix ID	w/c_a	w/p_b	a/p_c	MK, kg/m^3	SF, kg/m^3	LP or WPP$_d$, kg/m^3	HRWRA, kg/m^3	V-funnel time, s	Slump flow, mm	Reference
T1	0.56	0.84	2.7			300	2.24	7.5	730	-
T2	0.50	0.85	2.8			260	2.34	14.6	580	-
T3	0.45	0.85	2.8			220	2.60	8.5	630	-
SCC-1	0.56	0.84	2.7	40		260	2.20	9.5	610	[13]
SCC-2	0.50	0.84	2.8	40		220	2.70	7.7	720	[13]
SCC-3	0.45	0.85	2.8	40	40	180	2.80	9.3	690	[13]
SCC-4	0.56	0.83	2.7		40	260	4.00	8.2	710	[13]
SCC-5	0.50	0.84	2.7		40	220	3.60	12.0	725	[13]
SCC-6	0.45	0.85	2.8			180	3.20	9.5	720	[13]
T4	0.56	0.90	3.0			260	0.96	16.5	530	-
T5	0.50	0.91	3.1			220	1.26	9.5	630	-
T6	0.45	0.92	3.1			180	3.20	3.7	890	-
SCC-7	0.56	0.90	3.0	40		220	2.40	13.2	680	[13]
SCC-8	0.50	0.91	3.0	40		180	2.63	6.8	820	[13]
SCC-9	0.45	0.92	3.1	40		140	4.00	7.0	850	[13]
SCC-10	0.56	0.89	3.0		40	220	2.88	10.8	835	[13]
SCC-11	0.50	0.90	3.0		40	180	3.13	8.4	835	[13]
SCC-12	0.45	0.91	3.0		40	140	3.70	9.9	820	[13]
R1	0.56	0.84	2.7			300	3.04	5.0	800	[11, 14]
R2	0.50	0.85	2.8			260	3.06	6.3	795	[11, 14]
R3	0.45	0.85	2.8			220	3.56	5.9	790	[11, 14]
M1	0.56	0.84	2.7	40		260	3.36	7.1	775	[11, 14]
M2	0.50	0.84	2.8	40		220	3.96	8.6	800	[11, 14]
M3	0.45	0.85	2.8	40		180	4.40	11.0	755	[11, 14]
S1	0.56	0.83	2.7		40	260	5.44	5.3	765	[11, 14]
S2	0.50	0.84	2.7		40	220	4.86	6.3	780	[11, 14]
S3	0.45	0.85	2.8		40	180	5.20	6.7	770	[11, 14]
R4	0.56	0.90	3.0			260	1.92	5.7	740	[11, 12]
R5	0.50	0.91	3.1			220	2.02	5.4	760	[11, 12]
R6	0.45	0.92	3.1			180	2.72	4.6	780	[11]
M4	0.56	0.90	3.0	40		220	2.72	9.7	775	[11, 12]
M5	0.50	0.91	3.0	40		180	2.92	10.3	780	[11, 12]
M6	0.45	0.92	3.1	40		140	4.00	8.6	810	[11]
S4	0.56	0.89	3.0		40	220	2.88	6.3	760	[11]
S5	0.50	0.90	3.0		40	180	3.17	5.0	770	[11]
S6	0.45	0.91	3.0		40	140	3.76	5.1	790	[11]
R7	0.56	1.01	3.5			200	1.74	5.2	780	[11]
R8	0.50	1.03	3.6			160	1.55	7.7	750	[11]
R9	0.45	1.04	3.6			120	1.76	5.9	770	[11]
M7	0.56	1.01	3.5	40		160	2.27	7.5	770	[11]
M8	0.50	1.02	3.6	40		120	2.34	8.7	785	[11]
M9	0.45	1.03	3.6	40		80	2.84	9.7	800	[11]
S7	0.56	1.00	3.5		40	160	2.31	6.7	765	[11]
S8	0.50	1.01	3.5		40	120	2.34	6.0	780	[11]
S9	0.45	1.02	3.6		40	80	2.72	3.6	850	[11]
NA1	0.56	0.84	2.7			300	3.68	4.9	790	[14]
NA2	0.50	0.85	2.8			260	3.42	6.1	760	[14]
NA3	0.45	0.85	2.8			220	3.92	6.1	780	[14]
MA1	0.56	0.84	2.7	40		260	4.80	9.5	790	[14]

Mix ID	w/c_a	w/p_b	a/p_c	MK, kg/m³	SF, kg/m³	LP or WPP_d, kg/m³	HRWRA, kg/m³	V-funnel time, s	Slump flow, mm	Reference
MA2	0.50	0.84	2.7	40		220	5.76	11.2	800	[14]
MA3	0.45	0.85	2.8	40		180	6.20	10.1	790	[14]
SA1	0.56	0.83	2.7		40	260	4.64	6.6	750	[14]
SA2	0.50	0.84	2.7		40	220	5.04	5.9	770	[14]
SA3	0.45	0.85	2.8		40	180	4.80	6.4	760	[14]
N1-P1	0.56	0.78	2.6			300	7.17	8.0	850	[15]
N2-P1	0.50	0.79	2.7			260	9.31	7.6	825	[15]
N3-P1	0.45	0.81	2.7			220	7.57	10.1	780	[15]
M1-P1	0.56	0.78	2.6	40		260	7.65	10.3	760	[15]
M2-P1	0.50	0.80	2.7	40		220	8.10	12.5	725	[15]
M3-P1	0.45	0.81	2.7	40		180	8.40	8.3	840	[15]
S1-P1	0.56	0.78	2.6		40	260	7.58	5.0	810	[15]
S2-P1	0.50	0.79	2.7		40	220	7.20	7.8	750	[15]
S3-P1	0.45	0.81	2.7		40	180	10.56	8.7	780	[15]
N1-P2	0.56	0.84	2.9			260	6.40	6.1	785	[12, 15]
N2-P2	0.50	0.85	3.0			220	7.56	5.5	800	[12, 15]
N3-P2	0.45	0.87	3.0			180	7.96	11.7	790	[15]
M1-P2	0.56	0.84	2.9	40		220	7.42	8.6	800	[12, 15]
M2-P2	0.50	0.86	3.0	40		180	8.10	6.4	790	[12, 15]
M3-P2	0.45	0.88	3.0	40		140	8.40	7.9	765	[15]
S1-P2	0.56	0.84	2.9		40	220	7.04	5.5	785	[15]
S2-P2	0.50	0.86	2.9		40	180	7.95	8.1	770	[15]
S3-P2	0.45	0.87	3.0		40	140	8.88	8.0	790	[15]

Table 5. Mixtures parameters
5. táblázat Keverék összetételek

To better imitate SCC types used in practice, several factors were considered in the mix design, including the total fine content (sum of cement, fillers, and SCM), SCMs, and filler type. The cement content (320, 360, 400 kg/m³), total fine content (620, 580, 520) kg/m³ and SCM (none, 40 kg/m³) dosages were set as variables. Aggregate particle-size distribution (three nominal grading fractions) was used as: sand 0/4 mm (45%), small gravel 4/8 mm (25%), and medium gravel 8/16 mm (30%). The amount of water (W), 180 kg/m³ was held as constant parameters. The mixture compositions of all the studied concretes is summarized in *Table 5*. In this study, the cement was defined as the main binder, with MK or SF as the SCMs, and WPP or LP as filler materials.

Because of the scope of the comparison, parameters related to the rheological properties of SCC mixtures were collected from previous studies [11-15].

To examine the adequacy of SCC mixtures deformability and viscosity, slump flow diameter and V-funnel time tests were carried out according to European Standards [16-17]. Refereeing to EFNARC guidelines for SCC [4], the aim of the study was to obtain a slump flow criterion which belong to SF3 category. The latter could be achieved by the proper addition of HRWRA and maximum aggregate size of 16 mm.

X_a: water to cement ratio by weight; X_b: volumetric water to powder ratio; X_c: Volumetric aggregates to powder ratio; X_d: Mixtures with WPP filler are those from N1-P1 to S3-P2

3. Range of SCC- "Window solution"

According to the measures from *Table 5*, a processing window similar to *Fig. 1* for the studied SCC mixtures was derived. Note that all studied mixtures were having the same grading fraction of aggregates with a maximum nominal size of 16 mm. Based on the positively evaluated SCC mixtures given in *Table 5* and the limitation given by EFNARC [4], an update for the processing window has been created (*Fig. 3*). This was done in four directions. First, the V-funnel time was enlarged to 14 s, to account for the higher friction and viscous SCC mixtures. Stagnation was noticed by visual inspection when the V-funnel time was greater than 14 s and the slump flow diameter was less than 600 mm. These mixtures were lacking the flow ability characteristic of SCC. Referring to *Fig. 4*, cases with stagnation corresponded to mixtures with low volumetric water to powder ratio (Mixtures T2 and T4; see *Table 5*), and by that, enhancing the plastic viscosity of the concrete. However these mixtures were reproduced with the same mixture composition but with a higher content of HRWRA (Mixtures R2 and R4), providing adequate flow ability and viscosity properties. Therefore, the requirement of V-funnel time greater than 14 s and slump flow less than 600 mm might be an appropriate limitation for a highly viscous SCC. Note that this workability window was applied to the range of temperature around 20 °C.

On the other hand, the slump flow axis is enlarged up to 850 mm, to account for the highly flow able mixtures. When

it comes to mixtures holding a V-funnel time less than 4 s, segregation of concrete was visually observed. The V-funnel time axis is enlarged also in the direction of shorter funnel times. Here at least, the mark of 4 s should be included as lower funnel time limit. It has been shown that SCC mixtures with low V-funnel time values, as low as 4.6 s (Mixture R6), could be successfully produced while also fulfilling all other requirements. This is of special relevance in particular for mixtures with low yield stress, thus with large slump flows.

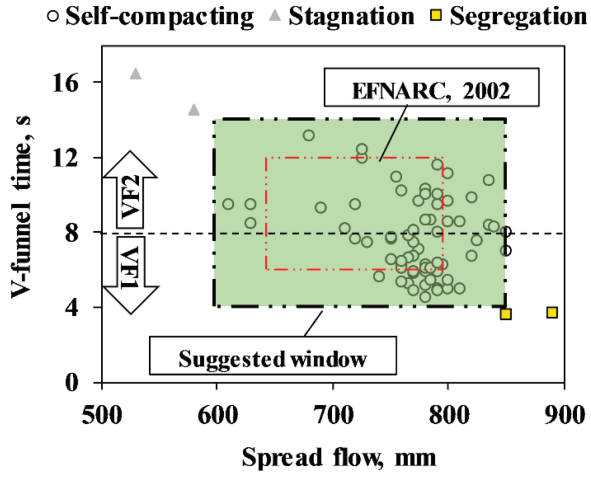

Fig. 3. Suggested processing window for SCC (corresponding data are collected from Table 5) in terms of V-funnel time and slump flow (in green); The red window corresponds to EFNARC limitations [4]

3. ábra Javasolt SCC reológiai jellemzők (az 5. táblázat adatai alapján) tölcséres kifolyási vizsgálatra és roskadási terülésre (zöld színnel); a piros vonallal határolt mező EFNARC [4] javaslat

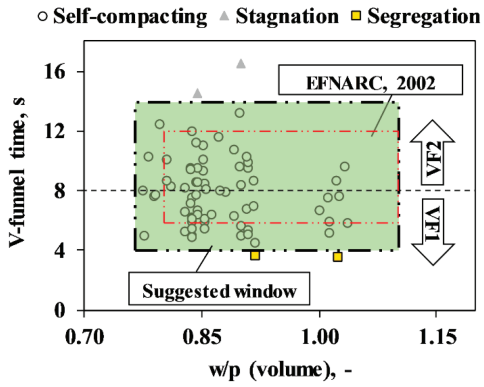

Fig. 4. Ssuggested processing window for SCC (corresponding data are collected from Table 5) in terms of V-funnel time and volumetric water to powder ratio (in green); The red window corresponds to EFNARC limitations [4]

4. ábra Javasolt SCC reológiai jellemzők (az 5. táblázat adatai alapján) tölcséres kifolyási vizsgálatra és térfogat szerinti víz-kötőanyag arányra vonatkozóan (zöld színnel); a piros vonallal határolt mező EFNARC [4] javaslat

The workability ranges for all collected SCC mixtures are shown in *Fig. 4* in terms of their volumetric water to powder ratio and V-funnel time. These mixtures differ in the total powder content, water to cement ratio, and different types of fillers and SCMs (see *Table 5*). It can be noticed that the workability ranges fluctuate between 750 and 850 mm since the targeted slump flow classification was SF3 for the following mixtures (starting with mixture "R1" to S3-P2; see *Table 5*). The exact position of the targeted workability highly depended on the implemented materials and their physical properties. EFNARC guidelines [3] classified the viscosity of SCC into two classes (see *Table 3*), *Figs. 3* and *4* compared all mixtures that were arranged according to their viscosity class (VF1 or VF2) [3]. It can be noticed that several mixtures shared the same slump flow value but with a different V-funnel time. For instance, if SCC mixture containing MK (mixture M2) or SF (mixture S2) were compared with their corresponding reference mixture R2, almost a common slump flow diameter (800 ±20 mm) is shown yet with significant difference in the V-funnel time value. MK enhanced the plastic viscosity of the mixture by 36% in V-funnel time, while adding SF does not appear to have any effect on the viscosity. Same response pattern is noticed for mixtures M5 and S5 as compared with mixture R5. The high cohesiveness of MK bearing mixtures seemed to be the reason for the high V-funnel time. On the other hand, shorter V-funnel times were recorded in SF incorporated mixtures. This could be explained by the ball bearing effect and additional lubrication provided by spherical and smooth-textured of SF particles. This finding is consistent with the following references [18-20].

To avoid the risk of segregation in SCC from excess amount of HRWRA, *Fig. 5* shows a curve where the minimum amount of HRWRA is indicated in accordance with the volumetric water to powder ratio derived from the data's in *Table 5*. The replacement of aggregates by fine powders (lower volumetric water to powder ratio) increased the HRWRA demand of when compared to mixtures with higher volumetric water to powder ratio. The risk of obtaining very viscous, unworkable SCC mixture could be reduced by increasing the w/p. The causes of the increase in HRWRA demand upon SCMs were studied by several researches [19]. They concluded that the very small size SCMs particles with high specific surface area, tendeed to agglomerate resulting in a high demand of HRWRA. Thereby, excess of HRWRA deflocculated the fine agglomerate particle, and lubricated the flowing system.

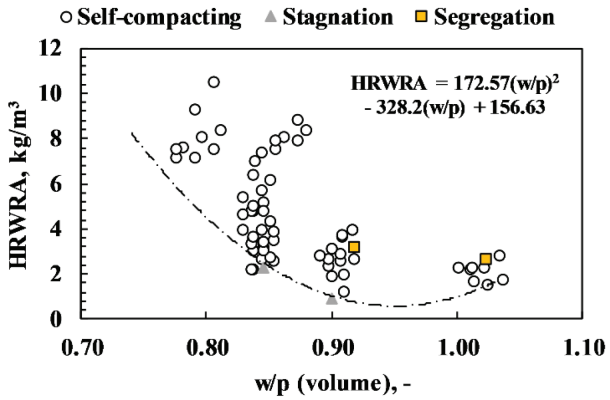

Fig. 5. Relationship between the high range water reducing admixture content and the volumetric water to powder ratio

5. ábra Összefüggés a folyósítószer adagolás és a térfogat szerinti víz-kötőanyag arány között

4. Conclusions

Self-compacting concrete (SCC) is sensitive to small changes in the material properties and proportions used in the mix design. An experimental approach for assessing the fresh

properties of SCC has been developed which represents the workability window of SCC in a diagram (slump flow diameter as a measure of the flow ability and the V-funnel flow time as a measure of the viscosity).

Based on the effects of the different mix design parameters (Volumetric water-to-powder ratio, high range water reducing admixture content and additives) on the fresh properties of examined SCC mixtures, the following conclusions could be drawn:

1. The optimum ranges of workability for self-compacting concrete SCC and its corresponding limits (stagnation and segregation) have to be tested and specified for the adequate fresh behaviour. That's could be achieved by varying the volumetric water to powder ratio and high range water reducing admixture. Thereby, this helped us to identify the range of workability within the workability window diagram.
2. V-funnel time of the SCC mixtures incorporating metakaolin was higher than of the mixtures with SF or reference mixtures.
   The minimum V-funnel time for VF1 classification should be 4 s; otherwise concrete segregation would occur.
3. For the same slump flow diameter values, mixtures containing metakaolin or silica fume showed higher demand of HRWRA as compared to that of.
4. reference mixtures.

5. Acknowledgment

Authors are grateful for the support of Sika Corp. and Lafarge for providing the necessary materials.

References

[1] Okamura, H. – Ouchi, M. (2003): Self-Compacting Concrete. *Journal of Advanced Concrete Technology*. Vol. 1, pp. 5-15.

[2] ACI Committee 237. (2007): Self-Consolidating Concrete. *American Concrete Institute.*

[3] Bonen, D. – Shah, S. P. (2004): Fresh and hardened properties of self-consolidating concrete. *Progress on Structural Engineering and Materials*. John Wiley & Sons, Ltd. Vol. 7, pp. 14-26. https://doi.org/10.1002/pse.186

[4] The European Guidelines for Self-Compacting Concrete. (2002): Specification and Guidelines for Self-Compacting Concrete.

[5] The European Guidelines for Self-Compacting Concrete. (2005): Specification, Production and Use.

[6] Johari, M. A. M. – Brooks, J. J. – Kabir, S. – Rivard, P. (2011): Influence of supplementary cementitious materials on engineering properties of high strength concrete. *Construction and Building Materials*. Vol. 25, pp. 2639-2648. https://doi.org/10.1016/j.conbuildmat.2010.12.013

[7] BSI Standards Publication. (2010): Concrete. Part 9: Additional Rules for Self-compacting concrete (SCC). *British Standard Institution*. BS EN 206-9:2010.

[8] BRL 1801. (2002): Aanvulling op de Nationale Beoordelingsrichtlijn Betonmortel betreffende het KOMO-productcertificaat voor Hoogvloeibare, verdichtungsarme en zelfverdichtende Betonmortel, *Certificatie-instelling BMC*, Gouda, The Netherlands (in Dutch).

[9] Domone, P. L. (2006): Self-compacting concrete: An analysis of 11 years of case studies. *Cement and Concrete Composites*. Vol. 28, pp. 197-208. https://doi.org/10.1016/j.cemconcomp.2005.10.003

[10] DAfStb. (2003): Richtlinie Selbstverdichtender Beton – Guideline for SCC, *Deutscher Ausschuss für Stahlbeton* (in German).

[11] El Mir, A. – Nehme, S. G. (2016): A comparative study on ultrasonic pulse velocity for normally vibrated and self-compacting concretes. *Concrete Structures*. Vol. 17, pp. 8-12.

[12] El Mir, A. – Nehme, S. G. (2017): Utilization of industrial waste perlite powder in self-compacting concrete. *Journal of Cleaner Production*. Vol. 156, pp. 507-517 https://doi.org/10.1016/j.jclepro.2017.04.103

[13] El Mir, A. – Nehme, S. G. (2015): Application of non-destructive test on self-compacting concrete, *IABSE Symposium Report*, I.A.B.S.E., vol. 105, pp. 1–8.

[14] El Mir, A. – Nehme, S. G. (2016): Comparison of durability performance of conventional and air-entrained self-compacting concrete modified by metakaolin and silica fume. *Proceedings of the 8th International RILEM Symposium on Self-Compacting concrete*, pp.61-71, Washington DC, U.S.A.

[15] El Mir, A. – Nehme, S. G. (2016): Application of chloride induced corrosion model for self-compacting concrete based on experimental data. *Proceedings of the 11th fib International PhD symposium in Civil Engineering*, pp.191-198, Tokyo, Japan.

[16] BSI Standards Publication. (2010): Testing fresh concrete Part 8: Self-compacting concrete — Slump-flow test. *British Standard Institution*. BS EN 12350-8:2010.

[17] BSI Standards Publication. (2010): Testing fresh concrete Part 9: Self-compacting concrete — V-funnel test. *British Standard Institution*. BS EN 12350-9:2010.

[18] Madandoust, R. – Mousavi, S. (2012): Fresh and hardened properties of self-compacting concrete containing metakaolin. *Construction and Building Materials*. Vol. 35, pp. 752-760. https://doi.org/10.1016/j.conbuildmat.2012.04.109

[19] Hassan, A. – Lachemi, M. – Hossain, K. (2012): Effect of metakaolin and silica fume on the durability of self-consolidating concrete. *Cement and Concrete Composites*. Vol. 34, pp. 801-807. https://doi.org/10.1016/j.cemconcomp.2012.02.013

[20] Ahari, R. – Erdem,T. – Ramyar, K. (2015): Time-dependent rheological characteristics of self-consolidating concrete containing various mineral admixtures. *Construction and Building Materials*. Vol. 88, pp. 134-142. https://doi.org/10.1016/j.conbuildmat.2015.04.015

Ref.:
El Mir, Abdulkader – **Nehme,** Salem Georges: *Assessment of the fresh self-compacting concrete properties utilizing different types of additives*
Építőanyag – Journal of Silicate Based and Composite Materials, Vol. 69, No. 3 (2017), 83–88. p.
https://doi.org/10.14382/epitoanyag-jsbcm.2017.14

Öntömörödő beton frissbeton-tulajdonságainak vizsgálata különböző kiegészítő anyagok alkalmazása esetén

Az öntömörödő betonok frissbeton tulajdonságai eltérnek a hagyományos betonokétól. Megfelelő beton összetétellel kell elérni, hogy a keverék homogén legyen, megfelelően mozogjon, és ne osztályozódjon szét. Az öntömörödő beton sikeres alkalmazásához szükség van a megfelelő frissbeton tulajdonságokra a bedolgozás során. Az öntömörödő betonok előállításának egyik legnagyobb kihívása az adott helyszínen elérhető alapanyagok minősége. Laboratóriumi kísérleteket végeztünk öntömörödő betonok reológiai tulajdonságainak vizsgálatára különböző cement kiegészítő anyagokkal. Jelen cikk azt vizsgálja, hogy a különböző cement kiegészítő anyagoknak milyen hatása van az öntömörödő betonok frissbeton tulajdonságaira. Az eredmények rávilágítottak, hogy a cement kiegészítő anyagok nagy hatást gyakorolnak a bedolgozhatóságra, és új elfogadási feltételek vezethetők be erre vonatkozóan.

Utilization of aluminium dross as asphalt filler

Zoltán SOÓS ▪ Department of Highway and Railway Engineering, Budapest University of Technology and Economics ▪ soos.zoltan.epito@gmail.com
Róbert GÉBER ▪ Institute of Ceramics and Polymer Engineering, University of Miskolc
Csaba TÓTH ▪ Department of Highway and Railway Engineering, Budapest University of Technology and Economics
Zsuzsanna IGAZVÖLGYI ▪ Department of Highway and Railway Engineering, Budapest University of Technology and Economics
Bella UDVARDI ▪ Institute of Ceramics and Polymer Engineering, University of Miskolc
Érkezett: 2017. 10. 15. ▪ Received: 15. 10. 2017. ▪ https://doi.org/10.14382/epitoanyag-jsbcm.2017.15

Abstract
Asphalt industry finds itself battling ongoing economic difficulties and an urge to achieve a more sustainable development and growth. It means constant searching is needed for alternative materials and possibilities to use recycled and processed waste materials in asphalt mixes as long as an expected level of performance and durability is provided.
Aluminium dross is a recyclable by-product of the casting process of melted aluminium. In this study an attempt was made to reveal the potentials of using aluminium dross as filler for asphalt wearing course mixes.
During the research, filler fractions (d<0.063 mm) were prepared by milling and microstructural tests were conducted both on the alternative and control filler for a better understanding of the materials and their composition. The effect of replacing limestone filler with aluminium dross filler on the performance of asphalt mixes was analysed by performance-based and performance related asphalt mechanical tests according to common standards. In the paper, the properties of fillers and various mechanical test results are presented and by interpreting the tests and results final conclusions are presented regarding the use of aluminium dross as filler in asphalt mixes.
Keywords: asphalt, aluminium dross, filler, rheology, stiffness
Kulcsszavak: aszfalt, alumínium salak, töltőanyag, reológia, merevség

Zoltán SOÓS PhD
Obtained PhD in 2017 at Department of Highway and Railway Engineering, BME. Member of the Hungarian Scientific Association for Transport. Research topics include testing and design of asphalt pavement materials and road structures with emphasis on fatigue behaviour and service life, performance and structural design. Takes part in lecturing at the University and as Deputy Head, in the work of the Pavement Laboratory since 2015.

Róbert GÉBER PhD
PhD since 2013. Working at the Institute of Ceramics and Polymer Engineering, University of Miskolc as assistant professor. Field of interests: testing of ceramics and composite materials including asphalt pavement materials. Member of the Scientific Society of the Silicate Industry, and author or co-author of 30 scientific articles.

Csaba TÓTH PhD, MBA
Member of the Hungarian Chamber of Engineers, the Hungarian Scientific Association for Transport and the Hungarian Road Society. Worked as Head of Division at Csongrád Couty Road Administration, then ÁKMI Kht. Involved in quality control of Hungarian road developments and both national and international researches as part of the Strabag concern. Had a role in several road overlay projects as engineering expert, designer and supervisor. Currently Assistant Professor and Head of Asphalt Unit at the Pavement Laboratory. Research field includes load bearing capacity of road structures and overlay design of flexible pavements.

Zsuzsanna IGAZVÖLGYI PhD
Assistant professor at the Department of Highway and Railway Engineering at BME since 2015 and member of the Pavement Laboratory since 2016. Main field of research involve asphalt materials, pavements and infrastructure design. Member of the Member of the Hungarian Scientific Association for Transport

Bella UDVARDI, BSc
Graduated in 2017 as material engineer, BSc. Currently working on her MSc diploma work.

1. Introduction

Handling, storage and wrecking of several waste material (construction and demolition waste, oil-drill cuttings, industrial by-products, etc.) is produced year by year which causes significant problems all over the world. To avoid these materials to damage the environment, they have to be recycled. Besides storing them on landfills, another way is the industrial utilization which may forward the reduction of yielding the available raw materials. A possible field of application of waste is building industry.

Utilization of different waste materials in concrete has been the subject of several research work. Aliabdo et al. [1] have done a comparative research work on the utilization of crushed clay brick in concrete. Kim [2] dealt with the application of waste concrete powder in self-consolidating concrete and its attribute characteristics. An extensive literature [3, 4, 5, 6, 7] is dealing with the application of concrete waste as aggregate in asphalt mixtures.

Utilization of different types of slags (basic oxygen furnace slag, steel slag) [8, 9, 10, 11,12] produced during various metallurgical processes as asphalt aggregate also showed good results. Based on the above mentioned research, it can be stated that mixtures made with slags have nearly the same performance as mixtures made with regular aggregates. Besides, slag – among others – improves resistance to plastic deformation and fatigue of asphalt pavements and it also decreases failure taking place due to sensitivity against

creative commons Attribution

moisture. Friction characteristics between vehicles and pavements can be improved by application of slag aggregates in wearing course and failure phenomena (rutting, cracking) can also be decreased in a great extent. By using slags, an improvement can be reached in the values of indirect tensile test, creep modulus and stripping.

Automotive casting was strengthened over the past decade in Hungary. A large amount of aluminium alloy is used during the aluminium melting process, significant amount of dross is formed due to oxidation process, which is a recyclable by-product. This waste material is produced during melting of alumina scrap; its general composition is: 15-30% Al_2O_3, 30-55% NaCl, 15-30% KCl and 5-7% of metallic aluminium and other impurities (carbides, nitrides, sulphides, phosphides). Several researches were made in the scope of recycling such drosses, mainly in the field of concrete technology [13, 14, 15]. These results showed that strength of the concrete made by substituting cement by 15% aluminium dross approached strength values of conventional concrete. Besides, alumina slag can be used for producing paver blocks and refractory blocks and can also be used where conventional concrete is applied.

2. Experimental

2.1 Sample preparation

Two types of fillers were used in this research. One was the aluminium dross, the other was limestone which was used as a reference material. The required particle size of fillers (d<0.063 mm) was obtained by sieving. Samples were then dried to weight constancy.

During the research the following tests were done on the fillers to reveal their properties. Mineralogical composition of samples was determined by X-ray powder diffraction (XRD) on a Rigaku MiniFlex II diffractometer. Particle size distribution (PSD) of the sieved material was measured by a Malvern Mastersizer X laser diffraction particle size analyzer in dry mode using air as dispersing media. Specific gravity of fillers was determined by pycnometer method according to MSZ EN 1097-7 standard. Hydrophilic coefficient was also determined by sedimentation method. Rigden Void of fillers were determined according to MSZ EN 1097-4 standard. For morphological tests Carl Zeiss EVO MA10 scanning electron microscope (SEM) was used. Specific surface area (SSA) of the powders (by BET-method) was determined by Micromeritics TriStar 3000 instrument.

2.2 Asphalt mix tests

The use of secondary and waste materials, slag and dross materials, to substitute certain parts of asphalt mixes is not a novelty in the past decades with a constant pursuit for a better sustainable environment, and asphalt industry [16, 17, 18]. Research has shown that the use, instead of disposal, of such by-products may be a promising way, amongst others, having at least no negative effects on performance while solving part of some issues related to the accessibility of virgin materials [19, 20].

In order to test performance of asphalt mixes having non-standard composition everyday methods as indirect tensile strength, wheel tracking, water sensitivity or fatigue may be inadequate, and require high volumes of the experimental material [21]. Furthermore as bituminous mixes have a rather complex, time and temperature behaviour, being a challenge to model and understand, multiple types of tests are required to assess performance at multiple testing conditions [22, 23, 24].

To obtain an overlook on the expected performance effect of replacing (part) of the pure limestone filler with dross simple performance test (SPT) as developed by NCHRP Project 9-19 was made on multiple temperatures, was made using a frequency sweep between 0.1 Hz – 25 Hz, due to the various possibilities to assess the data despite the simplicity of the test and the specimens [22].

To perform the preliminary tests three asphalt mix types have been made, one reference mix with 100% limestone as filler (Mix B), one mix made with 100% aluminium dross (Mix A), and one mix using 50% aluminium dross as filler (Mix C).

2.3. Mix composition

In order to assess the effect of the filler composition itself, asphalt wearing course mixes with nominal aggregate size of 11 mm (AC11) were made with the same aggregate composition, and the same binder type and content. Coarse aggregates have been washed and the dust loss has been compensated with fillers of the given three compositions. Thus, the total filler added was the filler by mix design and the mass of dust. *Fig. 1* shows the gradation of the asphalt mixes.

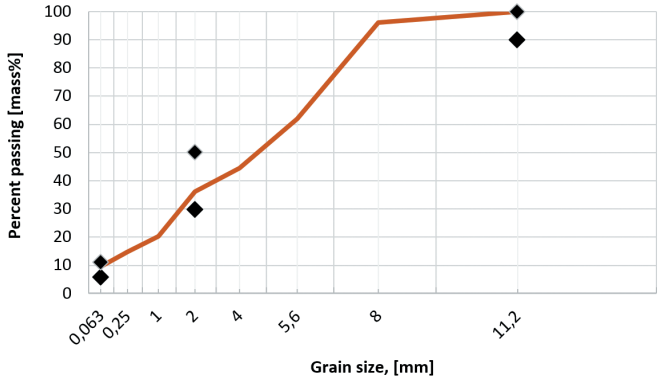

Fig. 1. Gradation of the asphalt mixes
1. ábra Aszfaltkeverékek szemeloszlása

Mixes were made using B50/70 standard bitumen with a content of 4.6%. Two gyratory specimens have been made for each mix, achieving a void of 4.7-4.8%, and the selected performance test has been conducted on all specimens.

2.4. Performance tests

Simple Performance Tests (SPT) were performed at temperatures between 0-40°C and frequencies between 0.1-25 Hz. Followed by proper conditioning intervals and resting times. Moduli and phase angle have been measured.

3. Results and discussion

3.1. Filler tests

Table 1 shows the results, which were obtained on fillers.

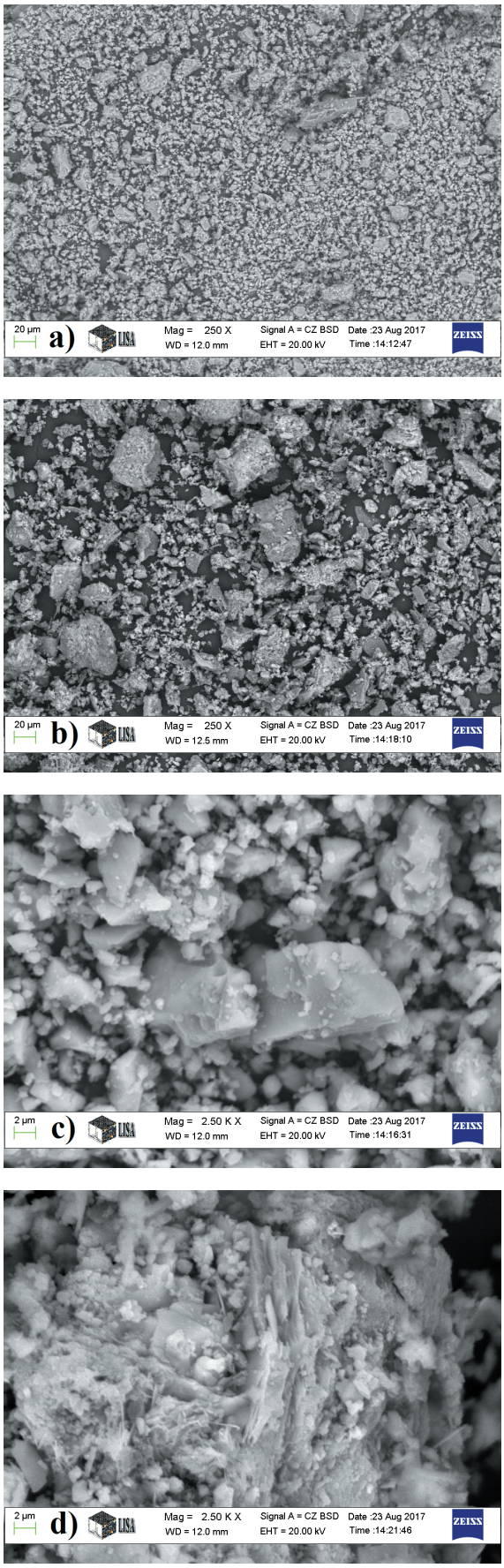

Fig. 2. Scanning electronmicrographs of fillers
2. ábra A töltőanyagok elektronmikroszkópos felvételei

Parameter	Unit	Limestone	Dross
Specific gravity, ρ	g/cm³	2.795	2.904
Average particle size, d_{50}	µm	13.77	24.96
Specific surface area, *SSA*	m²/g	1.55	1.03
Rigden Void, *RV*	vol%	47.2	45.7
Hydrophilic coefficient, η	-	0.75	0.67
Mineral composition	-	calcite ($CaCO_3$), quartz (SiO_2), dolomite ($CaMg(CO_3)_2$), muscovite 2M1 ($KAl_2(AlSi_3O_{10})(F,OH)_2$)	halite (NaCl), sylvite (KCl), potassium aluminium oxide ($K_{1.5}Al_{11}O_{17.25}$), corundum (Al_2O_3)

Table 1. Test results of fillers
1. táblázat Töltőanyagok vizsgálati eredményei

According to X-ray diffraction it can be stated that limestone build up mainly of calcite. Besides, this filler also contains dolomite, quartz and muscovite in small quantities. The main phases of dross are corundum and potassium aluminium oxide in a high quantities. Some salts, which are important components during the melting process of aluminium, like halite and sylvite have also identified during XRD tests.

The results of particle size analysis show that average particle size of limestone is smaller than aluminium dross ($d_{50\ limestone}$: 13.77 µm vs. $d_{50\ dross}$: 24.96 µm), so limestone contains much more fines than the other filler. Because of the higher quantities of fines in limestone, its specific surface is also higher. Electron micrographs (*Fig. 2*), taken in different magnifications also demonstrate the particle size distribution and the surficial features of fillers.

It is well observable that the surface of coarser particles of limestone is quite smooth and small calcite particles are stucked on it. Traces of open pores are not identified on the angular particles. In contrast, the surface of dross is much varied. Due to the mineral composition, smooth angular particles, plately parts and whisker-like surfaces can also be observed.

According to hydrophilic coefficient tests it can be stated that both fillers are hydrophobic which is favourable in asphalt technology.

3.2. Performance test results

3.2.1. Master curves

Master curves of viscoelastic materials are used to give a comprehensive assessment of the material stiffness for various temperatures and loading frequencies [25, 26]. Master curves can be constructed using the temperature-frequency superposition principle. Sigmoid model was used to construct the master curves of the specimens, based on Eq. (1).

$$log|E^*| = \delta + \frac{\alpha}{1+e^{\beta-\gamma\cdot log f_{red}}} \quad (1)$$

Where is the stiffness [MPa], α, β, γ, δ constants, f_{red} reduced frequency. Required constant parameters have been iterated

using the least squares method. Sigmoid functions obtained and the measured values are shown on *Fig. 3.*

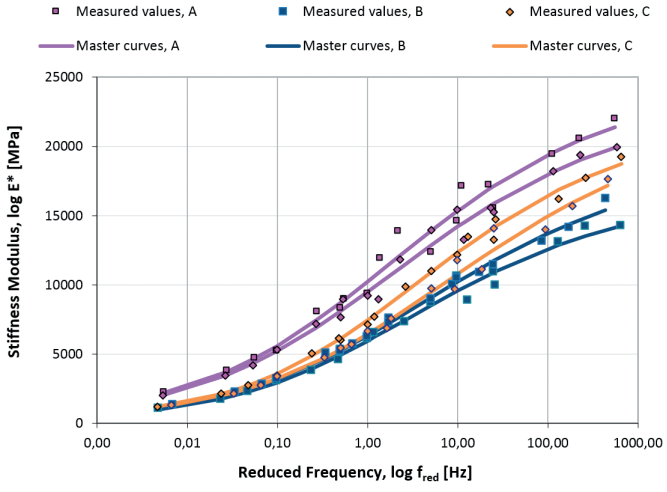

Fig. 3. Master curves of the tested specimens
3. ábra A vizsgált próbatestek mestergörbéi

As the master curves depict the mixes are stiffened by replacing limestone filler with aluminium dross. It is interesting to note that Mix A (100% dross) is significantly stiffer throughout the frequency range but Mix C (50% dross) is more similar to mix B (100% limestone) on high temperatures, and more like between the lesser two at high temperatures.

3.2.2. Black diagrams

Black diagrams give a good overlook on the viscoelastic properties of viscous materials such as bitumen and asphalt mixes [27, 28]. Plotting the measured complex moduli E* against the phase angle ϕ for each measurement in the case of all three mixes results in the Black diagram shown on *Fig. 4.* The tool developed to assess the rheological properties of binders may be, with limitations used for asphalt mixes as well, as viscoelastic materials.

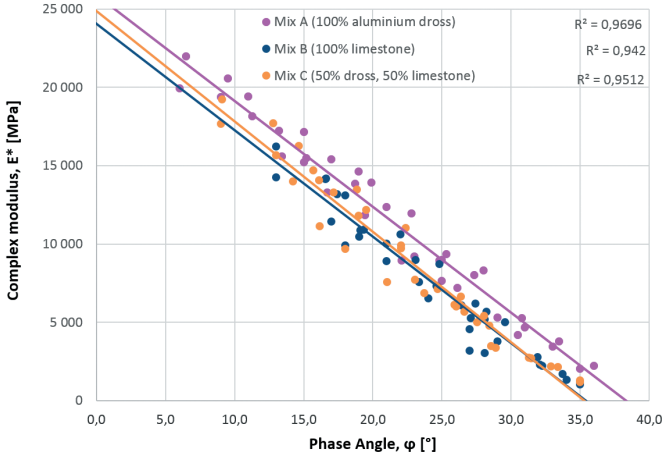

Fig. 4. Black diagrams of the tested specimens
4. ábra A vizsgált próbatestek Black diagramjai

The diagram enables the preliminary assessment of stiffness and non-linear behaviour. As the diagram shows, Mix A has higher stiffness values at given phase angles than the other two mixes, being similar at high phase angles, indicating that Mix A would perform more stiff at high temperatures and/or high frequencies. Notice that the 'return' of the curve is missing in all cases, which is normal taken into account the fact that asphalt mixes have been measured.

3.2.3. Cole-Cole diagrams

By using the known function of the complex modulus E* as shown on Eq. (2), storage modulus and loss modulus E_1 and E_2, respectively, can be calculated according to Eq. (3) and Eq. (4).

$$|E^*| = \frac{|\sigma_0|}{|\varepsilon_0|} = \sqrt{E_1^2 + E_2^2} \quad (2)$$

$$E_1 = E^* \cdot cos\varphi \quad (3)$$

$$E_2 = E^* \cdot sin\varphi \quad (4)$$

Where E* is the complex modulus, σ_0 is the maximum stress, ε_0 is the maximum strain, ϕ is the phase angle [°], E_1 is the storage modulus [MPa], and E_2 the loss modulus [MPa].

Storage modulus represents the part of the deforming stress that is stored in the deformed material and at the end of the deformation is used to cease the deformation. Loss modulus is the part of the stress that is usually lost during a deformation in heat form. Plotting the loss modulus against the storage modulus results the Cole-Cole diagram, as shown on *Fig. 5.*

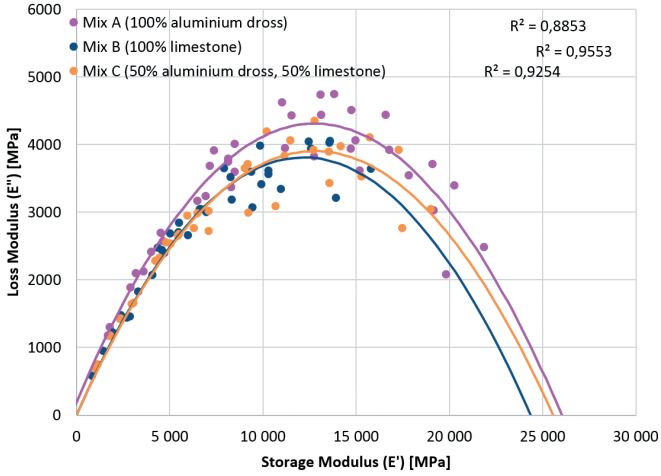

Fig. 5. Cole-Cole diagrams of the tested specimens
5. ábra A vizsgált próbatestek Cole-Cole diagramjai

The left part of the diagram indicates the mix behaviour at high temperatures, whereas the right hand side indicates the behaviour at low temperatures. Angle of given vectors pointing from zero to an arbitrary point on the graphs is called the loss angle.

The farther the intersections on the right side are, stiffer the materials are at low temperatures. As seen, the more the ratio of dross in the filler is, the stiffer the mix becomes in all temperature ranges compared to the limestone only filler. Furthermore, the stiffening effect is relatively higher on high temperatures than on low temperatures.

4. Conclusions

Simple Performance Test results have been conducted to preliminarily assess the effect of replacing limestone filler with

dross on the potential performance of the resulting asphalt mix. An interesting effect which requires further research is that the stiffening effect of the limestone is higher on low temperatures (low frequencies), and lower on low temperatures.

As seen, replacing the limestone filler with dross not only stiffens the asphalt mix, but increases the phase angle as well. However, replacing only 50%, i.e. only a part of the filler with dross may be a good direction for further research.

Acknowledgement

Present research is a part of GINOP -2.2.1-15-201600018 project.

The research results were presented in ic-rmm3 Conference, in Miskolc-Lillafüred, October, 2017.

References

[1] Aliabdo, A. A. – Abd-Elmoaty, M. A. – Hassan, H. H. (2014): Utilization of crushed clay brick in concrete industry. *Alexandria Engineering Journal*. Vol. 53, pp. 151-168, https://doi.org/10.1016/j.aej.2013.12.003

[2] Kim, Y-J. (2017): Quality properties of self-consolidating concrete mixed with waste concrete powder. *Construction and Building Materials*, Vol. 135, pp. 177-185, https://doi.org/10.1016/j.conbuildmat.2016.12.174

[3] Bhusal, S. – Li, X. – Wen, H. (2011): Evaluation of effects of Recycled Concrete Aggregate on volumetrics of Hot-Mix Asphalt. *Transportation Research Record: Journal of the Transportation Research Board*, Vol. 2205, pp. 36-39, https://doi.org/10.3141/2205-05

[4] Pasandín, A. R. – Pérez, I. (2014): Adhesion of Recycled Concrete Aggregates, demolition debris, and asphalt. P*etroleum Science and Technology*, Vol. 32. pp. 2584–91, http://dx.doi.org/10.1080/10916466.2013.856444

[5] Arabani, M. – Moghadas Nejad, F. – Azarhoosh, A. R. (2013): Laboratory evaluation of recycled waste concrete into asphalt mixtures. *International Journal of Pavement Engineering*, Vol. 14. No. 6. pp. 531-539, http://dx.doi.org/10.1080/10298436.2012.747685

[6] Paranavithana, S. – Mohajerani, A. (2006): Effects of recycled concrete aggregates on properties of asphalt concrete. *Resources, Conservation and Recycling*, Vol. 48. No.1. pp. 1-12, https://doi.org/10.1016/j.resconrec.2005.12.009

[7] Wong, Y. D. – Sun, D. D. – Lai, D. (2007): Value-added utilisation of recycled concrete in hot-mix asphalt. *Waste Management*, Vol. 27. No. 2. pp. 294-301, https://doi.org/10.1016/j.wasman.2006.02.001

[8] Yi, H. – Xu, G. – Cheng, H. – Wang, J. – Wan, Y. – Chen, H. (2012): An overview of utilization of steel slag. *Procedia Environmental Sciences*, Vol. 16. pp. 791-801, https://doi.org/10.1016/j.proenv.2012.10.108

[9] Chen, J. S. – Wei, S.-H. (2016): Engineering properties and performance of asphalt mixtures incorporating steel slag. *Construction and Building Materials*, Vol. 128. pp. 148–153, https://doi.org/10.1016/j.conbuildmat.2016.10.027

[10] Haritonovs, V. – Zaumanis, M. – Brencis, G. – Smirnovs, J. (2013): Asphalt Concrete Performance with Conventional and Waste Aggregates. *International Journal of Pavement Research and Technology*, Vol. 6. No. 5. pp. 505-510, http://dx.doi.org/10.6135/ijprt.org.tw/2013.6(5).505

[11] Asi, I. M. – Qasrawi, H. Y. – Shalabi, F. I. (2007): Use of steel slag aggregate in asphalt concrete mixes. *Canadian Journal of Civil Engineering*, Vol. 34. pp. 902–911

[12] Ézsiás, L. (2012): Kohászati salakok – a zúzottkövek megújult alternatívái az aszfaltgyártás területén. *Az Aszfalt*, Vol. 17. No.1 pp. 16-20

[13] Tsakiridis, P. E. (2012): Aluminium salt slag characterization and utilization – A review. *Journal of Hazardous Materials*, Vol. 217-218. pp. 1-10, https://doi.org/10.1016/j.jhazmat.2012.03.052

[14] Reddy, M. S. – Neeraja, D. (2016): Mechanical and durability aspects of concrete incorporating secondary aluminium slag. *Resource-Efficient Technologies*, Vol. 2. No. 4. pp. 225-232, https://doi.org/10.1016/j.reffit.2016.10.012

[15] Mailar, G. – Raghavendra, N. S. – Sreedhara, B. M. – Manu, D. S. – Hiremath, P. – Jayakesh, K. (2016): Investigation of concrete produced using recycled aluminium dross for hot weather concreting conditions. *Resource-Efficient Technologies*, Vol. 2. No. 2. pp. 68-80, https://doi.org/10.1016/j.reffit.2016.06.006

[16] Aziz, M. M. A. – Hainin, M. R. – Yaacob, H. – Ali, Z. – Chang, F.-L. – Adnan, A. M. (2014): Characterisation and utilisation of steel slag for the construction of roads and highways. *Materials Research Innovations*, Vol. 18. sup6, S6-255-S6-259, http://dx.doi.org/10.1179/1432891714Z.000000000967

[17] Krayushkina, K. – Prentkovskis, O. – Bieliatynskyi, A. – Junevičius, R. (2012): Use of steel slags in automobile road construction. *Transport*, Vol. 27. No. 2. pp. 129-137, http://dx.doi.org/10.3846/16484142.2012.690093

[18] Oluwasola, E. A. – Hainin, M. R. – Aziz, M. M. A. – Yaacob, H. – Warid, M. N. M. (2014): Potentials of steel slag and copper mine tailings as construction materials. *Materials Research Innovations*, Vol. 18. sup6, S6-250-S6-254, http://dx.doi.org/10.1179/1432891714Z.000000000966

[19] Ziari, H. – Khabiri, M. M. (2007): Preventive maintenance of flexible pavement and mechanical properties of steel slag asphalt. *Journal of Environmental Engineering and Landscape Management*, Vol.15. No.3. pp. 188-192, http://dx.doi.org/10.1080/16486897.2007.9636928

[20] Pasetto, M. – Baldo, N. (2012): Laboratory investigation on foamed bitumen bound mixtures made with steel slag, foundry sand, bottom ash and reclaimed asphalt pavement. *Road Materials and Pavement Design*, Vol. 13. No. 4. pp. 691-712, http://dx.doi.org/10.1080/14680629.2012.742629

[21] Mangiafico, S. – Di Benedetto, H. – Sauzéat, C. – Olard, F. – Pouget, S. – Planque, L. (2013): Influence of reclaimed asphalt pavement content on complex modulus of asphalt binder blends and corresponding mixes: experimental results and modelling. *Road Materials and Pavement Design*, Vol. 14:sup1, pp. 132-148, http://dx.doi.org/10.1080/14680629.2013.774751

[22] Di Benedetto, H. – Olard, F. – Sauzéat, C. – Delaporte, B. (2004): Linear viscoelastic behaviour of bituminous materials: From binders to mixes. *Road Materials and Pavement Design*, Vol. 5. sup1, pp. 163-202, http://dx.doi.org/10.1080/14680629.2004.9689992

[23] Olard, F. – Di Benedetto, H. (2003): General "2S2P1D " Model and Relation Between the Linear Viscoelastic Behaviours of Bituminous Binders and Mixes. *Road Materials and Pavement Design*, Vol. 4. No. 2. pp. 185-224, http://dx.doi.org/10.1080/14680629.2003.9689946

[24] Delaporte, B. – Di Benedetto, H. – Chaverot, P. – Gauthier, G. (2009): Linear Viscoelastic Properties of Bituminous Materials Including New Products Made with Ultrafine Particles. *Road Materials and Pavement Design*, Vol. 10. No. 1, pp. 7-38, http://dx.doi.org/10.1080/14680629.2009.9690180

[25] Chailleux, E. – Ramond, G. – Such, C. – de LaRoche, C. (2006): A mathematical-based master-curve construction method applied to complex modulus of bituminous materials. *Road Materials and Pavement Design*, Vol. 7. sup1, pp. 75-92, http://dx.doi.org/10.1080/14680629.2006.9690059

[26] Xu, Q. – Solaimanian, M. (2009): Modelling linear viscoelastic properties of asphalt concrete by the Huet–Sayegh model. *International Journal of Pavement Engineering*, Vol. 10. No. 6, pp. 401-422, http://dx.doi.org/10.1080/10298430802524784

[27] Biligiri, K. P. – Kaloush, K. – Uzan, J. (2010): Evaluation of asphalt mixtures' viscoelastic properties using phase angle relationships. *International Journal of Pavement Engineering*, Vol. 11. No.2. pp. 143-152, http://dx.doi.org/10.1080/10298430903033354

[28] Airey, G. D. (2002): Use of Black Diagrams to Identify Inconsistencies in Rheological Data, *Road Materials and Pavement Design*, Vol. 3. No. 4. pp. 403-424, http://dx.doi.org/10.1080/14680629.2002.9689933

Ref.:

Soós, Zoltán – **Géber,** Róbert – **Tóth,** Csaba – **Igazvölgyi,** Zsuzsanna – **Udvardi,** Bella: *Utilization of aluminium dross as asphalt filler* Építőanyag – Journal of Silicate Based and Composite Materials, Vol. 69, No. 3 (2017), 89–93. p. https://doi.org/10.14382/epitoanyag-jsbcm.2017.15

Utilization of aluminium dross as asphalt filler

Zoltán SOÓS ▪ Department of Highway and Railway Engineering, Budapest University of Technology and Economics ▪ soos.zoltan.epito@gmail.com
Róbert GÉBER ▪ Institute of Ceramics and Polymer Engineering, University of Miskolc
Csaba TÓTH ▪ Department of Highway and Railway Engineering, Budapest University of Technology and Economics
Zsuzsanna IGAZVÖLGYI ▪ Department of Highway and Railway Engineering, Budapest University of Technology and Economics
Bella UDVARDI ▪ Institute of Ceramics and Polymer Engineering, University of Miskolc
Érkezett: 2017. 10. 15. ▪ Received: 15. 10. 2017. ▪ https://doi.org/10.14382/epitoanyag-jsbcm.2017.15

Abstract
Asphalt industry finds itself battling ongoing economic difficulties and an urge to achieve a more sustainable development and growth. It means constant searching is needed for alternative materials and possibilities to use recycled and processed waste materials in asphalt mixes as long as an expected level of performance and durability is provided.
Aluminium dross is a recyclable by-product of the casting process of melted aluminium. In this study an attempt was made to reveal the potentials of using aluminium dross as filler for asphalt wearing course mixes.
During the research, filler fractions (d<0.063 mm) were prepared by milling and microstructural tests were conducted both on the alternative and control filler for a better understanding of the materials and their composition. The effect of replacing limestone filler with aluminium dross filler on the performance of asphalt mixes was analysed by performance-based and performance related asphalt mechanical tests according to common standards. In the paper, the properties of fillers and various mechanical test results are presented and by interpreting the tests and results final conclusions are presented regarding the use of aluminium dross as filler in asphalt mixes.
Keywords: asphalt, aluminium dross, filler, rheology, stiffness
Kulcsszavak: aszfalt, alumínium salak, töltőanyag, reológia, merevség

Zoltán SOÓS PhD
Obtained PhD in 2017 at Department of Highway and Railway Engineering, BME. Member of the Hungarian Scientific Association for Transport. Research topics include testing and design of asphalt pavement materials and road structures with emphasis on fatigue behaviour and service life, performance and structural design. Takes part in lecturing at the University and as Deputy Head, in the work of the Pavement Laboratory since 2015.

Róbert GÉBER PhD
PhD since 2013. Working at the Institute of Ceramics and Polymer Engineering, University of Miskolc as assistant professor. Field of interests: testing of ceramics and composite materials including asphalt pavement materials. Member of the Scientific Society of the Silicate Industry, and author or co-author of 30 scientific articles.

Csaba TÓTH PhD, MBA
Member of the Hungarian Chamber of Engineers, the Hungarian Scientific Association for Transport and the Hungarian Road Society. Worked as Head of Division at Csongrád Couty Road Administration, then ÁKMI Kht. Involved in quality control of Hungarian road developments and both national and international researches as part of the Strabag concern. Had a role in several road overlay projects as engineering expert, designer and supervisor. Currently Assistant Professor and Head of Asphalt Unit at the Pavement Laboratory. Research field includes load bearing capacity of road structures and overlay design of flexible pavements.

Zsuzsanna IGAZVÖLGYI PhD
Assistant professor at the Department of Highway and Railway Engineering at BME since 2015 and member of the Pavement Laboratory since 2016. Main field of research involve asphalt materials, pavements and infrastructure design. Member of the Member of the Hungarian Scientific Association for Transport

Bella UDVARDI, BSc
Graduated in 2017 as material engineer, BSc. Currently working on her MSc diploma work.

1. Introduction

Handling, storage and wrecking of several waste material (construction and demolition waste, oil-drill cuttings, industrial by-products, etc.) is produced year by year which causes significant problems all over the world. To avoid these materials to damage the environment, they have to be recycled. Besides storing them on landfills, another way is the industrial utilization which may forward the reduction of yielding the available raw materials. A possible field of application of waste is building industry.

Utilization of different waste materials in concrete has been the subject of several research work. Aliabdo et al. [1] have done a comparative research work on the utilization of crushed clay brick in concrete. Kim [2] dealt with the application of waste concrete powder in self-consolidating concrete and its attribute characteristics. An extensive literature [3, 4, 5, 6, 7] is dealing with the application of concrete waste as aggregate in asphalt mixtures.

Utilization of different types of slags (basic oxygen furnace slag, steel slag) [8, 9, 10, 11,12] produced during various metallurgical processes as asphalt aggregate also showed good results. Based on the above mentioned research, it can be stated that mixtures made with slags have nearly the same performance as mixtures made with regular aggregates. Besides, slag – among others – improves resistance to plastic deformation and fatigue of asphalt pavements and it also decreases failure taking place due to sensitivity against

creative commons Attribution

moisture. Friction characteristics between vehicles and pavements can be improved by application of slag aggregates in wearing course and failure phenomena (rutting, cracking) can also be decreased in a great extent. By using slags, an improvement can be reached in the values of indirect tensile test, creep modulus and stripping.

Automotive casting was strengthened over the past decade in Hungary. A large amount of aluminium alloy is used during the aluminium melting process, significant amount of dross is formed due to oxidation process, which is a recyclable by-product. This waste material is produced during melting of alumina scrap; its general composition is: 15-30% Al_2O_3, 30-55% NaCl, 15-30% KCl and 5-7% of metallic aluminium and other impurities (carbides, nitrides, sulphides, phosphides). Several researches were made in the scope of recycling such drosses, mainly in the field of concrete technology [13, 14, 15]. These results showed that strength of the concrete made by substituting cement by 15% aluminium dross approached strength values of conventional concrete. Besides, alumina slag can be used for producing paver blocks and refractory blocks and can also be used where conventional concrete is applied.

2. Experimental

2.1 Sample preparation

Two types of fillers were used in this research. One was the aluminium dross, the other was limestone which was used as a reference material. The required particle size of fillers (d<0.063 mm) was obtained by sieving. Samples were then dried to weight constancy.

During the research the following tests were done on the fillers to reveal their properties. Mineralogical composition of samples was determined by X-ray powder diffraction (XRD) on a Rigaku MiniFlex II diffractometer. Particle size distribution (PSD) of the sieved material was measured by a Malvern Mastersizer X laser diffraction particle size analyzer in dry mode using air as dispersing media. Specific gravity of fillers was determined by pycnometer method according to MSZ EN 1097-7 standard. Hydrophilic coefficient was also determined by sedimentation method. Rigden Void of fillers were determined according to MSZ EN 1097-4 standard. For morphological tests Carl Zeiss EVO MA10 scanning electron microscope (SEM) was used. Specific surface area (SSA) of the powders (by BET-method) was determined by Micromeritics TriStar 3000 instrument.

2.2 Asphalt mix tests

The use of secondary and waste materials, slag and dross materials, to substitute certain parts of asphalt mixes is not a novelty in the past decades with a constant pursuit for a better sustainable environment, and asphalt industry [16, 17, 18]. Research has shown that the use, instead of disposal, of such by-products may be a promising way, amongst others, having at least no negative effects on performance while solving part of some issues related to the accessibility of virgin materials [19, 20].

In order to test performance of asphalt mixes having non-standard composition everyday methods as indirect tensile strength, wheel tracking, water sensitivity or fatigue may be inadequate, and require high volumes of the experimental material [21]. Furthermore as bituminous mixes have a rather complex, time and temperature behaviour, being a challenge to model and understand, multiple types of tests are required to assess performance at multiple testing conditions [22, 23, 24].

To obtain an overlook on the expected performance effect of replacing (part) of the pure limestone filler with dross simple performance test (SPT) as developed by NCHRP Project 9-19 was made on multiple temperatures, was made using a frequency sweep between 0.1 Hz – 25 Hz, due to the various possibilities to assess the data despite the simplicity of the test and the specimens [22].

To perform the preliminary tests three asphalt mix types have been made, one reference mix with 100% limestone as filler (Mix B), one mix made with 100% aluminium dross (Mix A), and one mix using 50% aluminium dross as filler (Mix C).

2.3. Mix composition

In order to assess the effect of the filler composition itself, asphalt wearing course mixes with nominal aggregate size of 11 mm (AC11) were made with the same aggregate composition, and the same binder type and content. Coarse aggregates have been washed and the dust loss has been compensated with fillers of the given three compositions. Thus, the total filler added was the filler by mix design and the mass of dust. *Fig. 1* shows the gradation of the asphalt mixes.

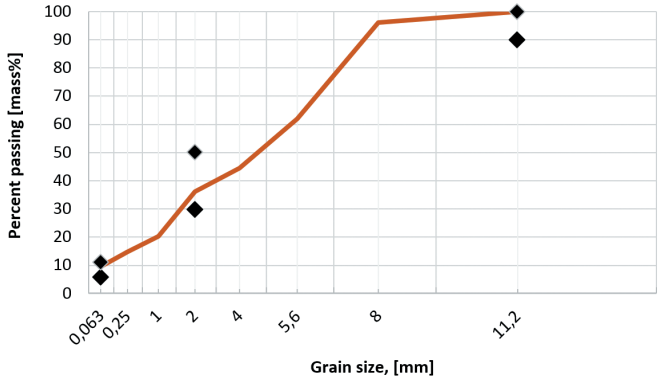

Fig. 1. Gradation of the asphalt mixes
1. ábra Aszfaltkeverékek szemeloszlása

Mixes were made using B50/70 standard bitumen with a content of 4.6%. Two gyratory specimens have been made for each mix, achieving a void of 4.7-4.8%, and the selected performance test has been conducted on all specimens.

2.4. Performance tests

Simple Performance Tests (SPT) were performed at temperatures between 0-40°C and frequencies between 0.1-25 Hz. Followed by proper conditioning intervals and resting times. Moduli and phase angle have been measured.

3. Results and discussion

3.1. Filler tests

Table 1 shows the results, which were obtained on fillers.

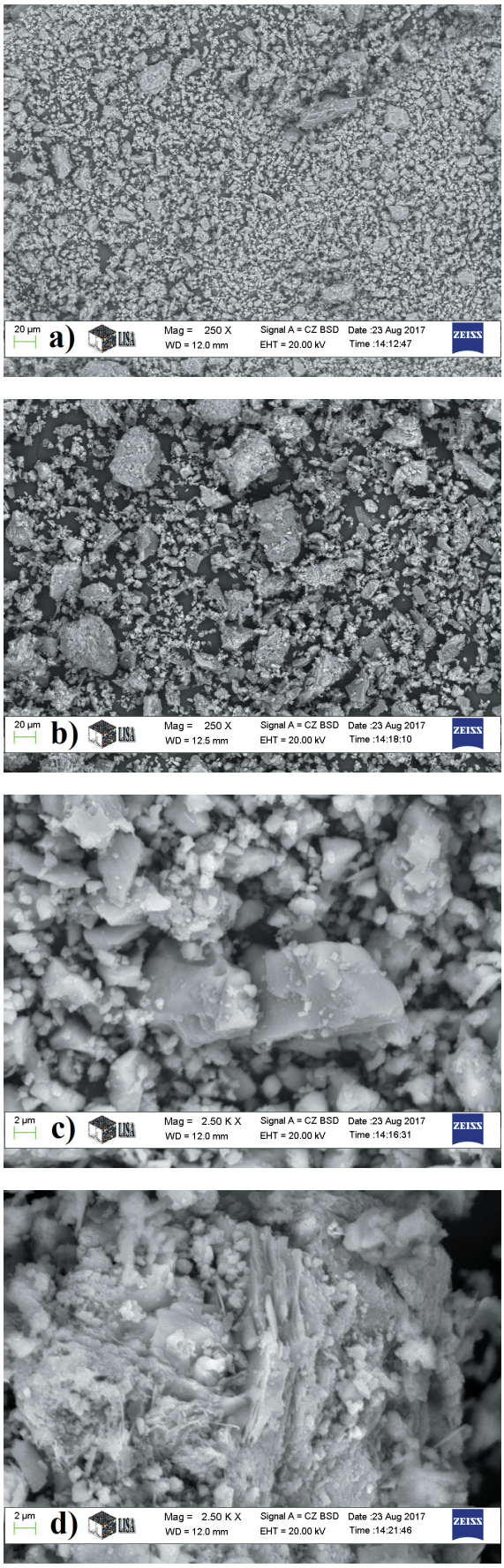

Fig. 2. Scanning electronmicrographs of fillers
2. ábra A töltőanyagok elektronmikroszkópos felvételei

Parameter	Unit	Limestone	Dross
Specific gravity, ρ	g/cm³	2.795	2.904
Average particle size, d_{50}	µm	13.77	24.96
Specific surface area, *SSA*	m²/g	1.55	1.03
Rigden Void, *RV*	vol%	47.2	45.7
Hydrophilic coefficient, η	-	0.75	0.67
Mineral composition	-	calcite ($CaCO_3$), quartz (SiO_2), dolomite ($CaMg(CO_3)_2$), muscovite 2M1 ($KAl_2(AlSi_3O_{10})(F,OH)_2$)	halite (NaCl), sylvite (KCl), potassium aluminium oxide ($K_{1.5}Al_{11}O_{17.25}$), corundum (Al_2O_3)

Table 1. Test results of fillers
1. táblázat Töltőanyagok vizsgálati eredményei

According to X-ray diffraction it can be stated that limestone build up mainly of calcite. Besides, this filler also contains dolomite, quartz and muscovite in small quantities. The main phases of dross are corundum and potassium aluminium oxide in a high quantities. Some salts, which are important components during the melting process of aluminium, like halite and sylvite have also identified during XRD tests.

The results of particle size analysis show that average particle size of limestone is smaller than aluminium dross ($d_{50\ limestone}$: 13.77 µm vs. $d_{50\ dross}$: 24.96 µm), so limestone contains much more fines than the other filler. Because of the higher quantities of fines in limestone, its specific surface is also higher. Electron micrographs (*Fig. 2*), taken in different magnifications also demonstrate the particle size distribution and the surficial features of fillers.

It is well observable that the surface of coarser particles of limestone is quite smooth and small calcite particles are stucked on it. Traces of open pores are not identified on the angular particles. In contrast, the surface of dross is much varied. Due to the mineral composition, smooth angular particles, plately parts and whisker-like surfaces can also be observed.

According to hydrophilic coefficient tests it can be stated that both fillers are hydrophobic which is favourable in asphalt technology.

3.2. Performance test results

3.2.1. Master curves

Master curves of viscoelastic materials are used to give a comprehensive assessment of the material stiffness for various temperatures and loading frequencies [25, 26]. Master curves can be constructed using the temperature-frequency superposition principle. Sigmoid model was used to construct the master curves of the specimens, based on Eq. (1).

$$log|E^*| = \delta + \frac{\alpha}{1+e^{\beta-\gamma\cdot log f_{red}}} \quad (1)$$

Where is the stiffness [MPa], α, β, γ, δ constants, f_{red} reduced frequency. Required constant parameters have been iterated

using the least squares method. Sigmoid functions obtained and the measured values are shown on *Fig. 3.*

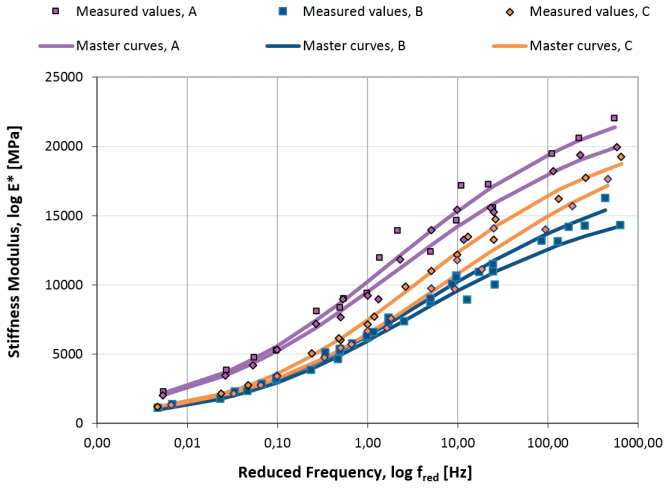

Fig. 3. Master curves of the tested specimens
3. ábra A vizsgált próbatestek mestergörbéi

As the master curves depict the mixes are stiffened by replacing limestone filler with aluminium dross. It is interesting to note that Mix A (100% dross) is significantly stiffer throughout the frequency range but Mix C (50% dross) is more similar to mix B (100% limestone) on high temperatures, and more like between the lesser two at high temperatures.

3.2.2. Black diagrams

Black diagrams give a good overlook on the viscoelastic properties of viscous materials such as bitumen and asphalt mixes [27, 28]. Plotting the measured complex moduli E* against the phase angle ϕ for each measurement in the case of all three mixes results in the Black diagram shown on *Fig. 4.* The tool developed to assess the rheological properties of binders may be, with limitations used for asphalt mixes as well, as viscoelastic materials.

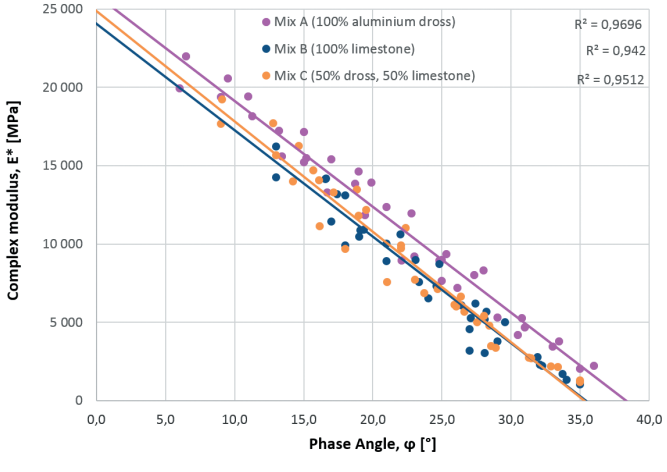

Fig. 4. Black diagrams of the tested specimens
4. ábra A vizsgált próbatestek Black diagramjai

The diagram enables the preliminary assessment of stiffness and non-linear behaviour. As the diagram shows, Mix A has higher stiffness values at given phase angles than the other two mixes, being similar at high phase angles, indicating that Mix A would perform more stiff at high temperatures and/or high frequencies. Notice that the 'return' of the curve is missing in all cases, which is normal taken into account the fact that asphalt mixes have been measured.

3.2.3. Cole-Cole diagrams

By using the known function of the complex modulus E* as shown on Eq. (2), storage modulus and loss modulus E_1 and E_2, respectively, can be calculated according to Eq. (3) and Eq. (4).

$$|E^*| = \frac{|\sigma_0|}{|\varepsilon_0|} = \sqrt{E_1^2 + E_2^2} \quad (2)$$

$$E_1 = E^* \cdot cos\varphi \quad (3)$$

$$E_2 = E^* \cdot sin\varphi \quad (4)$$

Where E* is the complex modulus, σ_0 is the maximum stress, ε_0 is the maximum strain, ϕ is the phase angle [°], E_1 is the storage modulus [MPa], and E_2 the loss modulus [MPa].

Storage modulus represents the part of the deforming stress that is stored in the deformed material and at the end of the deformation is used to cease the deformation. Loss modulus is the part of the stress that is usually lost during a deformation in heat form. Plotting the loss modulus against the storage modulus results the Cole-Cole diagram, as shown on *Fig. 5.*

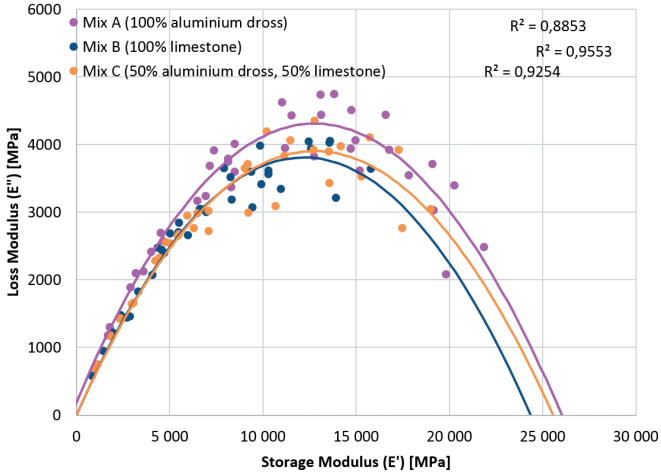

Fig. 5. Cole-Cole diagrams of the tested specimens
5. ábra A vizsgált próbatestek Cole-Cole diagramjai

The left part of the diagram indicates the mix behaviour at high temperatures, whereas the right hand side indicates the behaviour at low temperatures. Angle of given vectors pointing from zero to an arbitrary point on the graphs is called the loss angle.

The farther the intersections on the right side are, stiffer the materials are at low temperatures. As seen, the more the ratio of dross in the filler is, the stiffer the mix becomes in all temperature ranges compared to the limestone only filler. Furthermore, the stiffening effect is relatively higher on high temperatures than on low temperatures.

4. Conclusions

Simple Performance Test results have been conducted to preliminarily assess the effect of replacing limestone filler with

dross on the potential performance of the resulting asphalt mix. An interesting effect which requires further research is that the stiffening effect of the limestone is higher on low temperatures (low frequencies), and lower on low temperatures.

As seen, replacing the limestone filler with dross not only stiffens the asphalt mix, but increases the phase angle as well. However, replacing only 50%, i.e. only a part of the filler with dross may be a good direction for further research.

Acknowledgement

Present research is a part of GINOP -2.2.1-15-201600018 project.

The research results were presented in ic-rmm3 Conference, in Miskolc-Lillafüred, October, 2017.

References

[1] Aliabdo, A. A. – Abd-Elmoaty, M. A. – Hassan, H. H. (2014): Utilization of crushed clay brick in concrete industry. *Alexandria Engineering Journal*. Vol. 53, pp. 151-168, https://doi.org/10.1016/j.aej.2013.12.003

[2] Kim, Y-J. (2017): Quality properties of self-consolidating concrete mixed with waste concrete powder. *Construction and Building Materials*, Vol. 135, pp. 177-185, https://doi.org/10.1016/j.conbuildmat.2016.12.174

[3] Bhusal, S. – Li, X. – Wen, H. (2011): Evaluation of effects of Recycled Concrete Aggregate on volumetrics of Hot-Mix Asphalt. *Transportation Research Record: Journal of the Transportation Research Board*, Vol. 2205, pp. 36-39, https://doi.org/10.3141/2205-05

[4] Pasandín, A. R. – Pérez, I. (2014): Adhesion of Recycled Concrete Aggregates, demolition debris, and asphalt. P*etroleum Science and Technology*, Vol. 32. pp. 2584–91, http://dx.doi.org/10.1080/10916466.2013.856444

[5] Arabani, M. – Moghadas Nejad, F. – Azarhoosh, A. R. (2013): Laboratory evaluation of recycled waste concrete into asphalt mixtures. *International Journal of Pavement Engineering*, Vol. 14. No. 6. pp. 531-539, http://dx.doi.org/10.1080/10298436.2012.747685

[6] Paranavithana, S. – Mohajerani, A. (2006): Effects of recycled concrete aggregates on properties of asphalt concrete. *Resources, Conservation and Recycling*, Vol. 48. No.1. pp. 1-12, https://doi.org/10.1016/j.resconrec.2005.12.009

[7] Wong, Y. D. – Sun, D. D. – Lai, D. (2007): Value-added utilisation of recycled concrete in hot-mix asphalt. *Waste Management*, Vol. 27. No. 2. pp. 294-301, https://doi.org/10.1016/j.wasman.2006.02.001

[8] Yi, H. – Xu, G. – Cheng, H. – Wang, J. – Wan, Y. – Chen, H. (2012): An overview of utilization of steel slag. *Procedia Environmental Sciences*, Vol. 16. pp. 791-801, https://doi.org/10.1016/j.proenv.2012.10.108

[9] Chen, J. S. – Wei, S.-H. (2016): Engineering properties and performance of asphalt mixtures incorporating steel slag. *Construction and Building Materials*, Vol. 128. pp. 148–153, https://doi.org/10.1016/j.conbuildmat.2016.10.027

[10] Haritonovs, V. – Zaumanis, M. – Brencis, G. – Smirnovs, J. (2013): Asphalt Concrete Performance with Conventional and Waste Aggregates. *International Journal of Pavement Research and Technology*, Vol. 6. No. 5. pp. 505-510, http://dx.doi.org/10.6135/ijprt.org.tw/2013.6(5).505

[11] Asi, I. M. – Qasrawi, H. Y. – Shalabi, F. I. (2007): Use of steel slag aggregate in asphalt concrete mixes. *Canadian Journal of Civil Engineering*, Vol. 34. pp. 902–911

[12] Ézsiás, L. (2012): Kohászati salakok – a zúzottkövek megújult alternatívái az aszfaltgyártás területén. *Az Aszfalt*, Vol. 17. No.1 pp. 16-20

[13] Tsakiridis, P. E. (2012): Aluminium salt slag characterization and utilization – A review. *Journal of Hazardous Materials*, Vol. 217-218. pp. 1-10, https://doi.org/10.1016/j.jhazmat.2012.03.052

[14] Reddy, M. S. – Neeraja, D. (2016): Mechanical and durability aspects of concrete incorporating secondary aluminium slag. *Resource-Efficient Technologies*, Vol. 2. No. 4. pp. 225-232, https://doi.org/10.1016/j.reffit.2016.10.012

[15] Mailar, G. – Raghavendra, N. S. – Sreedhara, B. M. – Manu, D. S. – Hiremath, P. – Jayakesh, K. (2016): Investigation of concrete produced using recycled aluminium dross for hot weather concreting conditions. *Resource-Efficient Technologies*, Vol. 2. No. 2. pp. 68-80, https://doi.org/10.1016/j.reffit.2016.06.006

[16] Aziz, M. M. A. – Hainin, M. R. – Yaacob, H. – Ali, Z. – Chang, F.-L. – Adnan, A. M. (2014): Characterisation and utilisation of steel slag for the construction of roads and highways. *Materials Research Innovations*, Vol. 18. sup6, S6-255-S6-259, http://dx.doi.org/10.1179/1432891714Z.000000000967

[17] Krayushkina, K. – Prentkovskis, O. – Bieliatynskyi, A. – Junevičius, R. (2012): Use of steel slags in automobile road construction. *Transport*, Vol. 27. No. 2. pp. 129-137, http://dx.doi.org/10.3846/16484142.2012.690093

[18] Oluwasola, E. A. – Hainin, M. R. – Aziz, M. M. A. – Yaacob, H. – Warid, M. N. M. (2014): Potentials of steel slag and copper mine tailings as construction materials. *Materials Research Innovations*, Vol. 18. sup6, S6-250-S6-254, http://dx.doi.org/10.1179/1432891714Z.000000000966

[19] Ziari, H. – Khabiri, M. M. (2007): Preventive maintenance of flexible pavement and mechanical properties of steel slag asphalt. *Journal of Environmental Engineering and Landscape Management*, Vol.15. No.3. pp. 188-192, http://dx.doi.org/10.1080/16486897.2007.9636928

[20] Pasetto, M. – Baldo, N. (2012): Laboratory investigation on foamed bitumen bound mixtures made with steel slag, foundry sand, bottom ash and reclaimed asphalt pavement. *Road Materials and Pavement Design*, Vol. 13. No. 4. pp. 691-712, http://dx.doi.org/10.1080/14680629.2012.742629

[21] Mangiafico, S. – Di Benedetto, H. – Sauzéat, C. – Olard, F. – Pouget, S. – Planque, L. (2013): Influence of reclaimed asphalt pavement content on complex modulus of asphalt binder blends and corresponding mixes: experimental results and modelling. *Road Materials and Pavement Design*, Vol. 14:sup1, pp. 132-148, http://dx.doi.org/10.1080/14680629.2013.774751

[22] Di Benedetto, H. – Olard, F. – Sauzéat, C. – Delaporte, B. (2004): Linear viscoelastic behaviour of bituminous materials: From binders to mixes. *Road Materials and Pavement Design*, Vol. 5. sup1, pp. 163-202, http://dx.doi.org/10.1080/14680629.2004.9689992

[23] Olard, F. – Di Benedetto, H. (2003): General "2S2P1D " Model and Relation Between the Linear Viscoelastic Behaviours of Bituminous Binders and Mixes. *Road Materials and Pavement Design*, Vol. 4. No. 2. pp. 185-224, http://dx.doi.org/10.1080/14680629.2003.9689946

[24] Delaporte, B. – Di Benedetto, H. – Chaverot, P. – Gauthier, G. (2009): Linear Viscoelastic Properties of Bituminous Materials Including New Products Made with Ultrafine Particles. *Road Materials and Pavement Design*, Vol. 10. No. 1, pp. 7-38, http://dx.doi.org/10.1080/14680629.2009.9690180

[25] Chailleux, E. – Ramond, G. – Such, C. – de LaRoche, C. (2006): A mathematical-based master-curve construction method applied to complex modulus of bituminous materials. *Road Materials and Pavement Design*, Vol. 7. sup1, pp. 75-92, http://dx.doi.org/10.1080/14680629.2006.9690059

[26] Xu, Q. – Solaimanian, M. (2009): Modelling linear viscoelastic properties of asphalt concrete by the Huet–Sayegh model. *International Journal of Pavement Engineering*, Vol. 10. No. 6, pp. 401-422, http://dx.doi.org/10.1080/10298430802524784

[27] Biligiri, K. P. – Kaloush, K. – Uzan, J. (2010): Evaluation of asphalt mixtures' viscoelastic properties using phase angle relationships. *International Journal of Pavement Engineering*, Vol. 11. No.2. pp. 143-152, http://dx.doi.org/10.1080/10298430903033354

[28] Airey, G. D. (2002): Use of Black Diagrams to Identify Inconsistencies in Rheological Data, *Road Materials and Pavement Design*, Vol. 3. No. 4. pp. 403-424, http://dx.doi.org/10.1080/14680629.2002.9689933

Ref.:

Soós, Zoltán – **Géber,** Róbert – **Tóth,** Csaba – **Igazvölgyi,** Zsuzsanna – **Udvardi,** Bella: *Utilization of aluminium dross as asphalt filler* Építőanyag – Journal of Silicate Based and Composite Materials, Vol. 69, No. 3 (2017), 89–93. p. https://doi.org/10.14382/epitoanyag-jsbcm.2017.15

creative commons Attribution

Synthesis of alumino-silicates functionalized titanium as potential adsorbent: An industrial possibility

Fatima TARIQ ▪ Department of Environmental Sciences, Fatima Jinnah Women University ▪ Fatimatariq86@gmail.com
Uzaira RAFIQUE ▪ Department of Environmental Sciences, Fatima Jinnah Women University
Khurram YAQOOB ▪ School of Chemical and Material Engineering

Érkezett: 2017. 10. 19. ▪ Received: 19. 10. 2017. ▪ https://doi.org/10.14382/epitoanyag-jsbcm.2017.16

Abstract
Nowadays different industrial sectors are highly contributing towards the discharge of heavy metal in various environmental compartments and it is one of the foremost environmental concerns due to their high toxicity and destructive impacts impact on human health. The effluents discharge from paint and leather industries usually contain considerable amount of lead and mercury which ultimately accumulates along the food chain and causes severe damage to the nervous system. Various conventional methods have been reported in past for removing heavy metal ions such as chemical precipitation, electrochemical deposition, solvent extraction, and adsorption. Among these, adsorption is of immense importance because is effective and economical mean for environmental remediation. In past adsorption studies have focused on the development and application of different materials such as silica, titanium, vanadium, alumina, aluminosilicates, chitosan, starch and cyclodextrin. Currently designing of aluminosilicate based materials gain wide acceptance in multidisciplinary research areas due to their distinctive properties such as high surface area, pore volume and low operational cost. In addition to these characteristic features, the application of these materials are limited due to the lack of ion exchange ability which restricts the mobility of metals during adsorption phenomenon The present study was design to functionalize aluminosilicates with titanium chloride in order to enhance its ion exchange properties and ability to reduce harmful state of toxic metals for instance, Hg (II). The designed materials were subjected to different spectroscopic and quantitative techniques such as fourier transform infrared spectrometry, scanning electron microscopy, X-ray diffractometry. The objective of present research is to prepare aluminosilicate-Ti chloride by adapting simple sol-gel protocol and its functionalization with titanium chloride with simple mixing method. The synthesized material was applied adsorbent for entrapping different toxic pollutants such as mercury and lead. The formation of alumino-silicates-Ti material is confirmed by the presence of distinctive IR peak at 990 cm-1.Scanning electron microscopy of synthesized product reveals the microstructures with small void spaces. The X-ray diffractometry (XRD) pattern reflects the amorphous behaviour of synthesized material due to the modification of aluminosilicate with titanium chloride.
Keywords: aluminosilicates; lead; mercury; adsorbent; sol gel
Kulcsszavak: aluminoszilikátok; ólom; higany; adszorbens; szol gél

Fatima TARIQ
Ph.D research scholar from Fatima Jinnah Women University, The Mall, Pakistan is in progress of completing her Ph.D on synthesis of silica hybrids as nanocarrier for targeted drug delivery by functionalizing it with different gatekeepers. She won International Research Support Initiative Program by Higher Education Commission, Pakistan and joined University of Glasgow, UK , to work under co-supervision of Prof. Duncan Gregory on Synthesis and characterization of composite materials research project. Recently she went to University College London, UK to carry out part of her Ph.D research work on computational modelling and application of GULP software on my synthesized materials. She have published several papers which were published in conference proceedings. She filed a patent entitled Synthesis and application of agro- copolymers for treatment of organic pollutants from waste insulating fluid. Her research interests are in exploring the potential of synthesized composite materials in different fields especially in electrochemistry and adsorption under supervision of Prof. Uzaira Rafique (Dean of Faculty of Sciences, FJWU).

Prof. Uzaira RAFIQUE
Dean of Faculty of Sciences at FJWU Rawalpindi Pakistan. His interests in research group lie in synthesis, structure and physical properties of inorganic, organic, hybrid and composite materials. The basic aim of the group is to discover new materials with potential useful properties particularly with projected applications in field of environmental remediation and sustainable development.

Dr. Khurram YAQOOBE
Received his Bachelor of Metallurgical and Material Engineering degree from University of Engineering and Technology, Lahore, in 2007. Soon after, he was selected by Higher Education Commission of Pakistan for MS Leading to PhD studies from France. He completed his MS in Materials Science from Université Paul Sabatier Toulouse III, France, in 2009, and PhD degree in Materials Science from Université Paris Est, France, in 2012. His PhD research work was dedicated to the experimental determination and thermodynamic modeling of refractory metals phase diagrams. After successful completion of his PhD degree, he has joined Department of Materials Engineering, SCME- NUST as Assistant Professor in 2013.

1. Introduction

The rapid expansions of human and industrial activities lead towards unusual global and ecological changes. Under these circumstances, the major research target for scientists is to develop economical and environmental functional material by adapting simple methods [3]. Alumino-silicates become the centre of attention after modification with titanium chloride due to its remarkable physiochemical properties such as high surface area to volume ratio and ion exchangeable framework. The replacement of Si with Ti in the alumino-silicate framework enables the efficient use of these materials as adsorbent for remediation of heavy metals, volatile hazardous substances and persistent organic pollutants [9]. Recent reports in literature have revealed the possibility of producing alumino-silicate grafted zinc as nanotip by applying different synthesis routes including plasma sprayed, chemical vapour deposition and electrochemical anodization methods [4]. Within anodization method electrolyte and metal variations during synthesis process were reported and their effects were studied on the morphologies of synthesized materials. Additionally, these materials are preferable in the field of adsorption for the remediation of various dyes such as congo red and methylene blue, toxic metals (copper, nickel, lead and mercury) and organic pollutants (pesticides and PCBs) etc from industrial waste water samples [17]. *Wang* et al., 2012 reported about the modification of silica and alumina with zinc and vanadium to apply as adsorbent for efficient uptake of congo red from

textile wastewater samples. These materials exhibit significant removal of heavy metals due to its high porosity and large surface area. Similarly after the successive development of silica and alumina based materials, alumino-silicates were also synthesized and modified with zinc extracted from rice husk ashes and its potential application as adsorbent, drug carrier and catalyst due to its high cation exchange capacity. [13] The present study based on the synthesis of alumino-silicates followed by its modification with titanium chloride by using simple and economical sol-gel method. It is proposed that sol-gel method is a possible route to achieve particles with higher homogeneity and uniformity as compared to other conventional means. Based on the economical viability and environmental viable nature of the designed product it serve as nanocage for entrapping various toxic metallic species such as mercury and lead by batch adsorption experiments [6].

2. Materials and methods

The materials such as sodium silicate, aluminium nitrate, cetyl trimethylammonium bromide, titanium chloride and NaOH were the reagents used for synthesis and purchased commercially from Sigma Aldrich. Apparatus include a Flame Atomic Absorption spectrophotometer (AA 220, Varian) for metal analysis.

2.1. Synthesis of aluminosilicate products

Fig. 1 shows the synthesis of aluminosilicate by selecting sodium silicate and aluminium nitrate as primary precursors for silica and alumina. For this purpose, alumino-silicate was prepared by dissolving equal proportion (50:50) of both precursors (sodium silicate and aluminium nitrate) in 96 ml of double deionised water. The homogeneous solution is further processed by the addition of 0.7 ml of 2 M NaOH with continuous heating and vigorous stirring at 80 °C for 30 min followed by uniform mixing of 0.5 g of surfactants (CTAC). The resultant product was washed with distilled water, filtered and then dried in oven to get white powder which was calcined at 600 °C for 5hrs [19]. The prepared product was further functionalized with titanium chloride by simple mixing method. For this purpose, alumino-silicate fine powder was added in titanium chloride solution in (75:25) ratio. The titanium chloride was dissolved in less ratio because highest concentration of it will affect the integrity of the synthesized product [2].The prepared product was coded as AlSi-Ti.

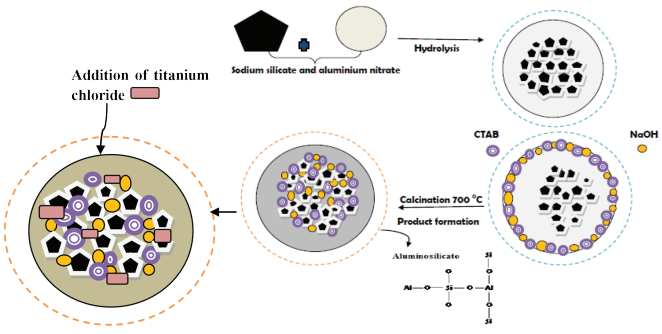

Fig. 1. Synthesis protocol of aluminosilicate material
1. ábra Aluminoszilikát szintézis protokollja

3. Characterization

The synthesized material is subjected to following characterization techniques such as FTIR (Fourier Transform Infrared (FTIR-8400 Schimadzu, Japan) spectrophotometer, XRD (STOE) and SEM (JEOL tsm-6490, Japan).

3.1 FTIR

The appearance of small IR peak at 997 cm^{-1} was assigned due to the formation of Si-O-Al bond after condensation of Si-OH and Al-OH groups [15] but modification of alumino-silicate with titanium chloride was confirmed by the shift in IR peak from 997 - 990 cm^{-1} and it corresponds to the stretching vibration of Si–O-Al [6] perturbed by the presence of vibration band of the -Al-O- Ti–O–Si [11] fragment The reduction in the intensity of IR peaks of alumino-silicate-Ti sample confirms the modification (see *Fig. 2*).

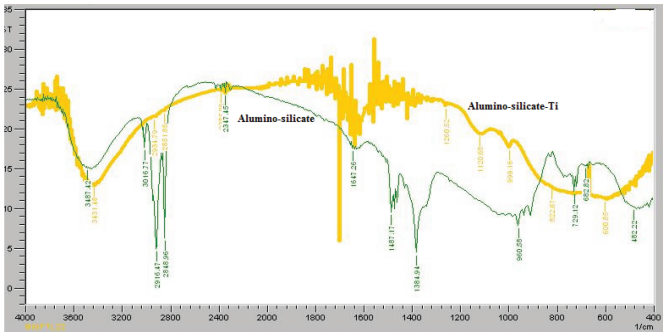

Fig 2. FTIR spectra of alumino-silicate-Ti based material
2. ábra Titán-aluminoszilikát FTIR spektruma

3.2 SEM

SEM micrograph of AlSi-Ti seen in *Fig. 3* showed aggregation of particles [12] with large number of small void spaces. This might be due to the effect of high calcinations temperature or attributed to the addition of cationic surfactant (CTAC) during synthesis [3].

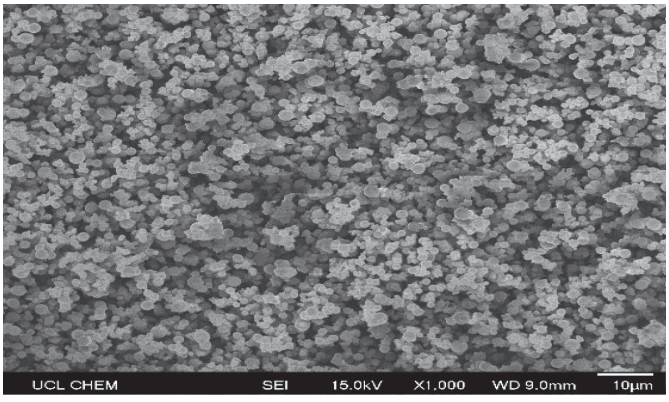

Fig. 3. SEM of alumino-silicate-Ti based material
3. ábra Titán-aluminoszilikát elektronmikroszkópos felvétele

3.3 XRD

XRD pattern of synthesized specimen scanned at 10-71of 2θ by steps of 0.015 with Cu K α radiation (λ = 1.54059) clearly depicts the amorphous nature of synthesized material. It is

attributed to the instability of AlSi-Ti material under acidic conditions which may lead towards the dealumination and collapse of atomic structures. This study is also supported by the Lin et al., 2015 which reveals the reduction in the peak intensities of the crystalline kaolinite after modification with Ti [18], see *Fig. 4.*

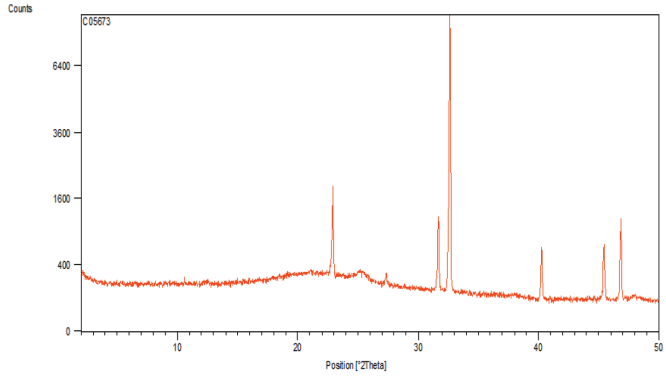

Fig. 4. XRD of alumino-silicate-Ti based material
4. ábra Titán-aluminoszilikát röntgendiffraktogramja

3.4 Batch adsorption experiment

A batch method was employed to study the adsorption of mercury and lead from aqueous solutions onto the alumino-silicate matrix. For this purposes, adsorbent 10 mg was suspended in 30, 50 and 70 mg/L of aqueous solution. Known concentration of adsorbate (0.03 mg/L) is pipetted out in the flask containing 10 mg of adsorbent (alumino-silicate), after the contact of every 5 minutes and analysed under flame atomic absorption spectrometer (FAAS) [7]. Percent removal was calculated by using following equation:

$$R\% = Ci\text{-}Co/Ci$$

It is proposed on the basis of experimental results that alumino-silicate modified titanium composites reveal (69%) uptake of mercury after 15 min minutes as shown in *Fig. 5.a*. It is attributed to the availability of large surface area and number of free binding sites. The slight decrease in adsorption of mercury ions is associated with the aggregation of available active sites as a result electrostatic attraction diminishes between mercury ions and adsorbent surface. This ultimately decreases the diffusion path length of the adsorbent [5].

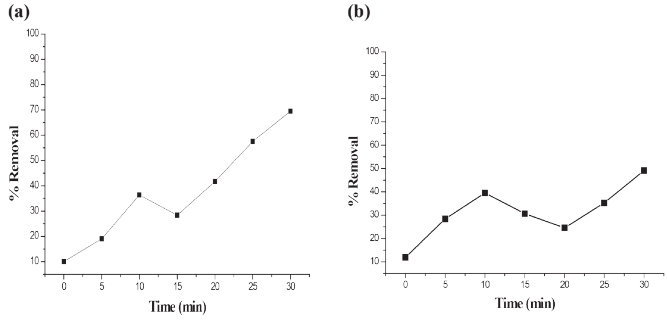

Fig. 5. Removal percentage (a) mercury, (b) lead
5. ábra Eltávolítási hányadok (a) higany, (b) ólom

In addition, gradual uptake of Pb^{2+} ion (49 %) was recorded at initial 10 minutes is due to the quick saturation of all empty active sites [1] and rapid diffusion of lead ions may accelerate the affinity of adsorbent to remove lead at initial time but quick decline after 10 minutes till 20 minutes is attributed to the surface coverage of alumino-silicate-Ti adsorbent results in the formation of metal complexes [10] (see *Fig. 5.b*)

Comparative adsorption studies of alumino-silicates-Ti with both metals (lead and mercury) suggest Accordingly it can be found that regular incline is observed for the removal of mercury as compared to lead. This adsorption trend is allied with the generation of unsaturated negative charge due to replacement of Si^{4+} ions by Al^{3+} in the alumino-silicate skeleton. Consequently lowest percentage removal of lead is observed at 20 min is due to the long-distance diffusion of lead ions into the internal pores of alumino-silicates framework [16].

4. Conclusions

It is concluded that physicochemical properties of alumino-silicates after modification serve as superior material for various industrial applications due to its bidimensional oxide structure in which the metals are bound to the Al_2O_3 matrix by SiO-Ti bond. Specific advantages to be gained by using alumino-silicates-Ti nanoparticles include facile adsorption, desorption, separations and catalysis applications. Efficient removal of mercury as compared to lead is observed due to the presence of electrostatic interactions between negative surfaces of alumino-silicates-Ti with the positive charge of mercury ion whereas removal of lead was significantly low due to the neutral charge of lead ion. It is concluded that modification of alumino-silicates with titanium chloride was favourable due to its potent economical and environmental benefits.

References

[1] K. M. Alam – P. A . Singh – C. S. Bodepudi – S. Pramanik (2011): Fabrication of hexagonally ordered nanopores in anodic alumina: An alternative pretreatment, *Surface Science Vol. 605*, No. 3–4, February 2011, pp. 441-449. https://doi.org/10.1016/j.susc.2010.11.015

[2] M. S. Auerbach – W. Fan – A. P. Monson (2015): Modelling the assembly of nanoporous silica materials, *International Reviews in Physical Chemistry*, Vol. 34, No. 1, pp. 35-70. https://doi.org/10.1080/0144235X.2014.988038

[3] G. Bellussi – R. Millini – E. Montanari – A. Carati – C. Rizzo – O. W. Parker – S. Zanardi (2012): A highly crystalline microporous hybrid organic–inorganic aluminosilicate resembling the AFI-type zeolite, *Chemical Communications, Vol. 48*, No. 59, pp. 7356-7358. https://doi.org/10.1039/C5SC01912E

[4] I. S. Chaturvedi (2013): Mercury Removal Using Al-Al Electrodes by Electrocoagulation, *International Journal of Modern Engineering Research, Vol. 3*, No. 1, pp. 109-115.

[5] Q. Chen – C. Boothroyd – M. A Soutar – T. X. Zeng (2010): Sol–gel nanocoating on commercial TiO2 nanopowder using ultrasound, *Journal of sol-gel science and technology, Vol. 53*, No. 1, pp. 115-120. https://doi.org/10.1007/s10971-009-2066-3

[6] S. Deng – M. Kurttepeli – J. D. Cott – D. S. Bals – C. Detavernier (2015): Porous nanostructured metal oxides synthesized through atomic layer deposition on a carbonaceous template followed by calcination, *Journal of Materials Chemistry A, Vol. 3*, No. 6, pp. 2642-2649. https://doi.org/10.1039/C4TA05165C

[7] S. Dursun – A. Pala (2007): Lead pollution removal from water using a natural zeolite, *J. Int. Environmental Application & Science*, Vol. 2, No. 2, pp. 11-19.

[8] J. Fang – I. Levchenko – K. Ostrikov (2014): Free-standing alumina nanobottles and nanotubes pre-integrated into nanoporous alumina membranes, *Science and Technology of Advanced Materials, Vol. 15*, No. 4. https://doi.org/10.1088/1468-6996/15/4/045004

[9] X. Lin – N. Zhao – P. Yan – P. H. Hu – F. J. Xu (2015): The shape and size effects of polycation functionalized silica nanoparticles on gene transfection, *Acta Biomaterialia*, Vol. 11, pp. 392. https://doi.org/10.1016/j.actbio.2014.09.004

[10] D. Macina – Z. Piwowarska – K. Tarach – K. Góra- Marek – J. Ryczkowski – L. Chmielarz (2016): Mesoporous silica materials modified with alumina polycations as catalysts for the synthesis of dimethyl ether from methanol, *Materials Research Bulletin, Vol. 74*, pp. 425-435. https://doi.org/10.1016/j.materresbull.2015.11.018

[11] Liu, M. – Hou, L. – Xi, B. – Zhao, Y. – Xia, X. (2013): Synthesis, characterization, and mercury adsorption properties of hybrid mesoporous aluminosilicate sieve prepared with fly ash, *Applied Surface Science, Vol. 273*, pp. 706-716. https://doi.org/10.1016/j.apsusc.2013.02.116

[12] P. Misaelides (2011): Application of natural zeolites in environmental remediation: A short review, *Microporous and Mesoporous Materials, Vol. 144*, No. 1, pp. 15-18. https://doi.org/10.1016/j.micromeso.2011.03.024

[13] L. Rita – T. Amit – G. Chandrashekhar (2011): Current trends in β-cyclodextrin based drug delivery systems, *International Journal of Research in Ayurveda and Pharmacy, Vol. 2*, pp. 1520-1526.

[14] S. Simon – M. Tămășan – T. Radu – V. Simon (211): Doping and calcination effect on nanostructured aluminosilicates processed by sol-gel route, *The European Physical Journal-Applied Physics, Vol. 55*, No. 3, pp. 10-15. https://doi.org/10.1051/epjap/2011100524

[15] J. R. Sohn – C. K. Lee (2007): Effect of V_2O_5 Modification in V_2O_5/TiO_2-ZrO_2 Catalysts on Their Surface Properties and Catalytic Activities for Acid Catalysis, *Bulletin of the Korean Chemical Society, Vol. 28*, No. 12, pp. 2459-2465. https://doi.org/10.5012/bkcs.2007.28.12.2459

[16] Y. Wang – C. Bryan – H. Xu – P. Pohl – Y. Yang – C. J. Brinker (2002): Interface Chemistry of Nanostructured Materials: Ion Adsorption on Mesoporous Alumina, *Journal of colloid and interface science, Vol. 254*, No. 1, pp. 23-30. https://doi.org/10.1006/jcis.2002.8571

[17] A. A. Warra (2011): Transition metal complexes and their application in drugs and cosmetics – A Review, *Journal of Chemical and Pharmaceutical Research, Vol. 3*, No. 4, pp. 951-958.

[18] Y. Yan – Y. Zhang – G. Meng – L. Zhang (2006): Synthesis of ZnO nanocrystals with novel hierarchical structures via atmosphere pressure physical vapor deposition method, *Journal of crystal growth, Vol. 294*, No. 2, pp. 184-190. https://doi.org/10.1016/j.jcrysgro.2006.06.049

[19] Y. Zhang – Z. He – H. Wang – L. Qi – G. Liu – X. Xang (2015): Applications of hollow nanomaterials in environmental remediation and monitoring: A review, *Frontiers of Environmental Science & Engineering, Vol. 9*, No. 5, pp. 770-783. https://doi.org/10.1007/s11783-015-0811-0

Ref.:
Tariq, Fatima – **Rafique,** Uzaira – **Yaqoob,** Khurram: *Synthesis of alumino-silicates functionalized titanium as potential adsorbent: An industrial possibility*
Építőanyag – Journal of Silicate Based and Composite Materials, Vol. 69, No. 3 (2017), 94–97. p.
https://doi.org/10.14382/epitoanyag-jsbcm.2017.16

On behalf of the Organising Committee, it is our great pleasure to invite you to attend the 28th International Conference on Organometallic Chemistry **(ICOMC-2018)** which will be held from **15th to 20th of July 2018** at the Congress and Exhibition Centre in the heart of the City of Florence, Italy, organised by the Institute of Chemistry of Organometallic Compounds **(ICCOM)** of the Italian National Research Council **(CNR)**, in association with the official PCO of the event, Adria Congrex Srl.

The Conference comes back to Italy after 30 years (Turin 1988) as a part of a series of biannual events with a long tradition. **ICOMC 2018** will provide a unique opportunity to present and disseminate all the main aspects of modern organometallic chemistry in a lively, multidisciplinary and modern environment. Companies are welcome to support the Conference by various kinds of Sponsorhip and will find exhibition space and other opportunities to advertise their products and activities.

The scientific program will be organised in parallel Lecture Sessions, focused on different aspects of traditional and emerging areas of organometallic chemistry and related applications. Student attendance will be encouraged by reduced fees and giving the possibility to showcase their results during two Poster Sessions and Flash Presentations. Top poster contributions will be shortlisted for Poster Prizes.

creative commons Attribution

Synthesis and characterization of aluminosilicates [$Zn_3(BTC)_2$] hybrid composite materials

Nosheen AYUB ▪ Department of Environmental Sciences, Faculty of Sciences, Fatima Jinnah Women University ▪ nosheen.ayub@gmail.com

Uzaira RAFIQUE ▪ Department of Environmental Sciences, Faculty of Sciences, Fatima Jinnah Women University

Érkezett: 2017. 10. 23. ▪ Received: 23. 10. 2017. ▪ https://doi.org/10.14382/epitoanyag-jsbcm.2017.17

Abstract

In this paper, hybrid composite materials based on metal organic framework [$Zn_3(BTC)_2$] at aluminosilicates (zeolite) was explored for the first time. The composite was successfully synthesized by hydrothermal crystallization of zeolite followed by Solvothermal growth of [$Zn_3(BTC)_2$] from its synthetic solution in the presence of dispersed zeolite particles. The synthesized materials were characterized by X-ray diffraction, Fourier transform infrared spectroscopy, scanning electron microscopy along with Energy dispersive X-ray spectrometric analysis. The XRD pattern exhibited the peaks characteristics of [$Zn_3(BTC)_2$] in composite material. It meant that Zn-BTC represented the major component of the composites, and it also suggested that the composites preserved the crystalline characters of parent Zn-BTC. The results of FTIR and SEM/EDX further confirm the successful synthesis of composite hybrid material aluminosilicates with [$Zn_3(BTC)_2$].

Keywords: Hybrid; zeolite; synthesis.
Kulcsszavak: Hibrid; zeolit; szintézis.

Nosheen AYUB

Ph. D. candidate at Fatima Jinnah Women University (FJWU) Rawalpindi Pakistan. She won International Research Support Initiative Program by Higher Education Commission, Pakistan and joined University of Glasgow, UK, to work under co-supervision of Prof. Duncan Gregory on Synthesis and characterization of composite materials research project. Her research interests are in exploring the potential of synthesized composite materials in different fields especially in electrochemistry and adsorption under supervision of Prof. Uzaira Rafique (Dean of Faculty of Sciences, FJWU).

Prof. Uzaira RAFIQUE

Dean of Faculty of Sciences at FJWU Rawalpindi Pakistan. His interests in research group lie in synthesis, structure and physical properties of inorganic, organic, hybrid and composite materials. The basic aim of the group is to discover new materials with potential useful properties particularly with projected applications in field of environmental remediation and sustainable development.

1. Introduction

Metal-organic frameworks (MOFs) are an emerging class of crystalline porous materials [1]. MOF consists of secondary building units, metal ions that act as lattice nodes, connected by organic linkers who impart high porosity and form modular structure [2]. Therefore by changing the connectivity of the inorganic moiety and nature of organic linker a wide structural diversity and highly designable pore sizes and shapes in MOFs are expected, which endow MOFs with tunable cavity architectures and properties. MOFs are synthesized both traditional and rather specific methods like use of microwave, ultrasonic, mechanochemical and electrochemical processing [3]. The reproducibility of the results of synthesis and post synthetic treatment of the produced samples is of critical importance. MOFs are most often functionalized to make them appropriate for precise application. In current era, the possibility to vary the structure porosity, topology and elemental composition (the Al:Si ratio and isomorphous substitution of transition metal atoms in tetrahedral positions) has rendered zeolites and their derivatives the most suitable materials for use in a variety of applications: in gas adsorption and separation, catalysis, photocatalysis. Zeolites and their derivatives have been addressed in experimental and theoretical studies.

However, MOFs are superior to zeolites in various respects; in specific, a characteristic feature of MOFs is the large surface area. Metal-organic frameworks vary from zeolites in numerous key aspects. The key change of the MOFs is an extensive diversity and variability of their structure in combination with lower topological restrictions on the formation of porous three-dimensional frameworks. A significant number of new MOF structures synthesized every year confirms this variability and heightened interest in their potential application areas. Zeolites are built of tetrahedral fragments, and differences in their topology are based on a finite number of secondary structure elements, whereas inorganic secondary building units of MOFs can be both a separate metal atom or a more or less complicated cluster and one, two or three-dimensional extended inorganic substructures.

Nevertheless thermal stability of zeolite is higher than MOF. So, Assimilation of MOFs with different functional materials is a very effective and viable approach to further improve MOF performance [4] or present innovative functionality for practical use [5]. Thus far, various MOF composites have been fruitfully prepared by assembling MOFs and functional species, including graphene, carbon nanotubes (CNTs), metal oxides, complexes, and have shown remarkable performance in catalysis [6], photo-induced H_2 generation [7], proton conduction [8], and so on. In these MOF composites, the individual functions of the MOFs and functional materials synergistically fuse together not only to deliver multifunctionality as a whole but also to produce new physical and chemical properties that are not present in the individual components [9]. The combination of MOFs and other functional materials has extended their applications. Moreover, research on high-performance MOF hybrids with sophisticated architectures, in combination with enrichment of the MOF database, has led to new design tactics for MOF composites.

In this study, we report the synthesis of zeolite-MOF composite materials by Solvothermal growth of MOF on the surface of zeolite. Zeolite-MOF composite has the potential to be novel and useful porous system the variety of application, as the inorganic zeolite component imparts the advantages of their higher thermal, mechanical and structural stability

and the organic MOF imparts specific functionality and high flexibility.

2. Experimental

2.1. Materials

Analytical grade reagents, such as aluminumisopropoixde, sodium hydroxide (NaOH), tetraethyl ammonium hydroxide (TEAOH), Tetraethylorthosilicate (TEOS), Ammonium nitrate (NH_4NO_3), 1,3,5-benzenetricarboxylicacid or trimesic acid (TMA), zinc nitrate hexahydrate ($Zn(NO_3)_2.6H_2O$), methanol(CH_3OH) and N-N-dimethylformamide (DMF) were purchased from commercial source (Sigma-Aldrich) and used without further purification.

2.2. Synthesis

2.2.1. Synthesis of aluminosilicates (Zeolite)

The method to synthesis of zeolite was modified from literature [10]. The synthesis mixture was prepared as follows: NaOH aqueous solution (1 M), TEAOH solution (5 mL) and aluminumisopropoixde (0.1 g) were mixed and stirred until all components were dissolved. At last silica source, TEOS (6 ml) was added in above solution and stirred for an additional 30 min before crystallization to get a homogenous gel. Later on this gel was transferred to a stainless steel autoclave and placed in furnace at 150 °C for 24 h at heating rate of 10 °C/min. After completion of the reaction autoclave was cooled down to room temperature and product obtained was collected by centrifugation at 4000 rpm for 15 min. The synthesized material was washed with deionized water before drying overnight at 50°C and calcined in furnace at 600 °C for 6 h. Calcined zeolite was protonated by ion-exchange with 1.0 M NH_4NO_3 solution, stirred at 80 °C for 2 h. The solid was filtered, washed with distilled water and dried at 50 °C overnight. The solid powder was then calcined at 550 °C at the rate of 5 °C/min for 4 h in order to remove NH_3 for the generation of zeolite in H^+ form.

2.2.2. Synthesis of $[Zn_3(BTC)_2]$

$[Zn_3(BTC)_2]$ was synthesized using Solvothermal method [11] The procedure was as follow: 0.368 g of zinc nitratehexahydrate ($Zn(NO_3)_2.6H_2O$) was dissolved in 20 mL of DMF:CH_3OH:H_2O (1:1:1 v/v). The quantity of 0.148 g of 1, 3, 5-benzenetricarboxylic acid was dissolved in 20 mL of the same solvent mixture and both solutions were combined with stirring. The resulting mixture was transferred to Teflon-lined stainless steel autoclave and placed in furnace at 150 °C for 24 h. At the end of the reaction, the autoclave was cooled down to room temperature, and the resulting white powder was washed with the same solvent mixture and dried overnight at 60 °C.

2.2.3. Synthesis of aluminosilicate $[Zn_3(BTC)_2]$ nanocomposite

The synthesis of zeolite-$[Zn_3(BTC)_2]$ composite was performed by the same procedure described above except that 0.1 g zeolite particles of the procedure 2.2.1 were added to the synthetic solution of $[Zn_3(BTC)_2]$ prior to Solvothermal crystallization of MOF.

2.3. Characterization

2.3.1. Powder X-ray diffraction XRD

X-ray diffraction (XRD) measurements were done with Cu Kα radiation (λ=1.5418A°, 40 kV, 40 mA). The powder samples were ground and spread on a sample holder. The samples were scanned in the range from 2θ= 5°-50° with a step size of 0.0334°.

2.3.2. Fourier Transform Infrared Spectroscopy FTIR

FTIR technique was used for the determination of functional groups in synthesized materials in transmittance (%) mode with a 16 cm^{-1} resolution and 50 scans in the mid IR region (400–4000 cm^{-1}).

2.3.3. Scanning electron microscopy/Energy dispersive X-ray sepectroscopy SEM/EDX

The morphology of the prepared materials was examined on scanning electron microscope (SEM) along with EDX.

3. Result and Discussion

Zeolite, $[Zn_3(BTC)_2]$ and zeolite-$[Zn_3(BTC)_2]$ were successfully synthesized using Solvothermal method. Synthesis of zeolite-$[Zn_3(BTC)_2]$ was carried out by hydrothermal crystallization of zeolite followed by Solvothermal growth of $[Zn_3(BTC)_2]$ from its synthetic solution in the presence of dispersed zeolite particles.

Fig. 1 shows XRD pattern of zeolite, $[Zn_3(BTC)_2]$ and zeolite-$[Zn_3(BTC)_2]$. The reflection peaks in XRD pattern of zeolite are consistent with those reported for the topologies of zeolite material. The peaks between 10° and 20° are related to cubic crystalline structure of $[Zn_3(BTC)_2]$, which is in good agreement with that reported in literature [12,13], suggesting that $[Zn_3(BTC)_2]$ was successfully synthesized by Solvothermal method.

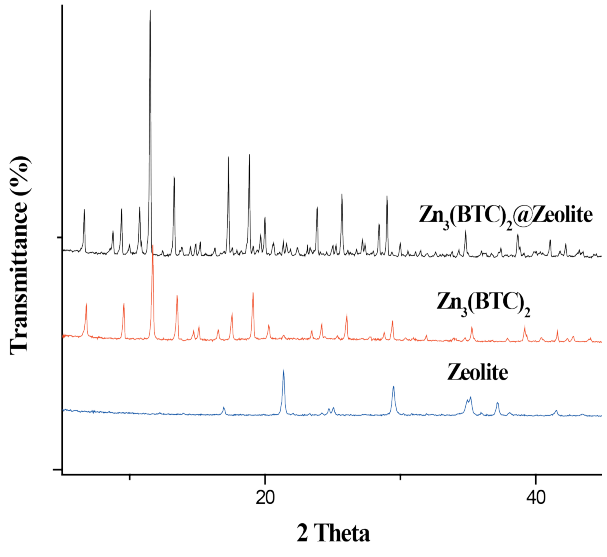

Fig. 1. XRD pattern of Zeolite, $Zn_3(BTC)_2$ and Zeolite-$Zn_3(BTC)_2$
1. ábra Zeolit, $Zn_3(BTC)_2$ és Zeolit-$Zn_3(BTC)_2$ röntgendiffraktogramjai

In XRD pattern of zeolite-$[Zn_3(BTC)_2]$ the main peak of $[Zn_3(BTC)_2]$ is at 11.5° is not changed after modification. It meant that Zn-BTC represented the major component of the

composites, and it also suggested that the composites preserved the crystalline characters of parent Zn-BTC. The similar pattern of XRD for composite material indicates the existence of well-defined MOF units in the synthesis materials. Thus, one can assume that zeolite did not prevent the formation of linkage between the zinc dimer and organic ligand [14].

FTIR spectra further confirm the results of XRD analysis on the formation of zeolite, $[Zn_3(BTC)_2]$ and composite material. It can obviously see that all vibration bands of IR spectra of zeolite and those for $[Zn_3(BTC)_2]$ were in good agreement with the published data [13]. All the characteristic peaks of zeolite could be observed in zeolite-$[Zn_3(BTC)_2]$ composite, indicating that hybrid composites were successfully synthesized, being mainly composed of zeolite and $[Zn_3(BTC)_2]$.

Fig. 2 represents the FTIR spectra of the synthesized materials. For zeolite, the characteristic broad features at 958 cm^{-1} were the asymmetric stretching vibration of T-O-T (T: Si or Al) in the framework of zeolite. For $[Zn_3(BTC)_2]$, the five typical bands were almost identical with those for the zeolite-$[Zn_3(BTC)_2]$ composites, indicating that MOF played major role in the hybrid composites. Another characteristic peaks are placed at 453 and 552 cm^{-1} for Zn (II) which prove the bonding between metal and carboxylic oxygen. The vibration bands centered on 1621/1562 cm^{-1} and 1433/1364 cm^{-1} correspond to the asymmetric stretching and the symmetric stretching vibrations of carboxylate groups respectively [12]. The presence of strong stretching vibration peak at 1621.17 cm^{-1} confirmed the deprotonation of carboxylate groups in 1, 3, 5-benzenetricarboxylic acid, upon reaction with metal ions [15].

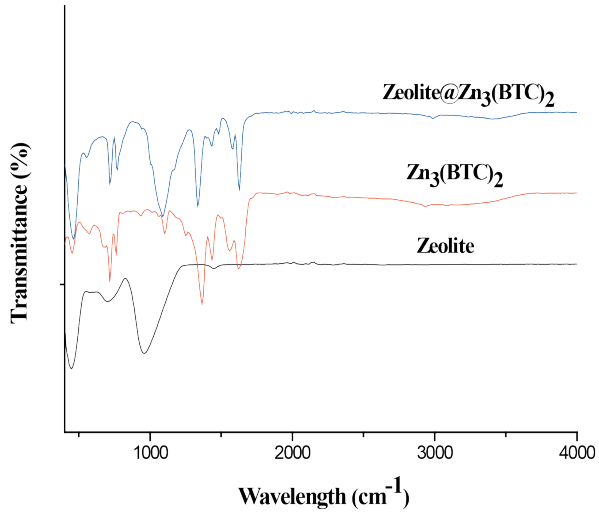

Fig. 2. FTIR spectrum of Zeolite, $Zn_3(BTC)_2$ and Zeolite-$Zn_3(BTC)_2$
2. ábra Zeolit, $Zn_3(BTC)_2$ és Zeolit-$Zn_3(BTC)_2$ FTIR spektrumai

From *Fig. 3*, the SEM photographs revealed the morphologies of the zeolite, $Zn_3(BTC)_2$ and composite material. Compared with pure $Zn_3(BTC)_2$, the composite particles (*Fig. 3.c*) still remain in its pure shape indicating an intact host matrix after loading the sample with zeolite.

EDX spectrum was shown in *Fig. 4.* Spectrum (*Fig. 4.a*) was of the zeolite particles. The zeolite construction element Si, Al and O were shown in the figure with Kα characteristic X-ray energy of 1.739 KeV, 1.486 KeV and 0.525 KeV, indicating the presence of zeolite particles. The EDX spectrum (*Fig. 4.c*) was of composite particles and was comprised of Si, Al, O and Zn peaks, indicating the presence of zeolite and MOF structures. The primary construction element of $[Zn_3(BTC)_2]$ Zn was shown with Lα characteristic X-ray energy of 1.042 KeV. The peaks at 0 come from the X-ray beam of the instrument. The EDX was done during the SEM and was performed on isolated particles, thus confirms the successful growth of zeolite onto $[Zn_3(BTC)_2]$ and the preservation of the crystallinity of both materials.

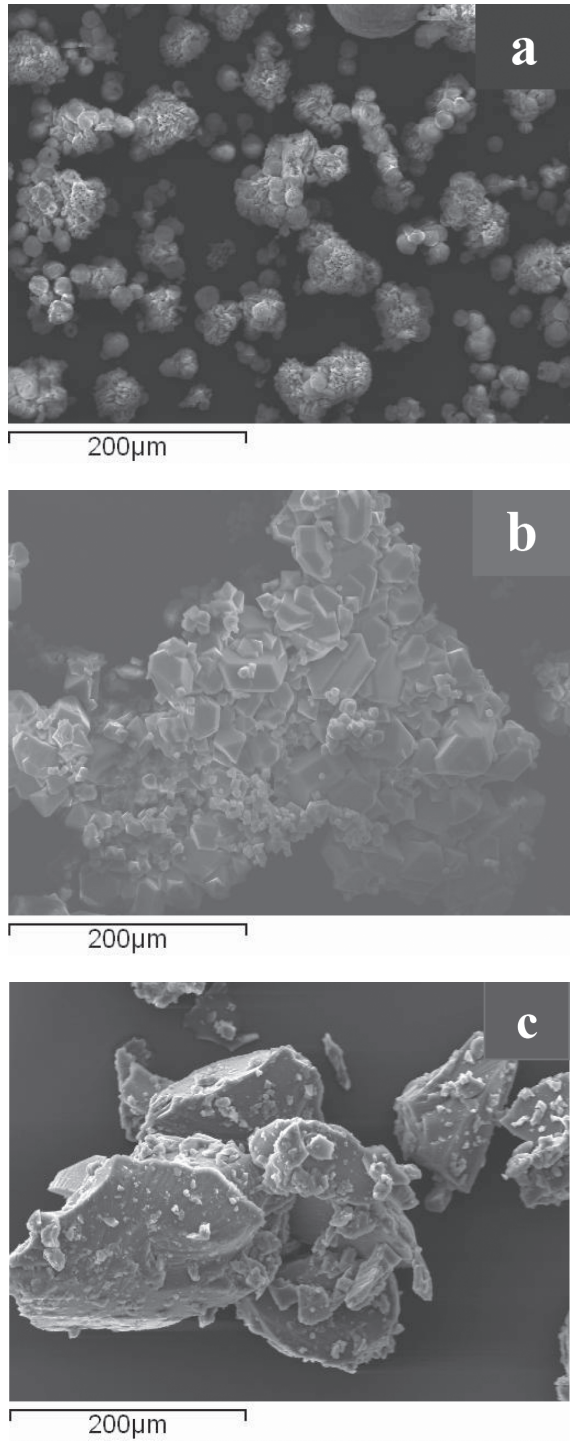

Fig. 3. SEM photograph of (a) Zeolite,(b) $Zn_3(BTC)_2$ and (c) Zeolite-$Zn_3(BTC)_2$
3. ábra Zeolit, $Zn_3(BTC)_2$ és Zeolit-$Zn_3(BTC)_2$ elektronmikroszkópos felvételei

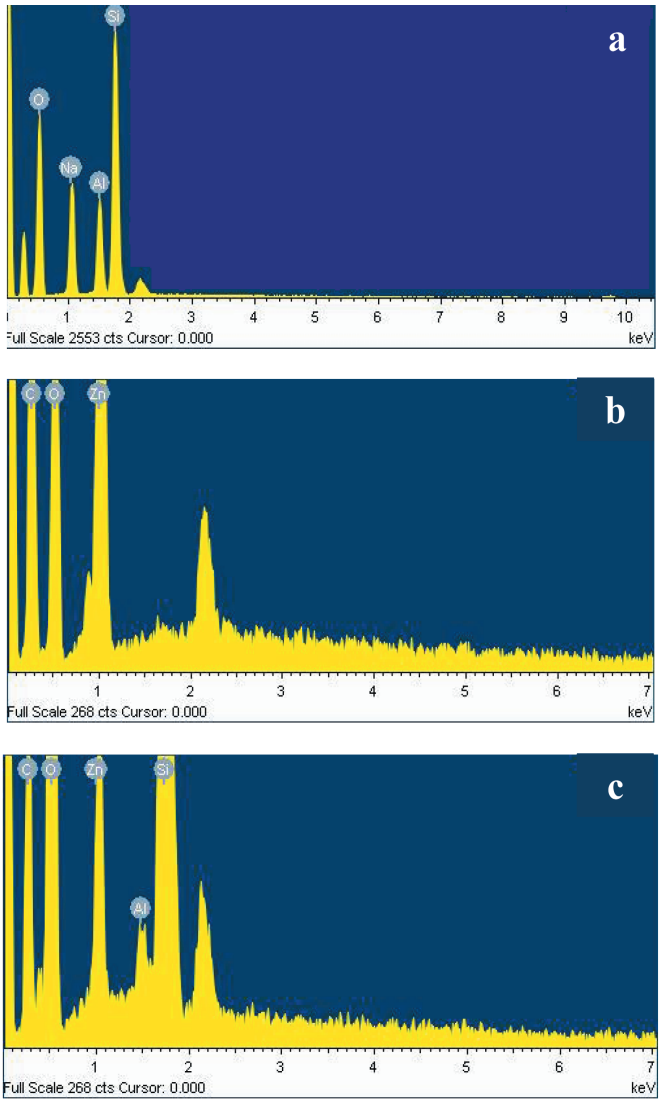

Fig. 4. EDX spectrum of (a) Zeolite, (b) $Zn_3(BTC)_2$ and (c) Zeolite-$Zn_3(BTC)_2$
4. ábra Zeolit, $Zn_3(BTC)_2$ és Zeolit-$Zn_3(BTC)_2$ EDX spektrumai

Conclusions

In summary, we report the synthesis of porous co-ordination network of $Zn_3(BTC)_2$ by solvothermal growth upon zeolite particles which were pre-synthesized via hydrothermal crystallization. The physiochemical and texture properties of synthesized materials were confirmed by XRD, FTIR and SEM/EDX. In XRD pattern of composite material (aluminosilicates with [Zn_3 (BTC)$_2$]) the main peak of [Zn_3 (BTC)$_2$] is at 11.5° which is not changed after modification. It meant that Zn-BTC represented the major component of the composites, and it also suggested that the composites preserved the crystalline characters of parent Zn-BTC. The co-existence of both vibrational peaks of zeolite and [Zn_3 (BTC)$_2$] in FTIR results further confirms the synthesis of composite material. SEM images of pure [Zn_3 (BTC)$_2$] and composite material shows that the composite particles still remain in its parent shape indicating an intact host matrix after loading the sample with zeolite. EDX results further confirm the successful synthesis of composite and strengthen the results of XRD, FTIR and SEM.

References

[1] Zhou, H. C. – Long, J. R. – Yaghi, O. M. (2012): Introduction to metal–organic frameworks, *Chemical Reviews*, Vol. 112, No. 2, pp. 673-674. https://doi.org/10.1021/cr300014x

[2] Allendorf, M. D. – Stavila, V. (2015): Crystal engineering, structure–function relationships, and the future of metal–organic frameworks. *Crystal Engineering Communication*, Vol. 17, No. 2, pp. 229-246. https://doi.org/10.1039/C4CE01693A

[3] Butova, V. V. E. – Soldatov, M. A. – Guda, A. A. – Lomachenko, K. A. – Lamberti, C. (2016): Metal-organic frameworks: structure, properties, methods of synthesis and characterization. *Russian Chemical Reviews*, Vol. 85, No. 3, pp. 280-307. https://doi.org/10.1070/RCR4554

[4] Wang, C. – Liu, D. – Lin, W. (2013): Metal–organic frameworks as a tunable platform for designing functional molecular materials. *Journal of the American Chemical Society*, Vol. 135, No. 36, pp. 13222-13234. https://doi.org/10.1021/ja308229p

[5] Q.-L. Zhu – Q. Xu (2014): Metal–organic framework composites. *Chemical Society Reviews*, Vol. 43, pp. 5468-5512. https://doi.org/10.1039/C3CS60472A

[6] Q.-L. Zhu – Q. Xu (2016): Immobilization of ultrafine metal nanoparticles to high-surface-area materials and their catalytic applications. *Chem, Vol. 1*, pp. 220-245. http://dx.doi.org/10.1016/j.chempr.2016.07.005

[7] C. Wang – K. E. de Krafft – W. Lin (2012): Pt nanoparticles@photoactive metal–organic frameworks: efficient hydrogen evolution via synergistic photoexcitation and electron injection. *Journal of the American Chemical Society*, Vol. 134, pp. 7211-7214. http://dx.doi.org/10.1021/ja300539p

[8] P. Ramaswamy – N. E. Wong – G. K. H. Shimizu (2014): MOFs as proton conductors-challenges and opportunities, *Chemical Society Reviews, Vol. 43*, pp. 5913-5932. http://dx.doi.org/10.1039/C4CS00093E

[9] Kitao, T. – Zhang, Y. – Kitagawa, S. – Wang, B. – Uemura, T. (2017): Hybridization of MOFs and polymers, *Chemical Society Reviews, Vol. 46,* pp. 3108-3133. http://dx.doi.org/10.1039/C7CS00041C

[10] Baradaran, S. – Sohrabi, M. – Bijani, P.M. – Javid, S. (2015): The 15th Iranian National Congress of Chemical Engineering, *University of Tehran,* Tehran, Iran, 17-19 February 2015.

[11] Thi, T. V. N. – Luu, C.L . – Hoang, T. C. – Nguyen, T. – Bui, T. H. – Nguyen, P. H. D. – Thi, T. P. P. (2013): Synthesis of MOF-199 and application to CO_2 adsorption, *Advances in Natural Sciences: Nanoscience and Nanotechnology*, Vol. 4, No. 3, 035016. https://doi.org/10.1088/2043-6262/4/3/035016

[12] Abbasi, A. R. – Noori, N. (2014): Synthesis, Characterization and Antibacterial Properties of Nano-Porous $Zn_3(BTC)_2{\cdot}12H_2O$ upon Silk Yarn Under Ultrasound Irradiation. *Journal of Inorganic and Organometallic Polymers and Materials*, Vol. 24, No. 6, pp. 1096-1102. https://doi.org/10.1007/s10904-014-0101-5

[13] Yang, Q. – Zhang, M. – Song, S. – Yang, B. (2017): Surface modification of PCC filled cellulose paper by MOF-5 (Zn_3(BDC)$_2$) metal–organic frameworks for use as soft gas adsorption composite materials. *Cellulose,* Vol. 24, No. 7, pp. 1-10. https://doi.org/10.1007/s10570-017-1331-9

[14] Petit, C. – Burress, J. – Bandosz, T. J. (2011): The synthesis and characterization of copper-based metal–organic framework/graphite oxide composites, *Carbon*, Vol. 49, No. 2, pp. 563-572. https://doi.org/10.1016/j.carbon.2010.09.059

[15] Papageorgiou, S. K. – Kouvelos, E. P. – Favvas, E. P. – Sapalidis, A. A. – Romanos, G. E. – Katsaros, F. K. (2010): Metal–carboxylate interactions in metal–alginate complexes studied with FTIR spectroscopy, *Carbohydrate Research*, Vol. 345, No. 4, pp. 469-473. https://doi.org/10.1016/j.carres.2009.12.010

Ref.:
Ayub, Nosheen – **Rafique,** Uzaira: *Synthesis and characterization of aluminosilicates [Zn_3 (BTC)$_2$] hybrid composite materials*
Építőanyag – Journal of Silicate Based and Composite Materials, Vol. 69, No. 3 (2017), 98–101. p.
https://doi.org/10.14382/epitoanyag-jsbcm.2017.17

creative commons Attribution

Understanding the Mechanism of Decomposition Reactions of Neat and Superplasticized ordinary Portland Cement Pastes Using Thermal Analysis

Elshafie A. M. GAD ▪ Egyptian Petroleum Research Institute ▪ eamgad@gmail.com
Amr Osman HABIB ▪ Chemistry Dept. Faculty of Engineering, Ain Shams University ▪ amrhabib2004@yahoo.com
Mahmoud M. MOUSA ▪ Faculty of Science, Benha University ▪ mousa_chem@yahoo.com

Érkezett: 2017. 10. 25. ▪ Received: nn. hh. 2017. ▪ https://doi.org/10.14382/epitoanyag-jsbcm.2017.18

Abstract

The effect of polycarboxylate superplasticizer on thermal stability and the kinetic thermal decomposition of OPC without and with 1.0 and 1.5% wt% plasticizer has been studied at temperature range of 30-1000 °C. The study was done by means of thermogravimetry (TG) technique under non-isothermal condition at a heating rate of 10 K/min. The results showed that the decomposition occurs for the superplasticized and neat OPC paste in three steps. The neat OPC was found to decompose at higher temperatures than those for the superplasticized paste. The kinetic parameters for each one of the decomposition steps were calculated through four calculation methods and the kinetic mechanisms were determined from the thermal data analysis using 35 solid state reaction models. The results showed that the mechanisms of decomposition steps depend on the percentage of the superplasticizer added to the paste. The thermodynamic parameters $\Delta S^{\#}$, $\Delta H^{\#}$ and $\Delta G^{\#}$ were also computed and discussed.

Keywords: Hydration kinetics; Ordinary Portland cement OPC; Thermogravimetrical Analyses TGA.
Kulcsszavak: Hidratációkinetika; Tiszta Portlandcement ; Termogravimetriai analízis

Prof. Dr. Elshafie A. GAD
Professor of Petrochemicals. My interests are surfactants applications, QSPR, Computational chemistry and recently Solid state Kinetics.

Dr. Amr Osman HABIB
received his M.Sc and Ph.D from Ain Shams University, Cairo, Egypt. He is currently a lecturer at Faculty of Engineering, Ain Shams University. He is a member of Technology of Building Materials and Pore Structure of Solids Unit, (R & D Unit), Faculty of Science, Ain Shams University, and member of The Engineering Consultants Centre, Faculty of Engineering, Ain Shams University.

Prof. Dr. Emer. Mahmoud M. MOUSA
Faculty of Science, Benha University, his interests are treatment of industrial solid wastes, renal function Studies, Iminodiacetic Acid Analog, Nanomaterials application and solid state kinetics.

1. Introduction

Calcium silicate hydrates (CSH) and calcium hydroxide (CH) which are the main hydration phases accounted for the properties of Portland cement paste. The dehydration of Portland cement paste causes a deterioration effect on the concrete strength. Thermal analysis tools can be used to identify each of the product compositions and their amounts due to thermal effects on cement composites. Several investigators studied thermal analysis to recognize the products due to hydration of different cement composites [1,2,3]. *Zelic* et al. [4] investigated thermal decomposition kinetics of the calcium hydroxide-Portlandite formed into hydrated ordinary Portland cement (OPC) paste with use of non-isothermal thermogravimetric data. *Sha* et al. [5] reported that the three major endothermic peaks in the DSC curves are due to loss of water from calcium silicate hydrate, dehydroxyaltion of calcium hydroxide, and decarbonation of calcium carbonate contribute respectively. *Pane* et al. [6] investigated hydration of OPC pastes containing three types of mineral additive; fly ash, ground-granulated slag, and silica fume using DTA/TGA and isothermal calorimetry It was shown that the chemically bound water obtained using DTA/TGA was proportional to heat of hydration and could be used as a measure of hydration. *Agarwal* et al. [7] studied the hydration behavior of different cements at different time intervals in the presence of superplasticizers using DTA technique. It was observed that OPC has shown retardation either blended with naphthalene-based superplasticizers or with blended polymer-based superplasticizer. However, Portland Slag Cement has been found to be compatible with all the superplasticizers. *Ye* et al. [8] reported on the properties of Self-compacting when it is exposed to elevated temperatures. Fire test has shown differences between high performance concrete and traditional concrete at elevated temperature. These differences are largely depending on the microstructural properties of concrete matrix. *Kong* et al. [9] studied the effect of elevated temperature on geopolymer paste, mortar and concrete made using fly ash as a precursor. It was found that strength loss in geopolymer concrete at elevated temperatures is attributed to the thermal mismatch between the geopolymer matrix and the aggregates. *Heikal* et al. [10] studied the effect of substitution of nano-silica on the behavior of composite cement pastes including OPC and blast-furnace slag exposed to elevated temperature up to 1000°C. DTA and TGA were carried out on cement pastes partially replaced with Neem seed husk ash [11]. The results showed that the calcium hydroxide contents increases with increase in Neem seed husk ash replacements. *Klimesch* and *Ray* [12] presented a method for consistent DTA/TGA evaluation using computer software for data analyses. DTA/TGA was used to study the effect of ground quartz addition to cement. *Alarcon-Ruiz* et al. [13] used thermal analysis techniques to study the effect of temperature in the mineralogical composition of cement hydration products. Such techniques can be used to determine fire conditions and the consequent deterioration expected in the cement paste. *Bhatty* and *Reid* [14] produces high-strength Type 1 cement. The product from raw taconite

Oxide	SiO_2	Al_2O_3	Fe_2O_3	CaO	MgO	SO_3	Na-Oxide	K- Oxide	Lime Saturation Factor	Undissolved solids	Loss on Ignition
%	19.82	4.99	3.92	62.66	0.82	2.53	0.47	0.09	0.95	0.97	3.92

Table 1 Chemical analysis of ordinary Portland cement
1. táblázat Portlandcement kémiai összetétele

and copper-nickel tailings of Minnesota is the subjected to hydration studies by using thermal methods such as TGA and DTA. Hydration is measured in terms of hydration product formation and the amount of bound water and free calcium hydroxide incorporated in them.

Reactions that occur with an increase of temperature in cement paste and concrete can be summarized as: evaporable water and a part of the bound water escapes at 30–102°C [4]. The decomposition of gypsum [15] and ettringite [16] takes place at 110–170°C, The decomposition of the C-S-H and carboaluminate hydrates undergoes at 180–300°C [17]. Dehydroxylation of the portlandite [18] occurs at 450–550°C. Decarbonation of calcium carbonate happens at 700–900°C [13].

However, the dehydration kinetics of Portland cement paste is too complex and can not be described by a single Arrhenius equation. In the present work, we studied the thermal dehydration and decomposition kinetics of OPC hardened pastes containing polycarboxylate admixtures using TGA at a heating rate of 10 K/min for two samples containing admixtures besides, control sample. Four calculation procedures based on TG curves as well as 35 mechanism functions were applied on the thermal data.

2. Materials and experimental technique

Cement: A freshly produced sample of a commercial ordinary Portland cement supplied from Suez Cement Company with the chemical composition listed in *Table 1*, was used in this study.

The specific surface area as determined by the Blaine air-permeability method was found to be 3400 cm^2/gm. The potential phase composition as estimated using Bogue's calculation [19] was found to be C_3S, 58.04; β-C_2S, 13.11; C_3A, 6.59 and C_4AF, 11.91, respectively.

3. Preparation of OPC pastes

The percentages of admixtures (1.0 & 1.5 wt %) were dissolved in water of mixing. Various cement pastes were prepared by mixing OPC with water using standard water of consistency for each paste. The control cement pastes and the superplasticized samples with 1.0 and 1.5 wt % were hydrated for 28 days.

The standard water of consistency and percentage of water reduction were listed in *Table 2.*

Paste	W/C ratio	Water reduction %
Neat OPC	0.245	0 %
OPC+1%1%	0.1712	30%
OPC+1.5 %	0.16	34.69 %

Table 2. The standard water of consistency and percentage of water reduction for the control and superplasticized cement pastes
2. táblázat Szabványos konzisztencia vízigénye és a víztartalom csökkenés mértéke folyósítószer hatására

4. Thermal analysis

The thermal decomposition of the different hardened cement pastes was studied by thermal gravimetric analysis (TGA) technique using Simultaneous TGA/DSC MODEL SDTQ 600 Thermal Analyzer (USA). Some grains were extracted from the inner core of the hardened cement pastes. These grains were crushed and ground until a grain size of 80 μm was obtained. The temperature of the furnace was programmed to rise as a constant heating rate of 10 °C/min up to 1000 °C

5. Background on non-isothermal decomposition kinetics

Kinetic process calculations result in three parameters; i. e., Ea is the activation energy, A is the pre-exponential factor, f(α) represents the mathematical form of the mechanism to be assumed for the process, and α is the conversion degree. The rate determining mechanism model may take various forms based nucleation and nucleus growth, phase boundary reaction, diffusion and chemical reaction [20].

The reaction rate equation for non-isothermal decomposition kinetics [20] can be written as follows:

$$\frac{d\alpha}{dt} = k(T)f(\alpha) \quad (1)$$

Where k is the rate constant and the conversion factor α is defined as:

$$\alpha = \frac{m_i - m_t}{m_i - m_\infty} \quad (2)$$

Where m_i is the initial mass of the sample, m_t is the mass of the sample at time t, and m_∞ is the residual mass of the sample at the end of the reaction.

Integration of Eq. (1) gives the integral rate law:

$$g(\alpha) = kt \quad (3)$$

The rate constant k is generally given by the Arrhenius equation:

$$k = A\, exp\left(\frac{-E_a}{RT}\right) \quad (4)$$

Where E_a is the activation energy, R is the gas constant, and T is the absolute temperature. The combination of Eqs. (1) and (4) gives the following relationship:

$$\frac{d\alpha}{dt} = A\, exp\left(\frac{-E_a}{RT}\right) f(\alpha) \quad (5)$$

For a dynamic TG process, introducing the heating rate, β = dT/dt, into Eq. (5), gives Eq. (6):

$$\frac{d\alpha}{dt} = \left(\frac{A}{\beta}\right) exp\left(\frac{-E_a}{RT}\right) f(\alpha) \quad (6)$$

No.	Symbol	Name of the function	g(α)	f(α)	Rate-determining mechanism
1. Chemical process or mechanism non-invoking equations					
1	$F_{1/3}$	One-third order	$1-(1-\alpha)^{2/3}$	$(3/2)(1-\alpha)^{1/3}$	Chemical reaction
2	$F_{3/4}$	Three-quarters order	$1-(1-\alpha)^{1/4}$	$4(1-\alpha)^{3/4}$	Chemical reaction
3	$F_{3/2}$	One and a half order	$(1-\alpha)^{-1/2}-1$	$2(1-\alpha)^{3/2}$	Chemical reaction
4	F_2	Second order	$(1-\alpha)^{-1}-1$	$(1-\alpha)^2$	Chemical reaction
5	F_3	Third order	$(1-\alpha)^{-2}-1$	$(1/2)(1-\alpha)^3$	Chemical reaction
2. Acceleratory rate equations					
6	$P_{3/2}$	Mampel power law	$\alpha^{3/2}$	$(2/3)\alpha^{-1/2}$	Nucleation
7	$P_{1/2}$	Mampel power law	$\alpha^{1/2}$	$2\alpha^{1/2}$	Nucleation
8	$P_{1/3}$	Mampel power law	$\alpha^{1/3}$	$3\alpha^{2/3}$	Nucleation
9	$P_{1/4}$	Mampel power law	$\alpha^{1/4}$	$4\alpha^{3/4}$	Nucleation
10	E_1	Exponential law	$\ln\alpha$	A	Nucleation
3. Sigmoidal rate equations or random nucleation and subsequent growth					
11	A_1, F_1	Avrami–Erofeev equation	$-\ln(1-\alpha)$	$(1-\alpha)$	Assumed random nucleation and its subsequent growth, n = 1
12	$A_{3/2}$	Avrami–Erofeev equation	$[-\ln(1-\alpha)]^{2/3}$	$(3/2)(1-\alpha)[-\ln(1-\alpha)]^{1/3}$	Assumed random nucleation and its subsequent growth, n = 1.5
13	A_2	Avrami–Erofeev equation	$[-\ln(1-\alpha)]^{1/2}$	$2(1-\alpha)[-\ln(1-\alpha)]^{1/2}$	Assumed random nucleation and its subsequent growth, n = 2
14	A_3	Avrami–Erofeev equation	$[-\ln(1-\alpha)]^{1/3}$	$3(1-\alpha)[-\ln(1-\alpha)]^{2/3}$	Assumed random nucleation and its subsequent growth, n = 2.5
15	A_4	Avrami–Erofeev equation	$[-\ln(1-\alpha)]^{1/4}$	$4(1-\alpha)[-\ln(1-\alpha)]^{3/4}$	Assumed random nucleation and its subsequent growth, n = 3
16	A_u	Prout–Tomkins equation	$\ln[\alpha/(1-\alpha)]$	$\alpha(1-\alpha)$	Assumed random nucleation and its subsequent growth, n = 4 Branching nuclei
4. Deceleratory rate equations 4.1. Phase boundary reaction					
17	R_1,F_0,P_1	Power law	α	$(1-\alpha)^0$	Contracting disk
18	R_2, $F_{1/2}$	Power law	$1-(1-\alpha)^{1/2}$	$2(1-\alpha)^{1/2}$	Contracting cylinder (cylindrical symmetry)
19	R_3, $F_{2/3}$	Power law	$1-(1-\alpha)^{1/3}$	$3(1-\alpha)^{2/3}$	Contracting sphere (spherical symmetry)
4.2. Based on the diffusion mechanism					
20	D_1	Parabola low	α^2	$\frac{1}{2}\alpha$	One-dimensional diffusion
21	D_2	Valensi equation	$\alpha+(1-\alpha)\ln((1-\alpha)$	$[-\ln(1-\alpha)]^{-1}$	Two-dimension diffusion
22	D_3	Jander equation	$[1-(1-\alpha)^{1/3}]^2$	$(3/2)(1-\alpha)^{2/3}[1-(1-\alpha)^{1/3}]^{-1}$	Three-dimensional diffusion, spherical symmetry
23	D_4	Ginstling–Brounstein equation	$1-2\alpha/3-(1-\alpha)^{2/3}$	$(3/2)[(1-\alpha)^{-1/3}-1]^{-1}$	Three-dimensional diffusion, cylindrical symmetry
24	D_5	Zhuravlev, Lesokin, Tempelman equation	$[(1-\alpha)^{-1/3}-1]^2$	$(3/2)(1-\alpha)^{4/3}[(1-\alpha)^{-1/3}-1]^{-1}$	Three-dimensional diffusion
25	D_6	anti-Jander equation	$[(1+\alpha)^{1/3}-1]^2$	$(3/2)(1+\alpha)^{2/3}[(1+\alpha)^{1/3}-1]^{-1}$	Three-dimensional diffusion
26	D_7	anti-Ginstling-Brounstein equation	$1+2\alpha/3-(1+\alpha)^{2/3}$	$(3/2)[(1+\alpha)^{-1/3}-1]^{-1}$	Three-dimensional diffusion
27	D_8	anti-Zhuravlev, Lesokin, Tempelman equation	$[(1+\alpha)^{-1/3}-1]^2$	$(3/2)(1+\alpha)^{4/3}[(1+\alpha)^{-1/3}-1]^{-1}$	Three-dimensional diffusion
5. Another kinetics equations with unjustified mechanism					
28	G_1		$1-(1-\alpha)^2$	$\frac{1}{2}(1-\alpha)$	
29	G_2		$1-(1-\alpha)^3$	$1/3(1-\alpha)^2$	
30	G_3		$1-(1-\alpha)^4$	$\frac{1}{4}(1-\alpha)^3$	
31	G_4		$[-\ln(1-\alpha)]^2$	$(1/2)(1-\alpha)[-\ln(1-\alpha)]^{-1}$	
32	G_5		$[-\ln(1-\alpha)]^3$	$(1/3)(1-\alpha)[-\ln(1-\alpha)]^{-2}$	
33	G_6		$[-\ln(1-\alpha)]^4$	$(1/4)(1-\alpha)[-\ln(1-\alpha)]^{-3}$	
34	G_7		$[1-(1-\alpha)^{1/2}]^{1/2}$	$4\{(1-\alpha)[1-(1-\alpha)]^{1/2}\}^{1/2}$	
35	G_8		$[1-(1-\alpha)^{1/3}]^{1/2}$	$6(1-\alpha)^{2/3}[1-(1-\alpha)^{1/3}]^{1/2}$	

Table 3. Algebraic expressions of functions g(α) and f(α) and its corresponding mechanism. [20]
3. táblázat Algebrai kifejezések a g(α) és f(α) függvényekre és a hozzájuk tartozó mechanizmusok. [20]

6. Results and discussion

Thermograms (TGA and DTG) curves of OPC containing polycarboxylate admixtures (dose = 1.0 or 1.5%) and the control sample are shown in *Figs. 1* and *2*. The curves show three weight loss zones. The first drop in weight ranging from 100 to 200 °C, is accounted for the dehydration of Ca-silicate hydrates. The second weight loss is displayed at 450 to 500 °C which is attributed to dehydroxyaltion of portlandite. The third loss of weight shown at 700 to 750 °C, is due to decarbonation of calcium carbonate. The thermal analyses data are summarized in *Table 3*. It shows that the modified OPC Samples decompose at higher temperatures than that found for untreated OPC. This refers to that the addition of polycarboxylate admixture increases the thermal stability of OPC.

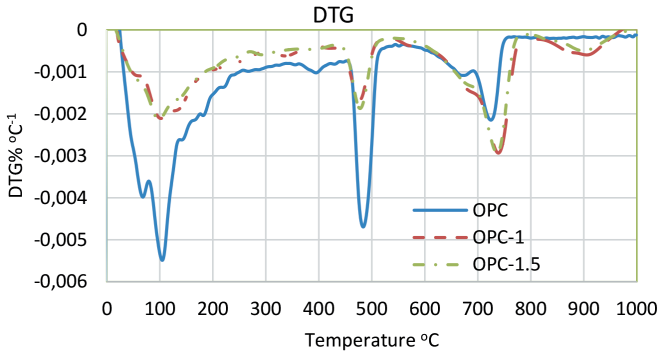

Fig. 1. DTG curves of the thermal decomposition of OPC containing polycarboxylate, heating rate = 10 Kmin-1
1. ábra DTG görbék polikarboxilát tartalmú cementpépekre, felfűtési sebesség = 10 Kmin-1

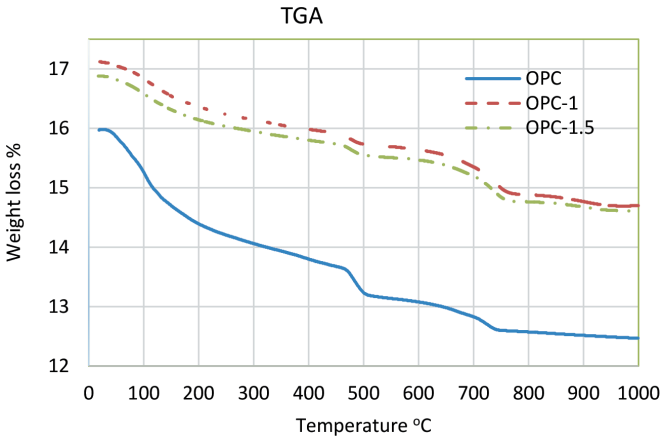

Fig. 2. TGA curves of the thermal decomposition of OPC containing polycarboxylate, heating rate = 10 Kmin-1
2. ábra TGA görbék polikarboxilát tartalmú cementpépekre, felfűtési sebesség = 10 Kmin-1

The kinetic parameters for the three stages of the thermal decomposition of the investigated samples were calculated using fraction conversion 0.1< α <0.8 obtained from a single thermos-analytical curve (heating rate 10 K/min). In this study, four calculation methods: *Coats* and *Redfern* [21] Eq. (7) and *Madhysudanan-Krishnan-Ninan* [22], Eq. (8), *Wanjun* et al. [22] Eq. (9) and *Tang* et al.[23] Eq. (10)as as well as 35 mechanism models g(α) were used to get the kinetic data:

$$\ln\left(\frac{g(\alpha)}{T^2}\right) = ln\left[\frac{AR}{\beta E_a}\left(1-\frac{2RT}{E_a}\right)\right] - \frac{E_a}{RT} \cong ln\left(\frac{AR}{\beta E_a}\right) - \frac{E_a}{RT} \quad (7)$$

$$\ln\left(\frac{g(\alpha)}{T^2}\right) = ln\left[\frac{AR}{\beta(1.00198882E+1.87391198RT_p)}\right] - \frac{E_a}{RT} \quad (8)$$

$$\ln\left[\frac{g(\alpha)}{T^{1.894661}}\right] = \left[\ln\frac{AE_a}{\beta R} + 3.635041 - 1.89466\, lnE_a\right] - \frac{1.00145033E_a}{RT} \quad (9)$$

$$\ln\left[\frac{g(\alpha)}{T^{1.921503}}\right] = \left[\frac{\ln AE_a}{\beta R} + 3.772050 - 1.921503 \ln E_a\right] - \frac{0.120394E_a}{T} \quad (10)$$

Plotting the left-hand sides of Eqs. (7-10), which involves $g(\alpha)$ versus $1/T$, gives E_a and A from the slope and intercept, respectively. The model that gives the higher correlation coefficient of the linear regression R^2 for Eqs. (7) – (10) fit is chosen as the selected kinetic model. A mathematical program based on Excel 2016 was designed by the authors to calculate values of activation energy Ea and the pre-exponential as shown in *Table 4*.

The best mechanisms for each decomposition step, the kinetic results of the applied equations show kinetic models and parameters close to each other in the most cases as shown in *Table 4*. From which the best kinetic models according to the highest correlation coefficients and the kinetic parameters are given in *Table 5*. It can be seen that the mechanism of step depends on the percentage of the superplasticizer.

The pre-exponential factor A is calculated from the intercept of the plots of Eqs. (7-10), and from the theory of the activated complex (transition state) of *Eyring* [24,25], the following general equation may be written:

$$A = \frac{ek_BT_p}{h} exp\left(\frac{\Delta S^{\neq}}{R}\right) \quad (17)$$

Where: e = 2.7183 is the Neper number; k_B – Boltzmann constant; h – Plank constant, and T_p is the peak temperature of DTG curve.

According to the values of activation energy E and pre-exponential factor A for the different stages of decomposition, The calculated values of $\Delta S^{\neq}$, $\Delta H^{\neq}$ and $\Delta G^{\neq}$ are calculated using Eqs. (18 – 20) at $T = T_p$ (T_p is the DTG peak temperature at the corresponding stage), because this temperature characterizes the highest rate of the decomposition process. Therefore, the change of the activated entropy can be calculated according to the formula:

$$\Delta S^{\neq} = R\ln\frac{Ah}{ek_BT_p} \quad (18)$$

Since

$$\Delta H^{\neq} = E - RT_p \quad (19)$$

The changes in the activated enthalpy $\Delta H^{\neq}$ and the Gibbs free energy $\Delta G^{\neq}$ for the activated complex formation from the reactant are calculated using the well-known thermodynamical equation:

$$\Delta G^{\neq} = \Delta H^{\neq} - T_p\Delta S^{\neq} \quad (20)$$

	Decomposition step		Kinetic models			
			Eq 7	Eq 8	Eq 9	Eq 10
OPC	1St step	Mechanism	F3/2	F3/2	F3/2	F2
		Max R^2	0.9969	0.9969	0.9969	0.9941
		Ea	99.764	99.764	99.910	115.2940
		A	3.171E+13	2.764E+14	3.51913E+13	1.42983E+16
	2nd step	Mechanism	G6	P1/4	G6	G6
		Max R^2	0.9968	0.9993	0.9968	0.9973
		Ea	1313.022	50.837	1317.998	1339.6461
		A	2.838E+90	2.599E+03	3.05568E+93	7.87165E+94
	3rd step	Mechanism	Au	D7	G6	G6
		Max R^2	0.9948	0.9955	0.9912	0.9933
		Ea	614.035	275.823	802.540	805.8707
		A	1.107E+32	4.103E+13	2.02021E+45	2.40603E+45
OPC+1.0 %	1St step	Mechanism	F3/2	D5	D5	D5
		Max R^2	0.9988	0.9993	0.9993	0.9994
		Ea	46.839	95.010	95.158	93.8318
		A	5.750E+05	8.550E+12	1.08953E+12	6.51732E+11
	2nd step	Mechanism	G8	D7	D1	D1
		Max R^2	0.9906	0.9956	0.9799	0.9688
		Ea	-7.889	85.079	91.518	93.8317
		A	-4.440E-03	4.412E+04	189154.1585	281841.940
	3rd step	Mechanism	Au	P1/4	D5	G6
		Max R^2	0.9941	0.9977	0.9937	0.9920
		Ea	825.910	47.965	719.201	1337.9727
		A	8.463E+42	1.531E+02	6.73532E+36	9.34991E+72
OPC+1.5%	1St step	Mechanism	G8	F2	F2	F2
		Max R^2	0.9969	0.9965	0.9965	0.9970
		Ea	-3.388	60.676	60.863	61.7420
		A	-8.774E-	9.514E+08	122772431.9	163422155.
	2nd step	Mechanism	G8	D7	G6	G6
		Max R^2	0.9845	0.9945	0.9620	0.9598
		Ea	-8.314	86.000	268.665	270.7971
		A	-4.269E-	3.074E+04	2.96196E+20	3.21247E+20
	3rd step	Mechanism	G6	P1/4	D5	D5
		Max R^2	0.9976	0.9988	0.9982	0.9984
		Ea	1653.171	62.673	898.848	886.3492
		A	9.769E+85	1.044E+03	6.97492E+45	1.42405E+45

Table 4. Kinetic parameters, activation energy (Ea) and the pre-exponential (A) calculated from Coats et al. Eq. (7), Wanjun et al. Eq. (8), Madhysudanan et al Eq. (9) and Tang et al. Eq. (10), according to maximum correlation coefficients out of 35 models of mechanism of decomposition of different cement pastes

4. táblázat Kinetikai paraméterek, aktiválási energia (Ea) és hatványkitevő (A) számított értékei Coats et al. Eq. (7), Wanjun et al. Eq. (8), Madhysudanan et al Eq. (9) és Tang et al. Eq. (10) alapján

Decomposition step	OPC	OPC+1.0%	OPC+1.5%
Dehydration	$F_{3/2}$ – Chemical reaction	D5 – Three-dimensional diffusion	F2 – Second order reaction
Dihydroxylation	G6 – Unjustified mechanism	D1 – One dimensional diffusion	G6 – Unjustified mechanism
Decarbonation	G6 – Unjustified mechanism	P ¼ – Nucleation	P ¼ – Nucleation

Table 5. Summary of the rate determining mechanism of the thermal decomposition steps of the neat cement pastes and the superplasticized cement pastes with 1.0 and 1.5%

5. táblázat A hőbomlási lépcsők mechanizmusainak összefoglalása tiszta cementpépekre, ill. 1,0 és 1,5% folyósítószer tartalmú cementpépekre

Decomposition step		OPC	OPC+1.0%	OPC+1.5%	Units
Dehydration	$\Delta S^{\#}$	4.24	-28.92	-97.85	J/mol.K
	$\Delta H^{\#}$	96.80	90.72	58.63	kJ/mol
	$\Delta G^{\#}$	95.22	101.51	95.13	Kj/mol
Dihydroxylation	$\Delta S^{\#}$	-195.22	-171.67	-174.68	J/(mol.K)
	$\Delta H^{\#}$	44.81	79.049	79.97	kJ/mol
	$\Delta G^{\#}$	185.95	203.17	206.26	Kj/mol
Decarbonation	$\Delta S^{\#}$	-2.45	-221.23	-205.27	J/(mol.K)
	$\Delta H^{\#}$	267.71	39.85	54.56	kJ/mol
	$\Delta G^{\#}$	270.10	255.11	254.28	Kj/mol

Table 6. Thermodynamic parameters for different stages of thermal decomposition of hardened neat cement past and plasticized cement paste

6. táblázat Termodinamikai paraméterek a hőbomlás különböző fázisaiban tiszta cementpépekre és folyósítószer tartalmú cementpépekre

The thermodynamic results obtained are given in *Table 6*. From which it can be seen that the $\Delta S^{\#}$ value for the first decomposition stage of the hardened cement past is positive. It means that the activated complexes are less order in the arrangement, higher entropy. However, first decomposition stages of plasticized samples with 1.0 and 1.5% show negative values of $\Delta S^{\#}$ it means that the corresponding activated complex more arrangement lower entropy. While for the 2nd and 3rd decomposition stage, the corresponding activated complexes have negative values of $\Delta S^{\#}$ referring to higher degree of arrangement, i.e lower entropy than the initial state.

7. Conclusions

The addition of polycarboxylate superplasticizer into OPC with 1 and 1.5 wt% increased its thermal stability without any change in the thermal decomposition products. Whereas, the kinetic study showed that the mechanism for each decomposition step depends on the percentage of plasticizer found in the OPC sample.

Compliance with Ethical Standards

The authors declare that they have no conflict of interest.

References

[1] Sha W. – Pereira G.: Differential scanning calorimetry study of ordinary Portland cement paste containing metakaolin and theoretical approach of metakaolin activity. *Cem Concr Compos*. 2001;23(6):455-461. https://doi.org/10.1016/S0958-9465(00)00090-1

[2] Gruyaert E. – Robeyst N. – De Belie N.: Study of the hydration of Portland cement blended with blast-furnace slag by calorimetry and thermogravimetry. *J Therm Anal Calorim*. 2010;102(3):941-951. https://doi.org/10.1007/s10973-010-0841-6

[3] Mendes A. – Sanjayan J. – Collins F.: Phase transformations and mechanical strength of OPC/Slag pastes submitted to high temperatures. *Mater Struct.* 2008;41(2):345-350. https://doi.org/10.1617/s11527-007-9247-8

[4] Zelic J. – Ugrina L. – Jozic D.: Application of Thermal Methods in the Chemistry of Cement: Kinetic of Portlandite from Non-Isothermal Thermogravimetric Data. *First Int Profic Test Conf*. 2007:420-429.

[5] Sha W. – O'Neill E. A. – Guo Z.: Differential scanning calorimetry study of ordinary Portland cement. *Cem Concr Res*. 1999;29(9):1487-1489. https://doi.org/10.1016/S0008-8846(99)00128-3

[6] Pane I. – Hansen W.: Investigation of blended cement hydration by isothermal calorimetry and thermal analysis. *Cem Concr Res.* 2005;35(6):1155-1164. https://doi.org/10.1016/j.cemconres.2004.10.027

[7] Agarwal S. K. – Masood I. – Malhotra SK.: Compatibility of superplasticizers with different cements. *Constr Build Mater*. 2000;14(5):253-259. https://doi.org/10.1016/S0950-0618(00)00025-8

[8] Ye G. – Liu X. – De Schutter G. – Taerwe L. – Vandevelde P.: Phase distribution and microstructural changes of self-compacting cement paste at elevated temperature. *Cem Concr Res*. 2007;37(6):978-987. https://doi.org/10.1016/j.cemconres.2007.02.011

[9] Kong D. L. Y. – Sanjayan J. G.: Effect of elevated temperatures on geopolymer paste, mortar and concrete. *Cem Concr Res*. 2010;40(2):334-339. https://doi.org/10.1016/j.cemconres.2009.10.017

[10] Heikal M. – Ali AI – Ismail M. N. – Ibrahim SANS.: Behavior of composite cement pastes containing silica nano-particles at elevated temperature. *Constr Build Mater*. 2014;70:339-350. https://doi.org/10.1016/j.conbuildmat.2014.07.078

[11] Musa N. M.: Thermal Analysis of Cement Paste Partially Replaced With Neem Seed Husk Ash. *Int J Sci Eng Res*. 2014;5(1):1101-1105. http://www.ijser.org.

[12] Klimesch D. S. – Ray A.: The use of DTA/TGA to study the effects of ground quartz with different surface areas in autoclaved cement: quartz pastes. Part 1: A method for evaluating DTA/TGA results. *Thermochim Acta*. 1996;289(1):41-54. https://doi.org/10.1016/S0040-6031(96)03033-X

[13] Alarcon-Ruiz L. – Platret G. – Massieu E. – Ehrlacher A.: The use of thermal analysis in assessing the effect of temperature on a cement paste. *Cem Concr Res*. 2005;35(3):609-613. https://doi.org/10.1016/j.cemconres.2004.06.015

[14] Bhatty J. I. – Reid K. J.: Use of thermal analysis in the hydration studies of a type 1 portland cement produced from mineral tailings. *Thermochim Acta*. 1985;91:95-105. https://doi.org/10.1016/0040-6031(85)85205-9

[15] F. Paulik – J. Paulik M. A.: Thermal decomposition of gypsum. *Thermochim Acta*. 1992;200:195-204. https://doi.org/10.1016/0040-6031(92)85115-C

[16] Sha W. – Pereira G. B.: Differential scanning calorimetry study of ordinary Portland cement paste containing metakaolin and theoretical approach of metakaolin activity. *Cem Concr Compos*. 2001;23(6):455-461. https://doi.org/10.1016/S0958-9465(00)00090-1

[17] Gard J. A. – Taylor H. F. W.: Calcium silicate hydrate (II) ("C-S-H(II)"). *Cem Concr Res*. 1976;6(5):667-677. https://doi.org/10.1016/0008-8846(76)90031-4

[18] Alarcon-Ruiz L. – Platret G. – Massieu E. – Ehrlacher A.: The use of thermal analysis in assessing the effect of temperature on a cement paste. *Cem Concr Res*. 2005;35(3):609-613. https://doi.org/10.1016/j.cemconres.2004.06.015

[19] Skibsted J. – Jakobsen H. J. – Hall C.: Quantification of calcium silicate phases in Portland cements by 29 Si MAS NMR spectroscopy. *J Chem Soc* 1995;91(24):4423-4430.

[20] Vlaev L. – Nedelchev N. – Gyurova K. – Zagorcheva M.: A comparative study of non-isothermal kinetics of decomposition of calcium oxalate monohydrate. *J Anal Appl Pyrolysis*. 2008;81(2):253-262. https://doi.org/10.1016/j.jaap.2007.12.003

[21] Abbasi M. H. – Kahrizsangi R. E.: Evaluation of reliability of Coats-Redfernnext term method for kinetic analysis of non-isothermal TGA. *TransNonfferous Met Soc China*. 2008:217-221. https://doi.org/10.1016/S1003-6326(08)60039-4

[22] Georgieva V. – Vlaev L. – Gyurova K.: Non-isothermal degradation kinetics of CaCO3 from different origin. *J Chem*. 2013;2013. https://doi.org/10.1155/2013/872981

[23] Torkkeli A.: Droplet microfluidics on a planar surface. *VTT Publ.* 2003;55(504):3-194. https://doi.org/10.1002/aic

[24] Giese B. C. H. – Bamford, C. F. H.: Tipper (Eds.): Comprehensive Chemical Kinetics, Vol. 16, *Liquid-Phase Oxidation*, Elsevier, Amsterdam 1980. 264 Seiten, Preis: US $ 87.75. Berichte der Bunsengesellschaft für Phys Chemie. 1981;85(9):721-722. https://doi.org/10.1002/bbpc.19810850935

[25] Dsc C. F. – Dielectric B.: Journal of Thermal Analysis and Calorimetry. Vol 91. *Kluwer Academic Publishers*; 2008. https://doi.org/10.1007/s10973-008-3100-3

Ref.:

Gad, Elshafie A. M. – **Habib,** Amr Osman – **Mousa,** Mahmoud M.: *Understanding the Mechanism of Decomposition Reactions of Neat and Superplasticized ordinary Portland Cement Pastes Using Thermal Analysis*

Építőanyag – Journal of Silicate Based and Composite Materials, Vol. 69, No. 3 (2017), 102–107. p.

https://doi.org/10.14382/epitoanyag-jsbcm.2017.18